RUPRECHT-KARLS-UNIVERSITÄT HEIDELBERG

Ilja Bytschok

From Shared Input to correlated Neuron Dynamics: Development of a Predictive Framework

Diplomarbeit

KIRCHHOFF-INSTITUT FÜR PHYSIK

Faculty of Physics and Astronomy

University of Heidelberg

Diploma thesis

in Physics

submitted by

Ilja Bytschok

born in Tomsk, Russia

From Shared Input to correlated Neuron Dynamics: Development of a Predictive Framework

This diploma thesis has been carried out by Ilja Bytschok at the
Kirchhoff Institute for Physics
Ruprecht-Karls-Universität Heidelberg
under the supervision of
Prof. Dr. Karlheinz Meier

From Shared Input to correlated Neuron Dynamics: Development of a Predictive Framework

Depending on the nature and number of shared afferent inputs, neurons display varying degrees of correlated behavior. Especially in, but not only limited to, the context of neuromorphic hardware, where finite bandwidth may cause inevitable input overlap, it is important to be able to quantify and predict the resulting amount of neural response correlation. In this thesis, a mathematical framework is derived which allows an analytic prediction of membrane potential distributions of LIF neurons, both current- and conductance-based, the latter being treated in the high conductance state approximation. These results are subsequently used to predict both subthreshold and spike-based correlations, as quantified by two different measures: Pearson's product-moment correlation coefficient and the Symmetric Uncertainty.

Entwicklung eines Formalismus zur Vorhersage korrelierter neuronaler Dynamik aufgrund gemeinsamer Inputs

Abhängig von den Eigenschaften und der Anzahl ihrer gemeinsamen Inputs weisen Neurone ein variierendes Maß an korreliertem Verhalten auf. Insbesondere, aber nicht nur, im Kontext neuromorpher Hardware, bei der begrenzte Bandbreite unweigerlich zu Überlagerungen des Inputs führen kann, ist es wichtig, die daraus resultierende korrelierte Dynamik quantifizieren und vorhersagen zu können. In dieser Arbeit wird ein mathematischer Formalismus entwickelt, welcher es erlaubt, die Membranpotentialverteilung von LIF-Neuronen vorherzusagen, sowohl für den strom- als auch für den konduktanzbasierten Fall. Bei Letzterem wird als Näherung ein Zustand hoher Membrankonduktanz angenommen. Die hieraus gewonnenen Resultate werden benutzt, um Korrelationen des unterschwelligen Membranpotentialverlaufs und des Spike-Verhaltens vorherzusagen. Diese werden definiert über zwei Maße: der Pearson-Korrelationskoeffizient und die Symmetrische Unbestimmtheit.

Contents

1 Introduction

With the formulation of the "neuron theory" around the beginning of the 20th century, Ramon y Cajal set the foundations of an entirely new research discipline, one that would finally be able to address the age-old questions about perception and consciousness on a scientific basis. Over a comparatively short period of time, neuroscience has evolved at a breathtaking pace, not least due to the many technological breakthroughs achieved during the last hundred years.

Maybe the most important experimental breakthrough came with the development of intra-and extracellular recording techniques, which allowed A. L. Hodgkin and A. F. Huxley the formulation of their eponymous neuron model in 1952. Over time, ever more complex and detailed measurements have been allowed by new techniques such as patch clamping, multi-electrode arrays, EEG, MEG, FMRI etc. These experimental methods allowed the development of microscopic (on the level of single neurons and synapses) as well as macroscopic (on the network level) neuroscientific models.

In parallel with the accumulation of experimental findings, theoretical methods have also been under constant development. In the attempt of formalizing the dynamics of neural networks, a wealth of models has been developed. Neuron models cover a vast range of abstraction and complexity, from the Integrate and Fire model proposed as early as 1907 by Lapicque to the Adaptive Exponential Integrate and Fire model by Brette and Gerstner in 2005, culminating in extremely detailed models down to the level of individual ion channels, as investigated e.g. in the Blue Brain Project. For studying entire networks of neurons, various mathematical tools have been developed or borrowed from related disciplines, such as stochastic differential calculus, mean-field theory and information theory, only to name a few (*Dayan and Abbott* [2001], *Gerstner and Kistler* [2002], *Rieke et al.* [1997]).

Because, however, many functional aspects of neural networks seem to reside in their complexity, purely mathematical approaches have a hard time capturing the multiple spatial and temporal scales involved in their dynamics. With the dawn of the computer age around the 1950s, an extremely useful tool became available to the neuroscientific community, giving birth to a new branch of research - computational neuroscience. The unparalleled technological progress achieved during the following decades, famously epitomized by Moore's law, allowed an equivalently rapid increase in the complexity and size of simulated networks. Today, standard desktop machines are routinely utilized to simulate networks of tens of thousands of point neurons, while dedicated multiprocessor architectures (such as IBMs Blue Gene) are able to efficiently simulate networks of tens

of millions of multicompartment Hodgkin-Huxley neurons (*Djurfeld et al.* [2008]).

Nevertheless, standard general-purpose processor architectures present an obvious drawback when used for neural network simulations: their (by design) inherently serial information processing is extremely inefficient in reproducing the massively parallel processing which occurs in the brain. With raw computational power per unit of surface soon reaching a threshold imposed by miniaturization limitations, the only remaining option resides in the design of parallel processing architectures, as for example realized by the IBM Blue Gene series mentioned above. However, this approach also suffers from strong scalability limitations, including communication bandwidth, power consumption and speed. Not least do these machines also pose the problem of availability to the larger scientific community, as only few of them are likely to be available at any one time in the future.

1.1 Neuromorphic Hardware, FACETS and BrainScaleS

An alternative approach was first proposed by Mead in the 1980s. The idea behind so-called neuromorphic hardware is the direct implementation of neuron and synapse models within circuits on a silicon substrate using available *VLSI*[1] technology. In this context, the term "emulation" has been coined, because instead of numerically integrating the appropriate differential equations in a general-purpose processor (i.e. simulating the network), neuromorphic circuits intrinsically obey the same dynamics as their biological archetypes. This circumvents the glaring inefficacy of simulating a parallel system on a serial processor, thus greatly reducing unnecessary expenditure of hardware components - with a corresponding reduction in power consumption - while also coming with an added (and somewhat inevitable) speedup benefit: because typical circuit elements in VLSI are much smaller than their biological counterparts, the intrinsic time constants also become proportionately small.

While many research teams focus on specialized architectures (*Brüderle et al.* [2011]), only few approaches are concerned with building general-purpose emulation platforms. The *FACETS*[2] project, as well as its successor BrainScaleS, has been a leading proponent of such a general-purpose neuromorphic device. These projects have united a highly interdisciplinary group of teams under a common banner, providing expertise in experimental neurobiology, physics, mathematics, computer science and electronics, in a joint effort to understand and reproduce emergent phenomena of biological neural networks, with a particular focus on the mammalian neocortex. One of the main pillars of these projects is the design and construction of a highly accelerated neuromorphic device which is to serve as an emulation platform for neural network models developed by the consortium.

[1] Very Large Scale Inegration
[2] Fast Analog Computing with Emergent Transient States

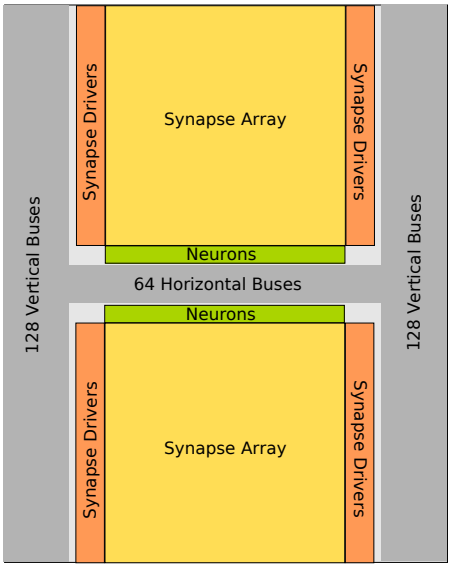

Figure 1.1: Illustration of a HICANN-chip. (Image is used with permission from B. Vogginger, *Vogginger* [2010])

In the first years of FACETS, a single-chip device has been constructed and tested - the *Spikey chip* (*Schemmel et al.* [2007]). It implements 384 conductance-based Leaky Integrate and Fire neurons and a synaptic array with a total of 98304 synapses, allowing almost arbitrary interconnections between the neurons on the chip. The synapses themselves feature both short-term[3] and long-term[4] *STDP* - Spike-Timing Dependent Plasticity plasticity. This device operates at an acceleration factor of 10000 with respect to biological real-time.

The Spikey chip, however, was only a prototype for a much larger device. In a first step, a new neuromorphic core was designed - the *HICANN* chip[5] (fig. 1.1). Taken on its own, this chip has two blocks with 256 AdEx[6] neurons and 65536 synapses[7] each. The more crucial second step, however, involves the technique of wafer-scale integration: instead of cutting the silicon substrate into individual chips, the full wafer, containing 352 HICANN modules, is subjected to a post-processing procedure which allows the interconnection of the individual modules with a high connection density (*Schemmel et al.* [2010]). The final wafer, which can operate at a speedup ranging from 10^3 to 10^5 compared to biological real time, contains about $2 \cdot 10^5$ neurons and $4 \cdot 10^7$ configurable synapses 1.2.

[3] as described in *Markram et al.* [1998]
[4] *Song and Abbott* [2001]
[5] High Input Count Analog Neural Network
[6] Adaptive Exponential Integrate and Fire Model, *Brette and Gerstner* [2005]
[7] with the same plasticity mechanisms as in the Spikey chip

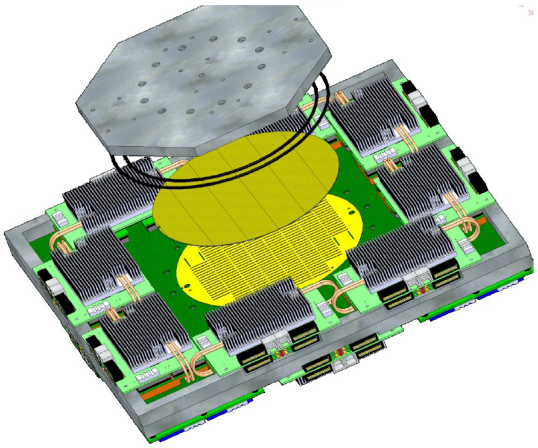

Figure 1.2: Illustration of a HICANN-wafer. (Image is taken from *Schemmel et al.* [2010])

1.2 The Bandwidth Bottleneck: Causes and Consequences

The finite size of the individual chips is a critical limiting factor to the total number of available synapses, as they require the most space. On the Spikey chip, for instance, when each neuron has at least one projection on another neuron, only a maximum of 128 external input channels remain (*Bruederle* [2009]). Along with input bandwidth limitations due to the high acceleration rate, this can easily lead to situations where it is impossible to provide each neuron with independent input sources.

Concerning the input bandwidth, a particular improvement over the Spikey chip is the inclusion of 8 Poisson spike generators on each HICANN. However, these are obviously not enough to stimulate each of the 512 neurons in the chip independently. Even when considering external inputs, for emulated networks beyond a certain size, the available maximum bandwidth does not allow independent stimulation of every neuron in a biologically realistic regime.

These limitations are in no way particular to the FACETS/BrainScaleS hardware, since the physical limitations of any hardware device impose hard restrictions to the maximum possible input bandwidth. Unfortunately, in many network models, independent stimulation of neurons is assumed (e.g. *Lundqvist et al.* [2006], *Kremkow et al.* [2010]). Lack of independence can cause correlated behavior, possibly leading to strongly distorted network dynamics which can easily break down the functionality of the network. It therefore appears inevitable that the effects of such correlations need to be investigated and minimized before attempting neuromorphic emulation.

It is quite evident that for any two neurons, decreasing the number of shared inputs also

decreases the amount of (undesired) correlation in their behavior. The aforementioned minimization step can therefore be formulated as the following optimization problem: given a number of input channels and a number of neurons, which configurations minimize the number of shared channels and maximize the number of independent channels at the same time? (See fig 1.3) This particular question has been addressed elswhere[8] and will not be of further concern here.

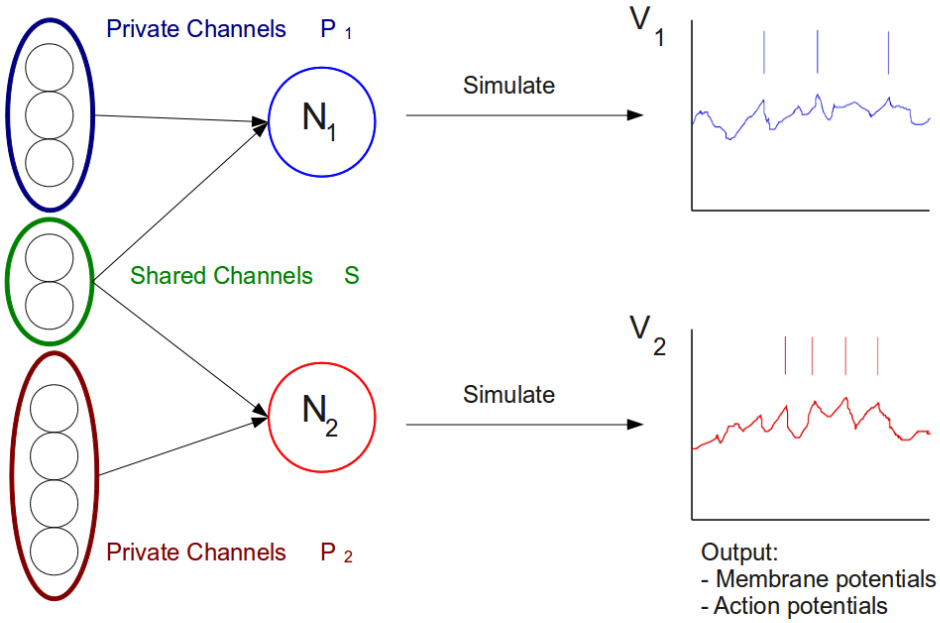

Figure 1.3: A neuron pair $N1$ and $N2$ receiving Poisson input from several sources, with two shared channels. In addition to the shared channels, both $N1$ and $N2$ receive inputs from three and four independent sources, respectively. Depending on the input configuration, the response of the neurons $N1$ and $N2$ displays varying degrees of correlation.

It turns out that there is no single solution to the above problem, but rather a set of solutions with varying number of shared and private channels per neuron pair. A second step is therefore necessary, where one needs to find which one of these configurations also causes minimal neural response correlations[9]. It is therefore necessary to define what one understands by "correlations" by defining a measure for these and then quantify the

[8] Petrovici, Bytschok and Bill, to be published

[9] While this might sound like a trivial problem - and, in some cases, it is - there are situations where it is not. Consider, for example, the configurations (2,3) and (3,4), with (x,y) standing for the number of

effects of particular input configurations on this measure. Ideally, one would like to find a way to predict these effects without performing the simulation itself.

shared and private channels, respectively. It is not immediately clear which configuration yields, for instance, less correlated spiking. The problem becomes even more complicated when the individual channels carry different spike frequencies and impinge on the neurons with different weights.

1.3 Outline

This thesis is structured as follows. Following the introduction in chapter 1, chapter 2 gives a brief description of the membrane properties of biological neurons and derives the dynamic equations for the Leaky Integrate and Fire (LIF) model, both current- and conductance-based, which will then be used throughout the rest of the thesis. Chapter 3 develops the mathematical framework on which the later predictions are based. In it, the LIF equations are solved analytically for the current based case and for the high-conductance-state approximation. The mean and variance of fluctuations induced by a Poisson point process are derived and the results are used, together with the analytic solutions to the LIF equations, to predict the distribution of a neuron membrane under the influence of multiple Poisson inputs.

In chapter 4, a measure of correlation for subthreshold fluctuations is defined and an analytic prediction is described, based on the results from chapter 3, the quality of which is investigated by comparison to computer simulations. Similarly, chapter 5 addresses the definition and prediction of a measure for spike-based correlations. The final chapter 6 contains a brief summary and a discussion of the obtained results.

2 From Biological Neurons to Leaky Integrators

The first section of this thesis will be dedicated to derivation of the so-called *Leaky Integrate and Fire* (LIF) model based on electrophysiologic properties of biological neurons. In particular, this includes clarifying the terminology and the fundamentals of the simulation setup which will be used throughout this thesis.

2.1 Fundamentals of Neurophysiology

The functionality of a neuron is essentially defined by the electrodynamic properties of its membrane, which in turn are governed by ion fluxes and the capacitance of the membrane. Living tissue is placeholder perfused by a large variety of charged chemical compunds, both intracellularly and in the extracellular medium. All cells are bounded by a cell membrane which consists of a lipid bilayer and is essentially impermeable to most of these charged particles.

However, certain channels embedded in the cellular membrane allow an exchange between the intra- and extracellular medium.

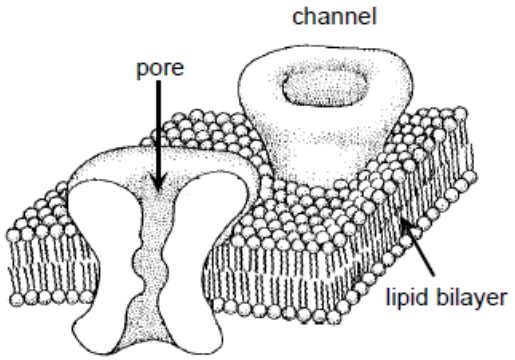

Figure 2.1: Illustration of membrane with with ion channels. (Picture taken from *Dayan and Abbott* [2001])

So-called active and passive ion channels control these ion fluxes and thereby determine key variables such as concentration gradients and charge accumulations. Despite there being a large variety of ions which influence neurodynamics, the basic functionality can be accounted for by two ion types, both positively charged: Na^+ and K^+. Inside the

neuron, the K^+ concentration $[K^+]$ is a lot higher than in the exterior of the cell. The opposite applies for Na^+-ions, whose concentration is higher outside the neuron[1].

There are several kinds of ion channels in the membrane:

- *Passive and active ion channels* can be subdivided into three categories:
  Always open (Passive), ligand-gated and voltage-gated. While the latter two are mainly responsible for synaptic-input-controlled subthreshold oscillations and action potential dynamics respectively, the first type determines the stable resting state of a neuron. Because of the concentration gradient of K^+ towards the exterior of the cell, open ion channels cause an outward K^+ ion flux, causing the cell interior to become more negatively charged. The exact opposite is true for Na^+ ions. The permeability of the K^+ ion channels is larger by far (see *Hodgkin* [1951]).
- *Active Transporters* counteract the above processes by acting as *ion pumps*, actively transporting ions opposed to the fluxes consuming energy (ATP) in the process. If there were no such ion pumps, the nonzero leakage of Na^+ would slowly disturb the concentration gradient by leaking Na^+ ions into the cell and increasing the potential inside. Ion pumps maintain the ion concentration on both sides, by exchanging three Na^+ ions from inside the cell with two K^+ ions from the extracellular medium in every pump step (see *Hodgkin* [1951]).

As a result, the cell is in an equilibrium, with a certain amount of charged particles outside and inside the cell whose overall concentrations do not change. The active channels cause a net amount of positive charge current into the neuron, by pumping more positive ions outside the neuron (Na^+) than inside (K^+). This causes a negative electric potential between the interior and exterior of the neuron membrane. As by definition the extracellular medium has zero electric potential, this so-called *rest (or leak) potential of the cell* E_L has, on average, around -65 mV. the membrane potential $V_{mem} = -65$ mV.

The value of this resting state can be explained by the *Nernst equation*, which relates the concentrations of a specific ion $[ion]_{out}$ and $[ion]_{in}$, outside and inside the neuron, to the resulting *reversal potential* E_{rev}, at which there is no net flux of this specific ion.

$$E_{rev} = \frac{R \cdot T}{z \cdot F} \cdot ln\left(\frac{[ion]_{out}}{[ion]_{in}}\right) \tag{2.1}$$

where R denotes the ideal gas constant, T the absolute temperature, z the charge of an ion, and F the Faraday constant.

In the case of K^+ ions, $E_{rev}^{K^+}$ ranges between[2] -70 mV and -90 mV. Given a hypothetical setup with $[K^+]$ as a sole ion population in a cell, the membrane potential would converge

[1] $[K^+]_{in} = 120 - 155$ mmol/l, $[K^+]_{out} = 4 - 5$ mmol/l. $[Na^+]_{in} = 7 - 11$ mmol/l, $[Na^+]_{out} = 144$ mmol/l (*Klinke* [2005])
[2] *Dayan and Abbott* [2001]

to $E_{rev}^{K^+}$ by transmitting ions through the passive ion channels, if there were no pumps counteracting this process. The same applies for sodium ions, with $E_{rev}^{Na^+} = 40 - 60$ mV.[3] Cumulatively, this results in a resting potential close to $E_{rev}^{K^+}$, because the permeability of passive K^+ ion channels is higher than the one of sodium ion channels.

From a modeling perspective, this system can be described as an electric circuit containing a capacitance C_{mem} connected to voltage sources E_{rev}^{K} and E_{rev}^{Na} via leak conductances g_{K^+} and g_{Na^+} respectively, with an additional current source representing the ion pumps. All ion flux contributions can be formally replaced by the *resting potential* E_{rest} connected to the membrane capacitance via the *leak conductance* g_L.

This RC circuit has a characteristic time constant

$$\tau_{mem} = R \cdot C_{mem} = \frac{C_{mem}}{g_L} \ . \tag{2.2}$$

This time constant is often referred to as the *membrane time constant* and describes the rate at which the membrane potential changes due to external perturbations.

Those dynamics can be described by the differential equation

$$C_{mem} \cdot \frac{dV_{mem}}{dt} = -(V_{mem} - E_{rest}) \cdot g_L \tag{2.3}$$

Before proceeding to synaptic inputs to describe the membrane potential in a non-resting state, it should be noted that only a so-called *point-neuron* is considered, meaning that any effects linked to the spatial configuration of dendrites, soma and axon are disregarded. This especially means that the propagation of membrane perturbations are neglected, a treatment of which can be found in *Gerstner and Kistler* [2002] and which most certainly do carry importance related to neural coding in certain configurations (*Emri et al.*).

2.2 Neurons with Synaptic input

Up to now, the membrane was described in its resting state. The interesting properties arise if one considers membrane fluctuations caused by activation of ligand-/voltage-gated ion channels.

The main activation source of ligand-gated ion channels is a release of neurotransmitter molecules at the bouton synapses of a neuron, where its dendrites connect to axons of other neurons. These neurotransmitters are released as a consequence of so-called action potentials (or *spikes*) from afferent neurons, which will be addressed shortly.

[3] *Dayan and Abbott* [2001]

Receptors at the dendritic end of a bouton synapse bind these neurotransmitters, which in turn activate certain types of ion channels, increasing the permeability of the cell membrane to certain ions.

The reaction of the membrane potential depends on the channels which have been activated, which in turn are specific for every synapse. Excitatory synapses frequently use glutamate as a neurotransmitter, and cause Na^+ channels to open. The influx of Na^+ ions causes a depolarization (i.e. an excitation) of the membrane towards $E_{rev}^{Na^+}$. Inhibitory synapses often use GABA to activate K^+ channels[4], allowing K^+ to escape from the cell interior, thus causing a hyperpolarization (i.e. inhibition) of the membrane towards $E_{rev}^{K^+}$[5].
In general, a change of the membrane potential due to synaptic input is called a *post synaptic potential* (PSP).

After a certain period of time (in the order of ms) the neurotransmitters detach again and are metabolyzed, causing the ligand-gated ion channels to close and allowing the leak mechanism described above to revert the cell to its resting state.

In order to model synaptic inputs, the equivalent circuit can be extended by adding time-dependent conductances g_{K^+} and g_{Na^+} connecting C_{mem} to voltage sources E_{K^+} and E_{Na^+}, respectively. Since a neuron can have multiple synapses, the model equation now becomes

$$C_{mem} \cdot \frac{dV}{dt} = g_L \cdot (E_L - V(t)) + \sum_{exc.\ i} g_i \cdot (E_{rev}^{Na^+} - V(t)) + \sum_{inh.\ j} g_j \cdot (E_{rev}^{K^+} - V(t)) \tag{2.4}$$

If the membrane potential is excited to a sufficiently high state, which can be called *the membrane threshold* V_{theshr}, an action potential is generated, which will be called an *output spike*. The generation of such spikes can be understood in more detail through the Hodgkin-Huxley model (*Hodgkin and Huxley* [1952]).

Even though the Hodgkin-Huxley model has no specific voltage threshold at which a spike is triggered, it behaves similar to what one would expect if such a threshold existed. For modeling purposes, it therefore often suffices to disregard the complex dynamics of the voltage-gated ion channels and to define a threshold voltage, which causes the emission of an action potential when reached by the membrane.

Most action potentials are also highly similar events of very short duration ($\sim$ 2 ms) and can therefore be considered as identical, singular events. In the equivalent circuit,

[4] GABA can also activate Cl^- channels, which will be neglected here

[5] It is important to mention that only few ions are sufficient for alrge local membrane potential fluctuations, thus not affecting ion concentrations and therefore keeping E_{rev}^x constant

this can be modeled by changing V_{mem} to V_{reset} to a period equal to τ_{ref} and emitting a singular pulse $\delta(t - t_s)$, where t_s is the time of the occuring action potential.

$$\begin{aligned} & V(t_s) = V_{thresh} \\ & \rightarrow \text{send action potential at time } t_s \\ & \rightarrow \text{reset: } \lim_{\substack{t \to t_s \\ t > t_s}} V(t) = V_{reset} \end{aligned}$$

The value V_{reset} is often chosen as the resting potential E_{rest}. From now on, for convenience, the specific values E^{Na^+} and $E^{K^+}_{rev}$ will be named E_{exc} and E_{inh}, respectively.

This completes the so-called LIF neuron model, which now obeys the following set of equations:

$$C_{mem} \cdot \frac{dV}{dt} = g_L \cdot (E_L - V(t)) + \sum_{exc.\ i} g_i \cdot (E^{Na^+}_{rev} - V(t) + \sum_{inh.\ j} g_j \cdot (E^{K^+}_{rev} - V(t) \tag{2.5}$$

$$\begin{aligned} V(t_s) &= V_{thresh} \\ &\rightarrow \delta_{spike}(t_s) \\ &\rightarrow \text{reset: } \lim_{\substack{t \to t_s \\ t > t_s}} V(t) = V_{reset} \end{aligned}$$

Equation (2.5) is the differential equation of a *leaky integrator*, which gives the model its name. It describes the integration of synaptic input currents $g_{syn}(t) \cdot (V(t) - E_{syn})$, with a leak term $-g_L \cdot (V(t) - E_L)$.
This equation is essential to the theoretic framework described in this thesis. In the next chapter, it is analyzed in detail.
For a complete formulation of equation (2.5), one needs to specify the shape of the conductances $g_i(t)$.

The leak conductance g_L represents the summation of passive ion channels and ion pumps working to establish the resting potential. These contributions to the total conductance can be considered constant.

The synaptic conductances however, are time dependent. There are different possibilities to model $g_{syn}(t)$ (*Gerstner and Kistler* [2002]). Throughout this thesis, the so-called exponential model (for reasons addressed in section 3.1.4) is considered. The conductances are modeled as instant rises at the arrival time of the input spike t_i, decaying afterwards along an exponential with the the *synaptic time constant* τ_{syn}:

$$g_{syn}(t) = \begin{cases} w_{syn} \cdot \exp^{-\frac{(t-t_i)}{\tau_{syn}}} & \text{if } t \geq t_i \\ 0 & \text{if } t < t_i \end{cases} \tag{2.6}$$

Similar to the membrane time constant τ_{mem}, the synaptic time constant indicates the time scale on which changes in the conductance occur, and w_{syn} are measures of the efficacy of the synapse, also called *synaptic weights*. The higher they are, the stronger the impact of the input spike will be. Values of τ_{syn} can vary greatly, in biology (see *Thompson* [1985]).

Contrary to what one might naively expect, when the membrane potential changes its equilibrium state due to synaptic conductances, its dynamics are no longer governed by its resting state time constant τ_{mem}.

Instead, one obtains an *effective time constant* τ_{eff} (see *Shelley et al.* [2002]):

$$\tau_{eff} = \frac{C_{mem}}{g_{inh}(t) + g_{exc}(t) + g_L} \ . \tag{2.7}$$

This equation will be formally derived in the next chapter, section (3.1)

The total synaptic conductance can be written as

$$g_{syn}(t) = w_{syn} \sum_{t_{spk}} \exp^{-\frac{(t-t_{spk})}{\tau_{syn}}} \cdot \Theta(t - t_{spk}) \ . \tag{2.8}$$

This equation shows the total conductance as a linear sum of all conductances of single input spikes.

This linearity is a result of *spatial and temporal summation of synaptic inputs*, which are essential principles of membrane dynamics. It means that the impact (here: conductance rise) of multiple afferent synapses (spatial summation), as well as from afferent spikes different times (temporal summation) can be simply added to yield the total conductance.

Mathematically, this means that kernels such as the exponential for the conductance can be summed to yield the total conductance.

3 On the membrane potential of LIF models

Before adressing the issue of correlated neural dynamics, this chapter will discuss the behavior of the membrane potential in a single conductance-based Leaky Integrate and Fire unit and its statistical properties.

As conductance-based models have more relevance both in the biological context and for the FACETS/BSS hardware, the current-based LIF model will be useful as it allows a more straightforward analytic treatment. The main goal of this chapter will be to derive the membrane potential time course of the conductance-based LIF model from its differential equation, which will allow calculating statistical measures of its behavior.

For the synaptic input, the biologically most relevant case of Poisson-distributed excitatory and inhibitory spikes will be considered, which in turn trigger post-synaptic potentials. These PSPs are essential for the membrane potential traces, as they represent the defining dynamic component. The derivation of the PSP time course will be achieved through several approximations of the differential equation of the conductance-based LIF model, eq. (2.5):

$$C_{mem} \cdot \frac{dV}{dt} = -g_L \cdot (V(t) - E_L) - \sum_{syn \in \{exc,inh\}} g_{syn}(t) \cdot (V(t) - E_{syn}) \qquad (3.1)$$

At the end of this chapter, the membrane potential amplitude distributions will be discussed, showing parameter regions where they can be assumed as Gaussians. This will be important in the following chapters, as these statistical properties have a significant influence on the analytic prediction of correlation measures.

3.1 Theoretical approximation of the membrane potential time course

The goal of the methods described in this section is to be able to understand and predict the dynamics of the membrane potential when stimulating the neuron through afferent spikes, which in turn evoke subthreshold variations of the membrane potential, the PSPs.

As described in the previous, introductory chapter, voltage-gated ion channels are equivalent to conductances from the membrane to the respective reversal potentials, whose

competition determine both E_L and τ_{mem}. Synaptic input causes the opening of additional channels, thus modifying the conductances towards the same reversal potentials, defining a new, dynamic value $V_{eff}(t)$ for the equilibrium membrane potential and also modifying the membrane time constant towards a new, likewise dynamic value $\tau_{eff}(t)$.

One can regard the typical time course of a PSP as the membrane following V_{eff} with a lag determined by τ_{eff}.

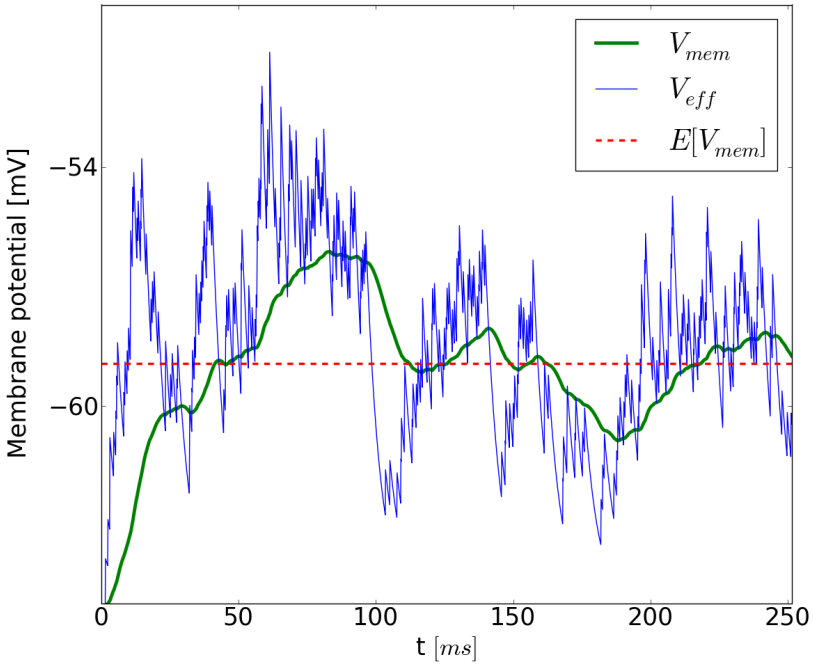

Figure 3.1: The membrane potential and effective potential in a comparison for excitatory inputs. One can see that V_{eff} is more susceptible to inputs, as it reacts immediately to synaptic inputs. As V_{mem} decays towards V_{eff} along an exponential with time constant τ_{eff}, the peaks of the PSPs become smaller as a result. The mean values of both traces are the same, although the variance of V_{eff} is higher.

These considerations are easy to reproduce analytically by incremental modifications to the LIF equation (3.1):

$$C_{mem} \cdot \frac{dV}{dt} = -g_L \cdot (V(t) - E_L) - \sum_{syn \in \{exc,inh\}} g_{syn}(t) \cdot (V(t) - E_{syn}) \tag{3.2}$$

$$\Leftrightarrow C_{mem} \cdot \frac{dV}{dt} = \sum_{i \in \{Leak,syn\}} g_i \cdot (E_i - V(t)) \tag{3.3}$$

Dividing both sides by the total conductance $g_{tot}(t) = \sum g_i(t)$ yields

$$\frac{C_{mem}}{g_{tot}(t)} \cdot \frac{dV}{dt} = \frac{\sum g_i(t) \cdot E_i}{g_{tot}(t)} - V(t) \tag{3.4}$$

Now the dynamic equilibria discussed above can be defined

$$\tau_{eff} = \frac{C_{mem}}{g_{tot}(t)} \quad \text{and} \quad V_{eff} = \frac{\sum g_i(t) \cdot E_i}{g_{tot}(t)} \tag{3.5}$$

Substituting these into (3.4) finally yields

$$\tau_{eff}(t) \cdot \frac{dV}{dt} = V_{eff}(t) - V(t) \tag{3.6}$$

which gives the mathematical representation of the phenomenologic considerations above.

In general, eq. (3.6) can not be solved analytically, since, in addition to $V(t)$, τ_{eff} and V_{eff} are also time-dependent and can take on complex forms, depending on synaptic dynamics and the nature of the input. However, under certain circumstances, approximations can be made which allow an analytic treatment and ultimately yield excellent predictions, as shall be described in the following.

3.1.1 Current-based approximation in the Leaky Integrate and Fire Model

One possible way to approximate and simplify equation (3.6), is to make a so-called current-based approximation. This implies that the PSPs are not caused by conductance, but rather directly by ion currents I_i passing through the ion channels of the membrane. Analogously to equation (2.8), these can be modeled as exponentially decaying synaptic currents

$$I_{syn}(t) = i_{syn} \sum_{t_{spk}} \exp^{-\frac{(t-t_{spk})}{\tau_{syn}}} \cdot \Theta(t - t_{spk}) \tag{3.7}$$

Note that i_{syn} are the equivalents to the synaptic weights w_{syn} that are used in the conductance-based model. They both determine the height of the PSPs in the respective model, but have different scales for similar PSPs.
In effect, the conductance in this approximation will be held constant at g_L, resulting in a time-independent membrane time constant τ_{mem}. Obviously, reversal potentials are not considered in these approximations. Overall, considering equation (3.5), the following substitutions result from these thoughts:

$$\tau_{eff}(t) = \frac{C_{mem}}{g_{tot}(t)} \longrightarrow \tau_{mem} = \frac{C_{mem}}{g_L} \tag{3.8}$$

$$V_{eff} = \frac{\sum g_i(t) \cdot E_i}{g_{tot}(t)} \longrightarrow V_{eff} = \frac{\sum I_i(t)}{g_L} \tag{3.9}$$

with $I_L = g_L \cdot E_L$ as the *leak current*. This simplifies the form of the effective potential in the current-based approximation, V_{eff}, and allows an analytic solution of equation (3.6), which transforms into

$$\tau_{mem} \cdot \frac{dV}{dt} = V_{eff}(t) - V(t) \tag{3.10}$$

$$\Leftrightarrow \tau_{mem} \cdot \frac{dV}{dt} = \sum_{i \in \{L,exc,inh\}} \frac{I_i(t)}{g_L} - V(t) \tag{3.11}$$

The consequences of this approximation are:

- The fact that $\tau_{mem} = const.$ makes the shapes of all synaptic PSPs identical for a synapse, because the membrane potential basically reacts in the same way for every synaptic input, as the charging rate of the membrane does not change during the simulation.
- V_{eff} has no influence from reversal potentials, making the PSP amplitude independent from the potential value given at the time of the occurance of the afferent spike. This is fundamentally different from the conductance-based model, when the input spike arrives at a time when the membrane potential is close to the corresponding reversal potential (excitatory or inhibitory), the induced PSP will be small on account of the term proportional to $(V(t) - E_{rev})$. In these regions saturation effects can be seen (in fig. 3.3), which do not appear in the current-based model.

The second point is especially important, as it linearizes the differential equation for the membrane potential, because there is no dependence on the value of the membrane potential on the right hand side of the equation, and it does not matter at what potential the current-induced PSP was triggered.

This linearity of the equation ensures that instead of computing the effect of the sum of different current sources $V(t - \vec{t_{spk}})$, it is possible to compute the membrane potential resulting from a single afferent spike and then take the sum $\sum_{t_{spk}} V(t - t_{spk})$,

$$V(t - \vec{t_{spk}}) = \sum_{t_{spk}} V(t - t_{spk}) \ . \tag{3.12}$$

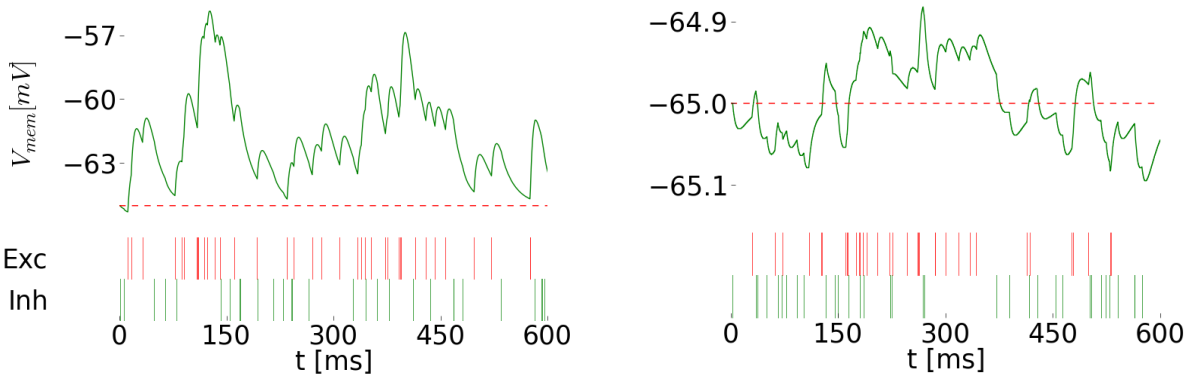

(a) Conductance based LIF model ($w = 10^{-2}\mu S$)

(b) Current based LIF model ($i = 10^{-2}nA$)

Figure 3.2: Figures show a comparison of both models in a state with equal synaptic rates $\nu_{inh} = \nu_{exc} = \nu = 50Hz$ and also equal synaptic weights (i and w respectively).
One can see the influence of the reversal potentials $E_{inh} = -70$ and $E_{exc} = 0$ mV on fig. 3.2a. The average potential is at ~ -62 mV. In spite of equal synaptic weights w, the excitatory PSPs are, on average, about $\left|\frac{(V(t)-E_{exc})}{(V(t)-E_{inh})}\right| \approx 8$ times as high as the inhibitory PSPs (see (3.1)).
In fig. 3.2b, there are no reversal potentials involved. The PSPs are equal, the membrane potential oscillates around the resting potential at -65 mV.

In fact, this approximation yields the dynamic equations of the eponymous current-based LIF model (see *Gerstner and Kistler* [2002]) and represents a significant simplification of the membrane subthreshold dynamics, which will be of interest especially later in this chapter, as well as in the following one.

In the next section, the differential equation describing the current-based LIF model will be used to derive a closed-form expression for the shape of current-based PSPs.

Solving the current-based Leaky Integrator Differential Equation

To solve the differential equation (3.6) and calculate the shape of a single PSP, two states will be considered. These two states will be described by two effective potentials, as they represent the dynamic equilibria of the membrane potential. The first state, described by $V_{eff}(t)$, is an unspecified effective potential and $V'_{eff}(t)$ - the effective potential with exactly the same progression as $V_{eff}(t)$ except for an additional input spike that occurs at time $t = 0$.

Let $V_{psp}(t)$ be the difference of the effective membrane potential time courses resulting from the input spike.

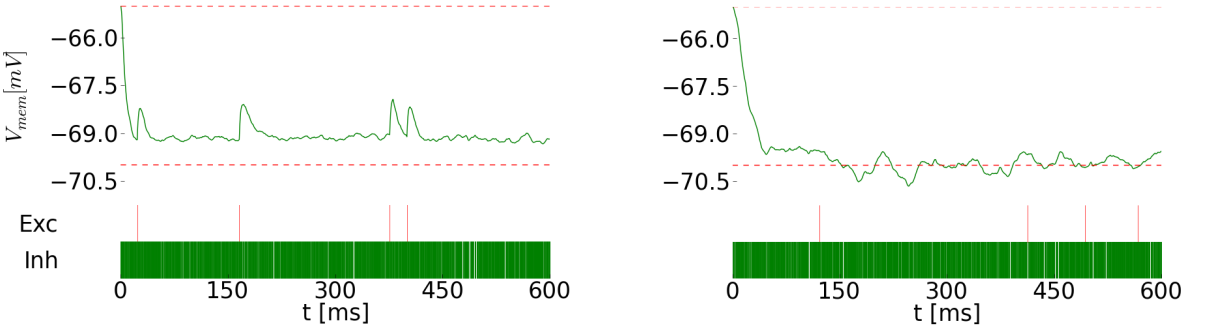

(a) Conductance based LIF model, bounded at E_{inh} (b) Current based LIF model, no lower bound by E_{inh}

Figure 3.3: Both neurons were stimulated by high-frequent inhibitory input (5000 Hz) and sparse excitatory input spikes (10 Hz) with $i = 10^{-2}$ nA and $w = 10^{-2}\mu$S. In the conductance based case in fig. 3.3a, the membrane potential ranges between the resting potential (−65 mV) and E_{inh} (−70 mV).
As the amplitude of the PSPs decreases linearly with smaller distance to E_{inh}, the potential never falls below E_{inh}, but remains close to it due to the high-frequent inhibitory inputs. Note that excitatory spikes induce large PSPs due to the distance of V_{mem} to $E_{exc} = 0$ mV.
In 3.3b, there is no such limitation because the PSPs remain the same regardless of the membrane potential value. In principle, the membrane potential can take on arbitrarily low (or high) values. Excitatory PSPs are as small as inhibitory ones.

$$\Delta V_{eff}(t) := V'_{eff}(t) - V_{eff}(t) \tag{3.13}$$

From eq. 3.9, one finds

$$V_{eff} = \frac{\sum I_i(t)}{g_L} \quad \xrightarrow{\text{spike } x} \quad V' = V_{eff} + \frac{I_x(t)}{g_L} \tag{3.14}$$

This indicates that the difference of the effective potentials lies in the PSP, triggered by an input spike x, causing a synaptic current $I_x(t)$, which has an exponential time course in eq. (3.7):

$$\Delta V_{eff}(t) = \frac{I_x(t)}{g_L} \tag{3.15}$$

Inserting both $V'(t)_{eff}$, $V(t)_{eff}$, and the respective membrane potentials $V'(t)$, $V(t)$ into the main equation (3.10) results in

$$\tau_{mem} \cdot \frac{dV'(t)}{dt} = V'_{eff}(t) - V'(t) \tag{3.16}$$

$$\tau_{mem} \cdot \frac{dV(t)}{dt} = V_{eff}(t) - V(t) \tag{3.17}$$

Now, one can restrict the possible input currents $I_x(t)$ as a result of synaptic inputs, and can therefore substituted

$$I_x(t) \longrightarrow I_{syn}(t) = i_{syn} \cdot e^{-\frac{t}{\tau_{syn}}} \tag{3.18}$$

Subtracting eq. (3.17) from (3.16) and dividing by τ_{mem} yields

$$\tau_{mem} \cdot \frac{d(V' - V)}{dt} = \frac{1}{\tau_{mem}} \cdot \left(\underbrace{\frac{I_{syn}(t)}{g_L}}_{=\Delta V_{eff}(t)} - \underbrace{V_{psp}(t)}_{:=V'(t)-V(t)} \right) \tag{3.19}$$

This has the form of an Ordinary Differential Equation of first order in time:

$$\frac{d}{dt} f(t) = a(t) \cdot f(t) + b(t) \tag{3.20}$$

A solution for this particular type of ODE is guaranteed to exist and can be expressed as (see *Hartman* [2002])

$$f(t) = e^{F(t)} \left[\int_0^t b(x) \cdot e^{-F(x)} \, dx + C \right] \tag{3.21}$$

$$\text{with } F(x) = \int_0^x a(x') \, dx' \tag{3.22}$$

For equation (3.19), one can simply replace the dependencies by

$$a(t) = -\frac{1}{\tau_{mem}} \tag{3.23}$$

$$b(t) = \frac{I_{syn}(t)}{\tau_{mem} \cdot g_L} = \frac{i_{syn}}{g_L \cdot \tau_{mem}} \cdot e^{-\frac{t}{\tau_{syn}}} \tag{3.24}$$

and see that

$$F(x) = -\frac{x}{\tau_{mem}} \tag{3.25}$$

so now the post-synaptic time course $V_{psp}(t)$ can be easily computed by integrating

$$V_{psp} = \underbrace{e^{-\frac{t}{\tau_{mem}}}}_{e^{F(t)}} \left[\int_0^t \underbrace{\frac{i_{syn}}{g_L \cdot \tau_{mem}} \cdot e^{-\frac{x}{\tau_{syn}}}}_{b(x)} \cdot \underbrace{e^{\frac{x}{\tau_{mem}}}}_{e^{-F(x)}} dx + C \right] \tag{3.26}$$

This yields[1]

$$V_{psp} = \frac{i_{syn}}{g_L \cdot \tau_{mem} \cdot (\frac{1}{\tau_{syn}} - \frac{1}{\tau_{mem}})} \cdot \left[e^{-\frac{t}{\tau_{mem}}} - e^{-\frac{t}{\tau_{syn}}} \right] \tag{3.27}$$

With the substitution

$$\tau_c := \left[\frac{1}{\tau_{syn}} - \frac{1}{\tau_{mem}} \right]^{-1} \tag{3.28}$$

the result of this computation can finally be written down as:

PSP time course for a current-based LIF neuron

The synaptic PSP triggered by synaptic currents I_{syn} with the time constant τ_{syn} in a current-based LIF neuron with leak current I_L, leak conductance g_L, and membrane time constant τ_{mem}:

$$V_{psp}(t) = \frac{i_{syn} \cdot \tau_c}{g_L \cdot \tau_{mem}} \cdot \left[e^{-\frac{t}{\tau_{mem}}} - e^{-\frac{t}{\tau_{syn}}} \right] \tag{3.29}$$

$$\tau_{mem} = \frac{C_{mem}}{g_L} \qquad \tau_c = \left[\frac{1}{\tau_{syn}} - \frac{1}{\tau_{mem}} \right]^{-1} \qquad \overline{V_{eff}} = \frac{\sum_i \overline{I_{syn}}}{g_L}$$

with $i \in \{L, syn\}$

In the following, a similar approach will be used to derive an analytic expression for the shape of a PSP for the more biologically plausible conductance-based LIF model. While, as described earlier, the general case has no analytic solution, biological neurons often operate in a regime called a high-conductance state (*Rudolph and Destexhe* [2006]) which allows the derivation of a closed-form expression.

[1] In the result, $C = 0$ because the initial condition is $V_{psp}(t = 0) = 0$

3.1.2 Approximation of the Leaky Integrate and Fire Model for a High Conductance State

The *high conductance state* is a state of the membrane potential generated and sustained by high-frequency synaptic input[2] with relatively low synaptic weights w_i, w_e. This results in a constantly high synaptic conductance $g_{syn}(t) \approx const.$ which is comparable to, or even exceeds the leak conductance, g_L.

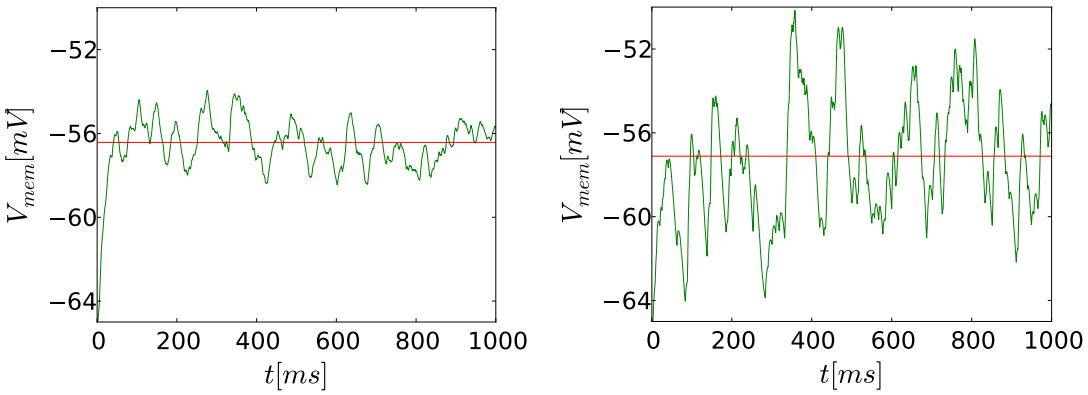

(a) high conductance state

(b) low-frequency stimulation

Figure 3.4: A comparison of conductance-based, subthreshold membrane potential oscillations with $V_{rest} = -65mV$. Figure (3.4a) shows a simulation with $\nu_{exc} = \nu_{inh} = 2$ kHz, $w_{inh} = w_{exc} = 10^{-3}\mu$S.
Simulation (3.4b) was conducted with $\nu_{exc} = \nu_{nnh} = 200$ Hz, $w_{inh} = w_{exc} = 10^{-2}\mu$S resulting in the same average membrane potential, due to $w_{syn} \cdot \nu_{syn} = const.$, but with a significantly higher variance. This also causes the membrane to come close to the inhibitory resting potential, dynamically altering inhibitory PSP amplitudes, which is essentially the reason for which the general conductance-based LIF equation has no closed-form solution.

In the limit of high input frequencies and low synaptic weights, one expects the perturbations of the total conductance to remain small compared to its average value. This would validate the first-order approximation

$$g_{tot} \approx \overline{g_{tot}(t)} = \overline{g_{exc}(t) + g_{inh}(t)} + g_L \quad \gg g'_{syn} \ , \tag{3.30}$$

with g'_{syn} being the contribution to the conductance from a single synapse. This will allow to simplify and eventually solve the equation (3.6) in a similar way as for the current-based case.

[2] in this thesis: Poisson-distributed input

The required mathematical formalism is the subject of the next section, which aims to derive a general formula for computation of statistical properties of linear superpositions of Poisson-process-induced fluctuations.

3.1.3 Statistical Characterization of Additive Fluctuations induced by Poisson Processes

Consider a sequence of points in time generated by a Poisson process $t_i \in \vec{t} = \{t_1, ..., t_n\}$.

Let $\kappa(t)$ be a kernel which is triggered by above process. Such a kernel marks the impact of the point process on a continuous function of time $Y(t)$.

Assuming superposition linearity, the total effect of the Poisson process becomes

$$Y(t) = \sum_{t_i \leq t} \kappa(t - t_i) \ . \tag{3.31}$$

The goal of this section is to find general expressions for the computation of the mean and variance of $Y(t)$ for a given kernel $\kappa(t_i)$.

One can start by considering a poisson process with a rate λ and N events for a continuous variable $t \in [0, T]$:

$$p_\lambda(N) = \frac{e^{-\lambda \cdot T} \cdot (\lambda \cdot T)^N}{N!} \tag{3.32}$$

First, one can look at the weighted, conditinional expectation values, which are the expectation values for a predefined number of spike occurences, weighted with $p_\lambda(N_{spk})$.

In case of zero occuring events (this result is possible, despite $\lambda \neq 0$), this would result in

$$E[Y] = E_0 \overset{p_\lambda(0)}{=} 0 \tag{3.33}$$

For one occurence, one will have

$$E_1 = p_\lambda(1) \cdot \int_0^T p_1(t) \cdot \kappa(T - t)\, dt = \lambda \cdot e^{-\lambda} \cdot \int_0^T \frac{1}{T} \cdot \kappa(T - t)\, dt \tag{3.34}$$

with $\frac{1}{T}$ being the probability density of the occurence of one event in the interval $t \in [0, T]$. For N events, this would transform into

$$p_N(t_1, \ldots, t_N) = \prod_{i=1}^{N} p_i(t_i) = \frac{1}{T^N} \tag{3.35}$$

$$\text{(Poissonian events are independent of each other)} \tag{3.36}$$

Applying this, two occuring events at rate λ yield

$$E_2 = E_0 + E_1 + \int_0^T \int_0^T p_2(t_1, t_2) \cdot (\kappa(T - t_1) + \kappa(T - t_2))\, dt_1\, dt_2 \tag{3.37}$$

The sum of these terms gives the total expectation value in case of two arrivals, since it is a sum over all possibilities of occuring spikes for a predefined input rate.

In general, despite having rate λ, one can not limit the amount of occuring events. This means that one has to consider a sum with infinite elements for the general expectation value, E_λ.

$$E_\lambda = \sum_{i=1}^{\infty} p_\lambda(i) \underbrace{\int_0^T \ldots \int_0^T}_{\times i} \underbrace{p_i(t_1, \ldots, t_i)}_{\frac{1}{T^i}} \cdot \sum_{j=1}^{i} \kappa(T - t_j)\, dt_1 \ldots\, dt_i \tag{3.38}$$

$$E_0 = 0 \Rightarrow \text{ summation starts at } i = 1 \tag{3.39}$$

Simplifying and reorganizing this equation ($\int \sum \cdots = \sum \int \ldots$) yields

$$E_\lambda = \sum_{i=1}^{\infty} \frac{p_\lambda(i)}{T^i} \sum_{j=1}^{i} \int_0^T \ldots \int_0^T \kappa(T - t_j)\, dt_1 \ldots\, dt_i \tag{3.40}$$

$$= \sum_{i=1}^{\infty} \frac{p_\lambda(i)}{T^i} \sum_{j=1}^{i} \underbrace{\int_0^T \ldots \int_0^T}_{i-1} \underbrace{\left[\int_0^T \kappa(T - t_{j'})\, dt_{j'} \right]}_{=A} dt_1 \ldots\, dt_{j'-1}\, dt_{j'+1} \ldots\, dt_i \tag{3.41}$$

This double sum then collapses into

$$E_\lambda = A \cdot \sum_{i=1}^{\infty} \frac{p_\lambda(i)}{T^i} \sum_{j=1}^{i} \underbrace{\int_0^T \dots \int_0^T dt_1 \dots dt_{j'-1}\, dt_{j'+1} \dots dt_i}_{T^{i-1}} \tag{3.42}$$

$$= A \cdot \sum_{i=1}^{\infty} \frac{p_\lambda(i)}{T^i} \sum_{j=1}^{i} T^{i-1} = A \cdot \sum_{i=1}^{\infty} \frac{p_\lambda(i) \cdot i}{T} \tag{3.43}$$

Substituting $p_\lambda(i)$ from eq. (3.32) finally yields

$$E_\lambda = \sum_{i=1}^{T} \frac{e^{-\lambda \cdot T} \cdot (\lambda \cdot T)^i}{i!} \tag{3.44}$$

$$= e^{-\lambda \cdot T} \cdot \lambda \cdot A \cdot \underbrace{\sum_{i=1}^{\infty} \frac{(\lambda \cdot T)^{i-1}}{(i-1)!}}_{e^{\lambda \cdot T}} \tag{3.45}$$

$$= \lambda \cdot A \tag{3.46}$$

The total expectation value is then

$$E_\lambda[Y] = \lambda \cdot \int_0^T \kappa(t)\, dt \tag{3.47}$$

This can not be directly applied for variances, which have a quadratic dependence on the summed kernels.

$$Var[Y] = E[(Y - E[Y])^2] = E[Y^2] - E[Y]^2 \tag{3.48}$$

However, to compute the variance, a similar derivation can be used like the one for the expectation value (3.47).

The term $E[Y]^2$ can be computed via (3.47), but the first term $E[Y^2]$ requires a formula for the computation of squared kernels of random variables, as formula (3.47) covers only linear superposition.

Nevertheless, it is possible to start with equation (3.38), this time with a squared sum of kernels $\kappa(t)$:

$$E_\lambda[Y^2] = \sum_{i=1}^{\infty} p_\lambda(i) \underbrace{\int_0^T \dots \int_0^T}_{\times i} \underbrace{p_i(t_1, \dots, t_i)}_{\frac{1}{T^i}} \cdot \left[\sum_{j=1}^{i} \kappa(t_j) \right]^2 dt_1 \dots dt_i \tag{3.49}$$

This expression can be decomposed into two terms:

$$\left[\sum_{j=1}^{i}\kappa(t_j)\right]^2 = \underbrace{\sum_{j=1}^{i}\kappa^2(t_j)}_{(1)} + \underbrace{\sum_{j=1}^{i}\sum_{k=1}^{i}\kappa(t_j)\cdot\kappa(t_k)}_{(2)} \ . \tag{3.50}$$

Plugging term (1) back into equation (3.49) yields

$$E_\lambda^{(1)}[Y^2] = \sum_{i=1}^{\infty} p_\lambda(i) \int_0^T \dots \int_0^T \frac{1}{T^i} \sum_{j=1}^{i} \kappa^2(t_j)\, dt_1 \dots\, dt_i \ , \tag{3.51}$$

which can be computed by using the derived formula (3.47). In this case, the sum consists of the kernels $\kappa^2(t_i)$, allowing to use the same method that was already derived for a linear summation of kernels.

As a result, the computation of term (1) will be

$$E_\lambda^{(1)}[Y^2] = \lambda \int_0^T \kappa^2(t)\, dt \tag{3.52}$$

Now, term (2) needs to be evaluated in equation (3.49):

$$E_\lambda^{(2)}[Y^2] = \sum_{i=2}^{\infty} p_\lambda(i) \int_0^T \dots \int_0^T \frac{1}{T^i} \sum_{j=1}^{i}\sum_{k=1}^{i} \kappa(t_j)\cdot\kappa(t_k)\, dt_1 \dots\, dt_i \tag{3.53}$$

$$\sum_{j=1}^{i}\sum_{k=1}^{i}\kappa(t_j)\cdot\kappa(t_k) = \sum_{j<k} 2\cdot\kappa(t_j)\cdot\kappa(t_k) \tag{3.54}$$

The index i starts at $i = 2$ in equation (3.53), because at least two events are necessary to examine the product of two separated kernels $\kappa(t_j)$, $\kappa(t_k)$.

Equation (3.53) can now be further simplified:

$$E_\lambda^{(2)}[Y^2] = \sum_{i=2}^{\infty} \frac{2 \cdot p_\lambda(i)}{T^i} \sum_{j<k}^{i} \int_0^T \dots \int_0^T \kappa(t_j) \cdot \kappa(t_k)\, dt_1 \dots\, dt_i \tag{3.55}$$

$$\overset{(3.41)}{=} \sum_{i=2}^{\infty} \frac{2 \cdot p_\lambda(i)}{T^i} \sum_{j<k}^{i} \underbrace{\int_0^T \dots \int_0^T dt_1 \dots\, dt_{j'-1}\, dt_{j'+1} \dots\, dt_{k'-1}\, dt_{k'+1} \dots\, dt_i}_{i-2} \cdot \tag{3.56}$$

$$\cdot \underbrace{\left[\int_0^T \kappa(t_{j'})\, dt_{j'} \int_0^T \kappa(t_{k'})\, dt_{k'} \right]}_{:=A_{j,k}^2}$$

This equation can be modified analogously to (3.42), computing non-framed integrals:

$$E_\lambda^{(2)}[Y^2] = \sum_{i=2}^{\infty} \frac{2 \cdot p_\lambda(i)}{T^i} \cdot T^{i-2} \cdot \sum_{j<k}^{i} A_{j,k}^2 \tag{3.57}$$

Here, it is possible to exploit the relation $\sum_{j<k}^{i} = \frac{(i-1)\cdot i}{2}$, yielding

$$E_\lambda^{(2)}[Y^2] = \sum_{i=2}^{\infty} \frac{p_\lambda(i)}{T^2} \cdot (i-1) \cdot i \cdot A_{j,k}^2 \tag{3.58}$$

Eventually, one can write down the Poisson-probabilities $p_\lambda(i)$ explicitly, and find a final form of the expectation value for the computation of the term (2):

$$E_\lambda^{(2)}[Y^2] = \sum_{i=2}^{\infty} \frac{e^{-\lambda \cdot T} \cdot (\lambda \cdot T)^i}{i! \cdot T^2} \cdot (i-1) \cdot i \cdot A_{j,k}^2 \tag{3.59}$$

$$= \lambda^2 \cdot e^{-\lambda \cdot T} \cdot A_{j,k}^2 \cdot \underbrace{\sum_{i=2}^{\infty} \frac{(\lambda \cdot T)^{i-2}}{(i-2)!}}_{=e^{\lambda \cdot T}} \tag{3.60}$$

$$= \lambda^2 \cdot A_{j,k}^2 \tag{3.61}$$

As $A_{j,k}^2$ constitutes the squared integral of the kernel $\kappa(t)$, as defined in eq. (3.57), one can express it as the squared mean of the sum of random variables $E[X]^2$

$$E_\lambda^{(2)}[Y^2] = \left[\lambda \int_0^T \kappa(t)\, dt \right]^2 = E[Y]^2 \tag{3.62}$$

This means that the full expression of the variance yields

$$Var_\lambda[Y] = E^{(1)}[Y^2] + E^{(2)}[Y^2] - E^2[Y] \tag{3.63}$$

$$\text{eq. (3.52), (3.62)} \Rightarrow Var_\lambda[X] = \lambda^2 \cdot A \tag{3.64}$$

$$\Rightarrow Var_\lambda[Y] = \lambda^2 \cdot \int_0^T \kappa(T-t)\,dt \tag{3.65}$$

The same result can also be derived in an intuitively more appealing way, which will be shown in the following.

First, the mean of $Y_1(t)$ in case of one occuring event in $t \in [0,T]$ can be computed:

$$E[Y_1] = \frac{1}{T} \underbrace{\int_0^T \kappa(T-t)\,dt}_{:=A} = \frac{A}{T} \tag{3.66}$$

$$\tag{3.67}$$

All occuring events in $[0,T]$ generated by a Poisson process arrive independently of each other, thus have the same single mean $E[Y_1]$. Due to the linear superposition of the kernels, the mean total effect of the Poisson process $E_\lambda[Y]$ can be written as a sum of means $E[Y_1]$ for long intervals T,

$$E_\lambda[Y] = \sum^N E[Y_1]\ , \tag{3.68}$$

with N being the total number of occuring events. If the time window $[0,T]$ is long enough, then the total number of expected events can be expressed as $N = \lambda \cdot T$. This leads to the total mean of $Y(t)$:

$$E_\lambda[Y] \overset{N=\lambda\cdot T}{=} \lambda \cdot T \cdot E[Y_1] = \lambda \cdot A \tag{3.69}$$

$$= \lambda \cdot \int_0^T \kappa(T-t)\,dt \tag{3.70}$$

This can be identified with the result from (3.47).
In the same fashion it is possible to derive the variance $Var[Y]$. At first, the variance of the total effect of one single occuring event $Var[Y_1]$ will be computed:

$$Var[Y_1] = E[Y_1^2] - E[Y_1]^2 \tag{3.71}$$

$$\overset{(3.66)}{=} \underbrace{\frac{1}{T}\int_0^T \kappa^2(T-t)\,dt}_{:=A_2} - \left(\frac{A}{T}\right)^2 \tag{3.72}$$

Again, one can reach the same result with the following intuitive reasoning, one can express the total variance of $Var[Y]$ as the sum of variances of N independent occurences:

$$Var[Y] = \sum^N Var[Y_1] \tag{3.73}$$

For long intervals $[0, T]$, again, one can therefore approximate $N = \lambda \cdot T$, which leads to

$$Var_\lambda = N \cdot Var[Y_1] = \lambda \cdot T \cdot \left[\frac{A_2}{T} - \left(\frac{A}{T}\right)^2\right] \tag{3.74}$$

$$= \lambda \cdot \left[A_2 - \frac{A^2}{T}\right] \tag{3.75}$$

For long intervals T, the second term vanishes. This leads to the final result

$$Var_\lambda[Y] = \lambda \cdot \int_0^T \kappa^2(T-t)\,dt\ , \tag{3.76}$$

which is of course identical with (3.78).

The two essential results of this section, $E_\lambda[Y]$ and $Var_\lambda[Y]$ will be summarized briefly:

The total expectation value $E_\lambda[Y]$ and variance $Var_\lambda[Y]$ of a variable $Y(t)$ representing a linear superposition of kernels $\kappa(t)$ triggered by a Poisson point process with rate λ are:

$$E_\lambda[Y] = \lambda \cdot \int_0^T \kappa(t)\,dt \tag{3.77}$$

$$Var_\lambda[Y] = \lambda \cdot \int_0^T \kappa^2(t)\,dt \tag{3.78}$$

3.1.4 Characterization of the Synaptic Conductance

The results from the previous section will serve in validating the first-order approximation from eq. (3.30), as they will be used to derive analytic expressions for the mean and the variance of both the synaptic conductance and the membrane potential.

At this point, it is important to stress the generality of the methods described throughout the following sections. While the following formalism can be applied to arbitrary shapes of spike-induced kernels, for the synaptic conductance, we consider the case of exponential kernels (see eq.(2.8), which is experimentally motivated by the hardware model implementation, which is, in turn, based on empirical evidence from biological measurements. This will have immediate consequences for the prediction of the membrane potential time course.

From eq. (2.8), one can calculate the total membrane conductance of a neuron

$$g_{tot}(t) = g_{syn}(t) + g_L \tag{3.79}$$

$$= \sum_{syn} w_{syn} \sum_{spikes} \exp^{-\frac{(t-t_{spk})}{\tau_{syn}}} \cdot \Theta(t - t_{spk}) + g_L \tag{3.80}$$

For a single synapse stimulated by a poisson spike train, one can identify the following characteristics:

$$\rightarrow \text{conductance course } \kappa(t) = w_{syn} \cdot e^{-\frac{t}{\tau_{syn}}} \tag{3.81}$$

$$\rightarrow \text{input rate } \nu_{syn} \text{ (corresponds to the } \lambda \text{ in the standard Poisson notation)} \tag{3.82}$$

$$\rightarrow \text{simulation time } T_{sim} \tag{3.83}$$

Then, one can directly apply equation (3.77) to find

$$E[g_{syn}] = \nu_{syn} \cdot \int_0^{T_{sim}} w_{syn} \cdot e^{-\frac{t}{\tau_{syn}}} \, dt \tag{3.84}$$

This integral is easy to compute, leading to the solution

$$E[g_{syn}] = \nu_{syn} \cdot w_{syn} \cdot \tau_{syn} \tag{3.85}$$

By making the appropriate substitutions of the parameters from (3.81), (3.82), (3.83) into equation (3.78), one directly obtains the variance of the conductance course:

$$Var[g_{syn}] = \nu_{syn} \cdot \int_0^{T_{sim}} \left[w_{syn} \cdot e^{-\frac{t}{\tau_{syn}}} \right]^2 dt \tag{3.86}$$

$$= \frac{1}{2} \cdot \nu_{syn} \cdot w_{syn}^2 \cdot \tau_{syn} \tag{3.87}$$

With $E[g_{syn}]$ and $Var[g_{syn}]$ now known for single synapses, the extrapolation to $E[g_{tot}]$ and $Var[g_{tot}]$ is trivial, due to the spatial summation principle and the assumed independence of the afferent spike trains from different synapses (see p. 13).
Again, the results for the inhibitory and excitatory values can be added like in eq. (3.30).

This leads to the following summarizing conclusion:

Given the input rates ν_{syn}, the synaptic weights w_{syn} and the synaptic time constants[a] τ_{syn} for every synapse, as well as the leak conductance g_L, the variance and mean of the synaptic conductance in the LIF model are

$$\overline{g_{tot}} = \sum_{syn} \nu_{syn} \cdot w_{syn} \cdot \tau_{syn} + g_L \tag{3.88}$$

$$Var[g_{tot}] = \frac{1}{2} \cdot \sum_{syn} \nu_{syn} \cdot w_{syn}^2 \cdot \tau_{syn} \tag{3.89}$$

[a] In later simulations, both synaptic time constants, for excitation and inhibition, will be set equal to simplify the computations

These results represent a significant progress because now the total conductance g_{tot} in the effective potential V_{eff} from eq. (3.5) can be assumed, in a first-order aproximation, to have no time dependency:

$$V_{eff}(t) = \frac{\sum_{syn} g_{syn}(t) \cdot E_{syn}}{g_{tot}(t)} \xrightarrow{g_{tot}(t) \approx const.} \frac{\sum_{syn} g_{syn}(t) \cdot E_{syn}}{\overline{g_{tot}(t)}} \tag{3.90}$$

Before reaping the benefits of this assumption, i.e. solving the differential equation (3.6), the quality of this approximation has to be tested. In the following, it will be shown that the substitution

$$g_{tot}(t) \approx \overline{g_{tot}(t)} = const. \tag{3.91}$$

is valid for the high conductance state regime, where a high synaptic frequency, triggering small post synaptic potentials, sustains a conductance level high above the leak conductance.

For this purpose, the *coefficient of variation* will be employed, which is the quotient of the standard deviation and the mean of a distribution

$$c_v = \frac{\sigma}{\mu} \tag{3.92}$$

This measure provides information on how densely the distributed data is clustered around the mean.

To simplify the evaluation of c_v, the neuron will be stimulated by a single synapse, resulting in the mean and variance (3.88), (3.89) of the conductance of the stimulated neuron.

The coefficient of variation is then

$$c_v = \frac{\sqrt{\frac{1}{2} \cdot w_{syn}^2 \cdot \nu_{syn} \cdot \tau_{syn}}}{w_{syn} \cdot \nu_{syn} \cdot \tau_{syn}} \tag{3.93}$$

$$= \frac{1}{\sqrt{2 \cdot \nu_{syn} \cdot \tau_{syn}}} \tag{3.94}$$

This result shows that the measure only depends on the inverse of the square root of the input rate, and not on the synaptic weights, as one might naively expect.

Figure (3.5) shows the behavior of c_v.

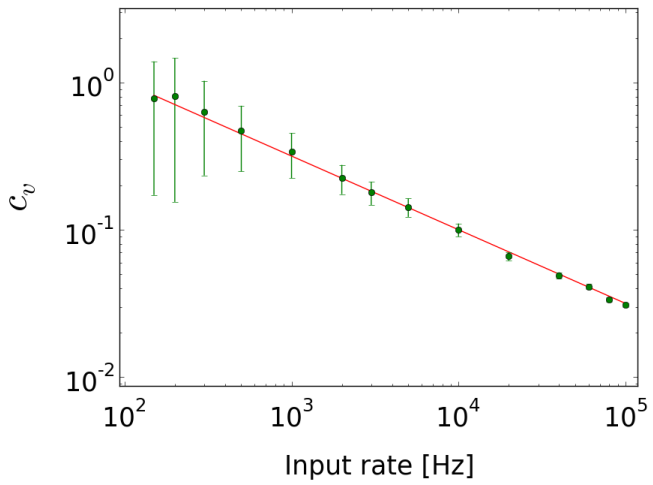

Figure 3.5: Illustration of the coefficient of variation of the synaptic conductance c_v with rising ν_{syn} on a double logarithmic scale. The red line denotes the theoretical equation (3.94), which has a gradient of $-\frac{1}{2}$ on a logarithmic scale. The green dots show the simulated results, with errorbars as the standard deviation. A decrease of the coefficient of variation signifies a more clustered set of data points in the proximity of the mean.

Therefore, one can assume the approximation (3.91) to be correct within an error margin of 10%, given a typical synaptic time constant of 5 ms, for total synaptic input rates

above 10 kHz[3], which represents a realistic regime for cortical neurons in vivo (see *Destexhe et al.* [2003]). This condition is further loosened by the membrane potential effectively constituting a low-pass filter for the conductance, thus further smoothing fast fluctuations.

3.1.5 High Conductance-based Approximation of the Leaky Integrate and Fire Model

Now that it is shown that $g_{syn}(t) + g_L \approx \overline{g_{tot}(t)} = g_{tot} = const.$, it follows

$$V_{eff}(t) = \frac{\sum_i g_{syn}(t) \cdot E_i}{\cancel{g_{tot}(t)}} \tag{3.95}$$

Again, the focal point of this section is equation

$$\tau_{eff} \cdot \frac{dV}{dt} = V_{eff}(t) - V(t) \tag{3.96}$$

Now, knowing more about $V_{eff}(t)$, two different effective potentials will be considered, $V_{eff}(t)$ being an unspecified effective potential and $V'_{eff}(t)$ the effective potential with exactly the same progression as $V_{eff}(t)$, except with an additional input spike that occured at time $t = 0$. This additional synaptic spike opens a conductance g_x towards the reversal potential E_x.

$$V_{eff}(t) = \frac{\sum_i g_{in}(t) \cdot E_i}{g_{tot}} \tag{3.97}$$

$$V'_{eff}(t) = \frac{\sum_i g_{in}(t) \cdot E_i + g_x(t) \cdot E_x}{g_{tot}} \tag{3.98}$$

$$\mathrm{i} \in \{L, syn\} \tag{3.99}$$

Of course, the two membrane potentials $V(t)$ and $V'(t)$ will be different due to the added input in the primed situation.

To be able to solve (3.96), the difference of the effecitve potentials $V'_{eff}(t) - V_{eff}(t)$ will be computed.

To be able to do this, an approximation will be aplied. Because the total conductance in the high conductance state is sustained by many occuring input spikes, the impact on the total conductance from one single spike $g_x(t)$ is negligible compared with the total conductance $g_{tot}(t)$.

Therefore, equation (3.98) will be approximated as the first two terms of its Taylor-Series. The general form of this equation is

[3] assuming approximately equal weight synapses

$$f(x) = \frac{a + b \cdot x}{c + x} \ . \tag{3.100}$$

The first two terms of the Taylor-Series of (3.100) at $x = 0$ is then

$$f(x \to 0) = \frac{a}{c} + \frac{b \cdot (c + x) - (a + bx)}{(c + x)^2}\bigg|_{x=0} \cdot x \qquad = \frac{a}{c} + \frac{bc - a}{c^2} \cdot x \tag{3.101}$$

Making the following substitutions,

$$x = g_x(t) \qquad a = \sum_i g_i \cdot E_i \tag{3.102}$$

$$b = E_x \qquad c = g_{tot} \ , \tag{3.103}$$

results in

$$V'_{eff} \approx \frac{\sum_i g_i(t) \cdot E_i}{g_{tot}} + \frac{g_{tot} \cdot E_x - \sum_i g_i \cdot E_i}{g_{tot}^2} \cdot g_x(t) \tag{3.104}$$

$$= \frac{\sum_i g_i(t) \cdot E_i}{g_{tot}} + \frac{g_{tot} \cdot E_x - V_{eff}(t) \cdot g_{tot}}{g_{tot}^2} \cdot g_x(t) \tag{3.105}$$

$$= \frac{\sum_i g_i(t) \cdot E_i}{g_{tot}} + \frac{E_x - V_{eff}(t)}{g_{tot}} \cdot g_x(t) \tag{3.106}$$

The difference of both effective potentials is then

$$\Delta V_{eff}(t) := V'_{eff}(t) - V_{eff}(t) = \frac{E_x - V_{eff}(t)}{g_{tot}} \cdot g_x(t) \tag{3.107}$$

The next step will be exactly the same as for the current-based LIF mode in section 3.1.1: Inserting $V'_{eff}(t)$ and $V_{eff}(t)$ in equation (3.96) and subtracting them, yields

$$\tau_{eff} \cdot \frac{dV'(t)}{dt} = V'_{eff}(t) - V'(t) \tag{3.108}$$

$$\tau_{eff} \cdot \frac{dV(t)}{dt} = V_{eff}(t) - V(t) \tag{3.109}$$

Subtracting eq. (3.109) from (3.108) and dividing by τ_{eff}, yields

$$\frac{d(V' - V)}{dt} = \frac{1}{\tau_{eff}} \cdot \Bigg(\underbrace{\frac{E_x - V_{eff}(t)}{g_{tot}} \cdot g_x(t)}_{=\Delta V_{eff}(t)} - \underbrace{V_{psp}(t)}_{:=V'(t)-V(t)} \Bigg) \tag{3.110}$$

The index x denotes the synaptic conductances, as well the synaptic reversal potentials, since every input will be synaptical. Therefore, it is possible to substitute at this point, without losing generality:

$$g_x \longrightarrow g_{syn} = w_{syn} \cdot e^{-\frac{t}{\tau_{syn}}} \tag{3.111}$$

$$E_x \longrightarrow E_{syn} \tag{3.112}$$

The only hindrance to solving differential equation (3.117) is the complex time dependence of $\Delta V_{eff}(t)$, which is a consequence of the time dependence in $V_{eff}(t)$. Therefore, the last approximation is to take the mean of $\Delta V_{eff}(t)$ instead, by computing $\overline{V_{eff}(t)}$.

$$\overline{\Delta V_{eff}(t)} = \sum_{syn} \frac{E_{syn} - \overline{V_{eff}}(t)}{g_{tot}} \cdot g_{syn} \cdot e^{-\frac{t}{\tau_{syn}}} \tag{3.113}$$

$$V_{eff}(t) = \sum_{i \in \{L,syn\}} \frac{g_i \cdot E_i}{g_{tot}} \quad \longrightarrow \quad \overline{V_{eff}(t)} = \sum_{i \in \{L,syn\}} \frac{\overline{g_i} \cdot E_i}{g_{tot}} \tag{3.114}$$

This approximation can be justified by the results from section (3.1.4), which allowed to state $g_{tot} \approx \overline{g_{tot}(t)}$. This can be applied to the effective potential, as its time course is determined by conductance changes from inputs.
The mean of the effective potential can be computed simply by the substitutiion

$$g_{syn}(t) \to \overline{g_{syn}} = \nu_{syn} \cdot w_{syn} \cdot \tau_{syn} \ . \tag{3.115}$$

The mean effective potential is then

$$\overline{V_{eff}} = \frac{\sum\limits_{syn} \nu_{syn} \cdot w_{syn} \cdot \tau_{syn} \cdot E_{syn} + g_L \cdot E_L}{g_{tot}} \ , \tag{3.116}$$

giving the final form of the differential equation to solve;

$$\frac{dV_{psp}(t)}{dt} = \frac{1}{\tau_{eff}} \cdot \left(\frac{E_{syn} - \overline{V_{eff}}}{g_{tot}} - V_{psp} \right) \tag{3.117}$$

This is done exactly like the derivation of the current-based PSPs in section (3.1.1), since both equations have the same structure, the only difference being the kernels and their time constants. Remembering the equations that lead to the solution of the current-based LIF model ((3.23) and (3.24)), one can simply modify them:

$$a(t) = -\frac{1}{\tau_{mem}} \quad \to \quad -\frac{1}{\tau_{eff}} \tag{3.118}$$

$$b(t) = \frac{i_{syn}}{g_L \cdot \tau_{mem}} \cdot e^{-\frac{t}{\tau_{syn}}} \quad \to \quad \frac{g_{syn} \cdot (E_{syn} - \overline{V_{eff}})}{g_{tot} \cdot \tau_{eff}} \cdot e^{-\frac{t}{\tau_{syn}}} \tag{3.119}$$

The rest of the computation applies to the current-based case, resulting in eq. (3.29). The result is then

PSP time course for a LIF neuron in the high conductance state

The synaptic PSP triggered by a conductance rise through synaptic weight w_{syn} with time constant τ_{syn} in the high conductance approximation of a LIF neuron with reversal potentials E_{syn}, a total conductance g_{tot} and membrane time constant τ_{eff}:

$$V_{psp}(t) = \frac{w_{syn} \cdot (E_{syn} - \overline{V_{eff}}) \cdot \tau_g}{g_{tot} \cdot \tau_{eff}} \cdot \left[e^{-\frac{t}{\tau_{eff}}} - e^{-\frac{t}{\tau_{syn}}} \right] \tag{3.120}$$

$$g_{tot} = \overline{g_{syn}} + g_L = \nu_{syn} \cdot w_{syn} \cdot \tau_{syn} + g_L$$

$$\tau_{eff} = \frac{C_{mem}}{g_{tot}} \qquad \tau_g = \left[\frac{1}{\tau_{syn}} - \frac{1}{\tau_{eff}} \right]^{-1} \qquad \overline{V_{eff}} = \frac{\sum_i \overline{g_i} \cdot E_i}{g_{tot}}$$
$$\text{with } i \in \{L, syn\}$$

Several important points need to be stressed:

- The starting point was the differential equation of the LIF model, (3.6). It has been shown that one can approximate the total conductance as its mean value $g_{tot} \approx \overline{g_{tot}}$, see section (3.1.4). With this first important approximation, it is possible to solve equation (3.6) analytically, because the time dependency in τ_{eff} has been eliminated.
- The membrane potential was assumed to be found close to the mean of the effective potential $\overline{V_{eff}}$ at all times, so every PSP rises with a factor proportional to the constant difference $w_{syn} \cdot |E_{syn} - E[V_{eff}]|$. This means that all evoked PSPs have an identical shape, given by $\exp(-\frac{t}{\tau_{eff}}) - \exp(-\frac{t}{\tau_{syn}})$, with the differences in magnitude resulting only from the individual synaptic weights and reversal potentials.

This approximation in the high conductance state has potential shortcomings:

The quality of this model obviously depends on the input parameters w_{inh}, w_{exc}, ν_{inh}, ν_{exc}. If the membrane potential lies too far away from the dynamic equilibrium $\overline{V_{eff}}$, the term $E_x = E_{rev} - \overline{V_{eff}}$ can deviate significantly from the actual scaling of the simulation.

A fast plausibility test of this approximation can be achieved by reducing the effective time constant τ_{eff}. At the beginning of this chapter, it was explained that the membrane

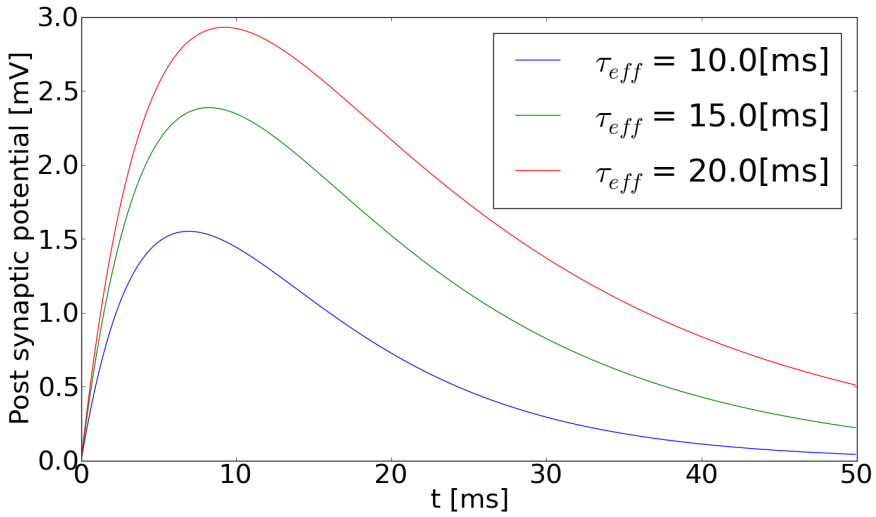

(a) Time course of PSP

Figure 3.6: Post synaptic potential of excitatory input for different time constants

potential of a conductance-based LIF model reacts to synaptic input as a low-pass-filter with a specific time constant τ_{eff}. The effective potential $V_{eff}(t)$ (which represents a purely mathematical construct and has no directly measurable physical equivalent in the cell) reacts to synaptic input immediately. The PSP time course derived above should exhibit the same behavior, if τ_{eff} converges to zero. In this approach, the PSP time course should rise abruptly instead of showing an alpha-shaped rise, as depicted in fig. 3.6. This can be tested on the derived PSP time course 3.120 by making it independent of τ:

$$V_{psp}(t) = \frac{w_{syn} \cdot (E_{syn} - \overline{V_{eff}}) \cdot \tau_{syn}}{g_{tot} \cdot (\tau_{eff} - \tau_{syn})} \cdot \left[e^{-\frac{t}{\tau_{eff}}} - e^{-\frac{t}{\tau_{syn}}} \right] \tag{3.121}$$

Applying

$$\tau_{eff} \to 0 \tag{3.122}$$

to equation (3.120) results in

$$V'_{psp}(t) = \frac{w_x \cdot (E_{syn} - \overline{V_{eff}}) \cdot \tau_{syn}}{g_{tot} \cdot \tau_{syn}} \cdot e^{-\frac{t}{\tau_{syn}}} \tag{3.123}$$

This equals precisely $\Delta V_{eff}(t)$, which comes to prove the plausibility of the results derived above.

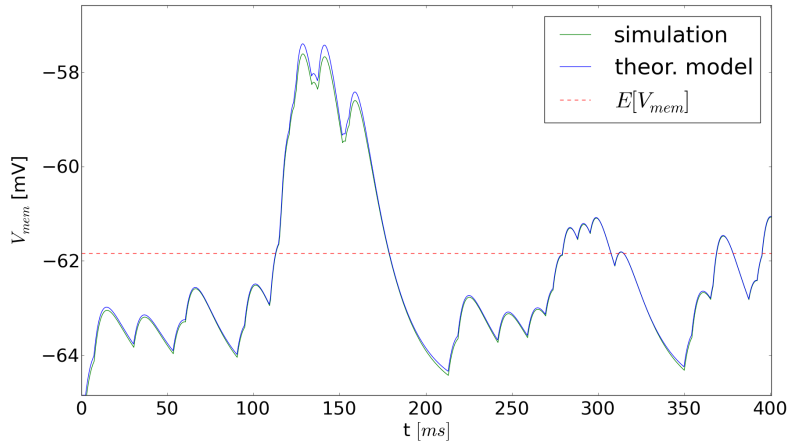

(a) Low conductance state with ν_{exc}

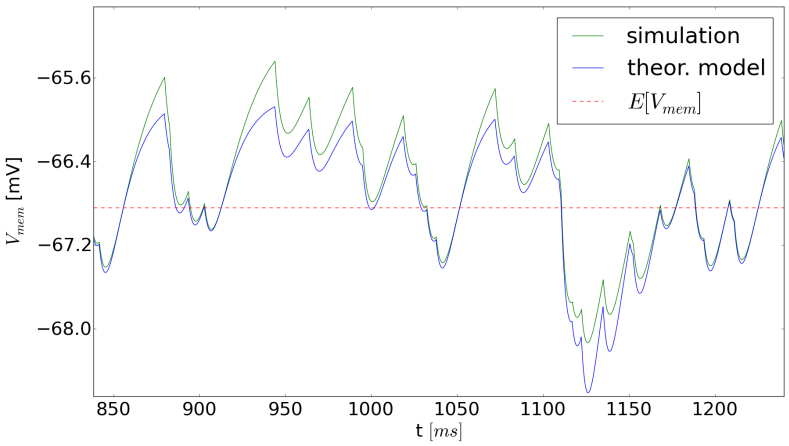

(b) Low conductance state with ν_{inh}

Figure 3.7: Two membrane potentials and their means (red dashed lines) with $\nu_{syn} = 100$ Hz for both simulations. Figure (3.7a) shows an excitatory stimulation with good agreement between the simulated and theoretical trace (as in eq. (3.120)). The term of the theoretical trace $PSP_{exc} \sim |E_{exc} - \overline{V_{eff}}| \approx 59$ mV scales slightly too high for regions far above the mean. The same, yet more dominant effect occurs for purely inhibitory input in fig. (3.7b). The deviations are higher in this case, because the theoretical trace gets close to the inhibitory reversal potential E_{inh} at -70 mV. Therefore, the differences of the simulated PSPs to the theoretical ones are higher than in the situation with only excitatory inputs, where $E_{exc} = 0$ mV.

By increasing the input rates and lowering the synaptic weights, better general agree-

ment between the theoretical and simulated traces can be achieved than for the states that have been shown in fig. (3.7), as the simulated and the theoretical traces are closer to the mean (fig. 3.8).

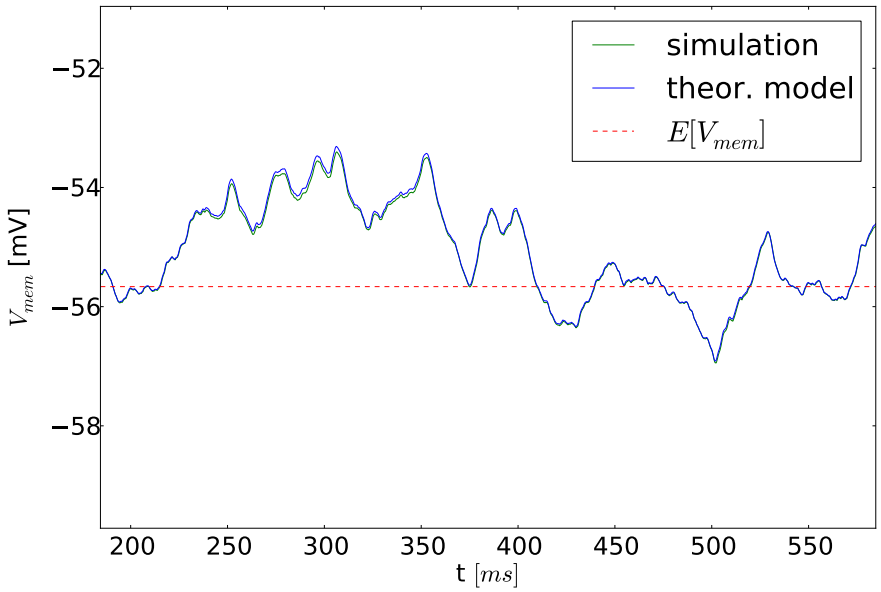

(a) High conductance state of a depolarized neuron

Figure 3.8: An example of the high conductance state with high synaptic rates of $\nu_{inh} = \nu_{exc} = 4500$ Hz, and low weights $w_{exc} = 5 \cdot 10^{-4}$ μS, $w_{inh} = 5 \cdot 10^{-4}$ μS. The traces show nearly perfect agreement, even better than the depolarized neuron in fig. (3.7a). Note that this neuron is also depolarized, but is more clustered around its mean (red dashed line), therefore not deviating much from the stereotypical PSPs proportional to $(E_{syn} - \overline{V_{eff}})$

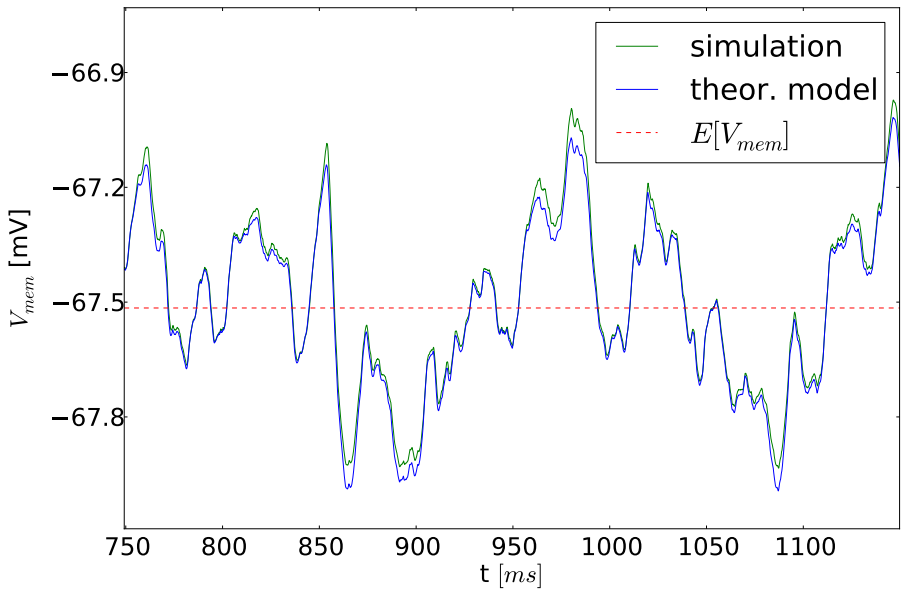

(a) High conductance state of a hyperpolarized neuron

Figure 3.9: A hyperpolarized high conductance state with synaptic inputs of $\nu_{inh} = \nu_{exc} = 4500$ Hz and low synaptic weights $w_{exc} = 1 \cdot 10^{-4}\mu$S, $w_{inh} = 30 \cdot 10^{-4}\mu$S. The mean value close to both the resting and reversal potential at -67.5 mV. As the membrane potential drops closer towards E_{inh}, the quality of the approximation decreases visibly, but not as drastically as the state driven by comparably high synaptic weights and low input rates depicted in fig. 3.7b. Again, just like in the depolorazied high conductance state in fig. 3.8, the membrane potential is more clustered around the mean (red dashed line), hence approximated well by PSPs proportional to $(E_{syn} - \overline{V_{eff}})$.

The following conclusions can be obtained from this illustration of the conductance-based approximation:
The membrane potential value itself is not the decisive factor for the quality of the approximation through stereotypical PSPs, but rather its distance to the reversal potentials E_{syn}. The excitatory PSPs are generally approximated better, because $E_{exc} = 0$ mV is far away from all subthreshold regions of the membrane potential. In contrast, the inhibitory reversal potential $E_{inh} = -70$ mV is much closer to all subthreshold regions of the membrane potential, which can cause problems when inhibition becomes too strong. A high standard deviation of the membrane potential can therefore produce a less precise approximation of the PSPs (and thus, membrane potential), because the PSPs $\sim (E_{inh} - \overline{V_{eff}})$ can underlie heavier deviations than their excitatory counterparts $(E_{exc} - \overline{V_{eff}})$.

For an analysis of correlated neuron dynamics, which is the subject of chapters 3 and 4, an accurate description of membrane potential statistics is necessary.

To this end, the mean and variance of the theoretical (current- and conductance-based) approximations to the LIF neuron will be derived in the following section.

3.1.6 Membrane Potential Statistics

Deriving closed-form expressions for the mean and variance of the membrane potential of a LIF neuron can be done mostly without specifying the approximation of the referred LIF model (i.e. current-based or cond.-based in a high conductance state), as the PSP time courses are similar:

$$V_{psp} = S \cdot \left(e^{-\frac{t}{\tau_i}} - e^{-\frac{t}{\tau_{syn}}} \right) \tag{3.124}$$

Both PSP kernels have the same structure, consisting of a scaling multiplicator S_{syn} and two exponentials determining their shape

$$V_{psp}(t) = S_{syn} \cdot \left(e^{-\frac{t}{\tau}} - e^{-\frac{t}{\tau_{syn}}} \right) \tag{3.125}$$

cond:

$$\tau = \tau_{eff}$$
$$\tau_g = \left[\frac{1}{\tau_{syn}} - \frac{1}{\tau_{eff}} \right]^{-1}$$
$$S_{syn} = \frac{w_{syn} \cdot (E_{syn} - \overline{V_{eff}}) \cdot \tau_g}{g_{tot} \cdot \tau_{eff}}$$

curr:

$$\tau = \tau_{mem}$$
$$\tau_c = \left[\frac{1}{\tau_{syn}} - \frac{1}{\tau_{mem}} \right]^{-1}$$
$$S_{syn} = \frac{i_{syn} \cdot \tau_c}{g_L \cdot \tau_{mem}} \tag{3.126}$$

Mean and variance for the current-based model:

For the current-based model, the computation of the mean and variance of the membrane potential can be done in a straightforward way, utilizing the results from section 3.1.3 with the following parameters:

$\rightarrow$ synaptic input rates ν_{syn}, (3.127)

$\rightarrow$ S_{syn}, taken from the general definition in (3.125), gives kernel (3.128)

$$\kappa(t) = S_{syn} \cdot \left(e^{-\frac{t}{\tau_{mem}}} - e^{-\frac{t}{\tau_{syn}}} \right) \tag{3.129}$$

Substituting these into equation (3.77) yields the integral for the mean of the PSPs:

$$E[V_{psp}^{syn}] = \nu_{syn} \cdot S_{syn} \cdot \int_0^{T_{sim}} \left(e^{-\frac{t}{\tau_{mem}}} - e^{-\frac{t}{\tau_{syn}}} \right) dt \tag{3.130}$$

This integral is easy to compute, resulting in:

$$E[V_{psp}^{syn}] = \nu_{syn} \cdot S_{syn} \cdot (\tau_{mem} - \tau_{syn}) \tag{3.131}$$
$$= \frac{\nu_{syn} \cdot i_{syn} \cdot \tau_{syn}}{g_L} \tag{3.132}$$

This result applies to a single synapse firing with rate ν_{syn}. To compute the total synaptic mean, the crucial property of spatial summation can be used, which was described in more detail on p. 13. This means that the total mean of the membrane potential can be expressed as the sum of the contributions from each synapse $E[V_{psp}^{syn}]$:

$$E\left[\sum_{syn} V_{psp}^{syn}\right] = \sum_{syn} E[V_{psp}^{syn}] \tag{3.133}$$

Additionally, the result is shifted by the leak term $\frac{I_L}{g_L}$ (see eq. (3.9)), resulting in

$$E[V_{mem}] = \sum_{syn} \frac{\nu_{syn} \cdot i_{syn} \cdot \tau_{syn}}{g_L} + \frac{I_L}{g_L} \tag{3.134}$$

$$= \frac{\sum_i \overline{I_i}}{g_L} \qquad \text{with } i \in \{L, syn\} \tag{3.135}$$

$$= \overline{V_{eff}}\ . \tag{3.136}$$

Naturally, the average of the membrane potential is the average of the dynamic equilibrium of the stimulated neuron, V_{eff}.

The variance of the membrane potential can be derived in the same fashion, substituting parameters (3.127) and (3.129) into (3.78), to yield the integral

$$Var[V_{psp}^{syn}] = \nu_{syn} \cdot \int_0^{T_{sim}} S_{syn}^2 \cdot \left(e^{-\frac{t}{\tau_{mem}}} - e^{-\frac{t}{\tau_{syn}}}\right)^2 dt \tag{3.137}$$

$$= \nu_{syn} \cdot S_{syn}^2 \cdot \int_0^{T_{sim}} \left[e^{-\frac{2 \cdot t}{\tau_{syn}}} + e^{-\frac{2 \cdot t}{\tau_{mem}}} - 2 \cdot e^{-t \cdot \left(\frac{1}{\tau_{syn}} + \frac{1}{\tau_{mem}}\right)}\right] dt \tag{3.138}$$

The evaluation of this integral gives

$$Var[V_{psp}^{syn}] = \nu_{syn} \cdot S_{syn}^2 \cdot \left[\frac{\tau_{mem}}{2} + \frac{\tau_{syn}}{2} - 2 \cdot \frac{\tau_{mem} \cdot \tau_{syn}}{\tau_{mem} + \tau_{syn}}\right]. \tag{3.139}$$

This result applies to each synapse.

With the same reasoning that has been applied before when evaluating the mean, the spatial summation allows to express the total variance of all PSPs as the sum of variances of each single PSP:

$$Var[V_{psp}] = Var\left[\sum_{syn} V_{psp}^{syn}\right] = \sum_{syn} Var[V_{psp}^{syn}] \tag{3.140}$$

$$Var[V_{psp}] = \sum_{syn} \nu_{syn} \cdot S_{syn}^2 \cdot \left[\frac{\tau_{syn}}{2} + \frac{\tau_{mem}}{2} - 2 \cdot \frac{\tau_{mem} \cdot \tau_{syn}}{\tau_{mem} + \tau_{syn}} \right] \tag{3.141}$$

$$= \sum_{syn} \nu_{syn} \cdot \left(\frac{i_{syn} \cdot \tau_c}{\tau_{mem} \cdot g_L} \right)^2 \cdot \left[\frac{\tau_{syn}}{2} + \frac{\tau_{mem}}{2} - 2 \cdot \frac{\tau_{mem} \cdot \tau_{syn}}{\tau_{mem} + \tau_{syn}} \right] \tag{3.142}$$

This is the variance of the PSPs for all synapses, which is obviously equivalent to the total variance of the membrane potential.

Mean and variance for the high conductance state approximation:

Because of the differences between the current-based and conductance-based LIF neuron, the approach to compute mean for the latter is less straightforward than the previous derivations for the current-based model.

First of all, the derivation of the PSP time course was only possible because the neuron was considered to be in a constantly stimulated state at the times of all spike occurences. This means that the neuron is kept in this state by frequent synaptic input, and every incoming PSP contributes to maintain it.

The average of this state is the effective potential $\overline{V_{eff}}$ (already derived in (3.116)), and also the mean of the membrane potential itself (as derived for the current-based model in (3.136)):

$$E[V_{mem}] \overset{(3.116)}{=} \overline{V_{eff}} = \frac{\sum\limits_{i \in \{L,syn\}} \overline{g_i} \cdot E_i}{g_{tot}} \tag{3.143}$$

To compute the variance of the membrane potential, one needs to compute the variance of all evoked PSPs, which has been done for the current-based approximation already. The only difference is the different scaling S_{syn} and membrane time constant, as can be seen on p. 42.

The integral to compute the variance of occuring PSPs generated with an input rate ν_{syn} from one synapse is then basically the same as in eq. (3.137), but with the substitution $\tau_{mem} \to \tau_{eff}$. The end result of the variance for the variance of the membrane potential of the high conductance approximation of the LIF neuron is

$$Var[V_{mem}] = \sum_{syn \in \{exc,inh\}} \nu_{syn} \cdot \left(\frac{w_{syn} \cdot (E_{syn} - V_{eff} \cdot \tau_g}{\tau_{eff} \cdot g_{tot}} \right)^2 \cdot \left[\frac{\tau_{syn}}{2} + \frac{\tau_{eff}}{2} - 2 \cdot \frac{\tau_{eff} \cdot \tau_{syn}}{\tau_{eff} + \tau_{syn}} \right] \tag{3.144}$$

The results and conclusions of this subsection should be briefly summarized at this point:

Expectation values and variances of the membrane potential of high conductance- and current-based LIF model with the leak conductance g_L at the resting potential E_L, stimulated by synaptic input with input rates ν_{inh}, ν_{exc} with synaptic strengths (cond:) w_{syn} or (current:) i_{syn}:

Mean:

$$E[V_{mem}] = \overline{V_{eff}} \tag{3.145}$$

cond.:

$$\overline{V_{eff}} = \sum_{syn} \frac{E_{syn} \cdot \overline{g_{syn}}}{g_{tot}} + E_L \qquad \overline{g_{syn}} = \nu_{syn} \cdot w_{syn} \cdot \tau_{syn}$$

curr.:

$$\overline{V_{eff}} = \sum_{syn} \frac{\overline{I_{syn}}}{g_L} + E_L \qquad \overline{i_{syn}} = \nu_{syn} \cdot i_{syn} \cdot \tau_{syn} \tag{3.146}$$

Variance:

$$Var[V_{mem}] = \sum_{syn \in \{exc,inh\}} \nu_{syn} \cdot S_{syn}^2 \cdot \left[\frac{\tau_{syn}}{2} + \frac{\tau}{2} - 2 \cdot \frac{\tau \cdot \tau_{syn}}{\tau + \tau_{syn}} \right] \tag{3.147}$$

cond:

$$\tau = \tau_{eff}$$
$$\tau_g = \left[\frac{1}{\tau_{syn}} - \frac{1}{\tau_{eff}} \right]^{-1}$$
$$S_{syn} = \frac{w_{syn} \cdot (E_{syn} - \overline{V_{eff}}) \cdot \tau_g}{\tau_{eff} \cdot g_{tot}}$$

curr:

$$\tau = \tau_{mem}$$
$$\tau_c = \left[\frac{1}{\tau_{syn}} - \frac{1}{\tau_{mem}} \right]^{-1}$$
$$S_{syn} = \frac{i_{syn} \cdot \tau_c}{\tau_{mem} \cdot g_L}$$

3.1.7 Systematic Deviations from the theoretical Approximation

It has been noted before that there are regions where the high conductance approximation shows notable deviations from the actual membrane potential.

On the other hand, the results derived for the current-based model are expected to be precise for all synaptic input regimes.

To have an overview of the quality of both approximations for different configurations, a sweep was performed over the four input parameters within such limits that output spiking was not induced, as it would skew the membrane potential statistics.

To ensure a sufficient number of samples, for a broad parameter range, the input rates were chosen very high. Accordingly, to avoid output spiking, synaptic weights were adjusted to a low range.

Due to the large difference in equally weighted synaptic input from excitatory and inhibitory synapses,

- $E_{exc} - E_{rest} = 65$ mV,
- $E_{inh} - E_{rest} = -5$ mV,

A factor of 13 results as a difference in scaling of the PSPs. To achieve balanced stimulation, the inhibitory synaptic weights were chosen to be 13× higher than the excitatory weights.
For the current-based case, the contribution due to the synaptic weights is equal for equal synaptic currents. The current parameters were chosen equal for both synapses.

Parameter spaces

High-conductance-based parameters:

$$\begin{aligned} w_{exc} &\in [5 \cdot 10^{-4}\mu\text{S},\, 5 \cdot 10^{-3}\mu\text{S}\ ] \\ w_{inh} &\in [65 \cdot 10^{-4}\mu\text{S},\, 65 \cdot 10^{-3}\mu\text{S}\ ] \\ \nu_{exc}, \nu_{inh} &\in [200\text{ Hz},\, 2900\text{ Hz}] \end{aligned}$$

Current-based model parameters:

$$\begin{aligned} i_{exc}, i_{inh} &\in [5 \cdot 10^{-3}\text{ nA},\, 5 \cdot 10^{-2}\text{ nA}] \\ \nu_{exc}, \nu_{inh} &\in [200\text{ Hz},\, 2900\text{ Hz}] \end{aligned}$$

At first, one can validate the influence of the input parameters on the statistical values that have been derived for the mean and variance in (3.146) and (3.147), respectively.

The mean value receives equal linear contribution from synaptic rates and weights, whereas the variances exhibit a quadratic dependence on synaptic weights and are influenced linearly by synaptic rates:

$$E[V_{mem}] \sim w_{syn} \cdot \nu_{syn} \tag{3.148}$$

$$Var[V_{mem}] \sim w_{syn}^2 \cdot \nu_{syn} \tag{3.149}$$

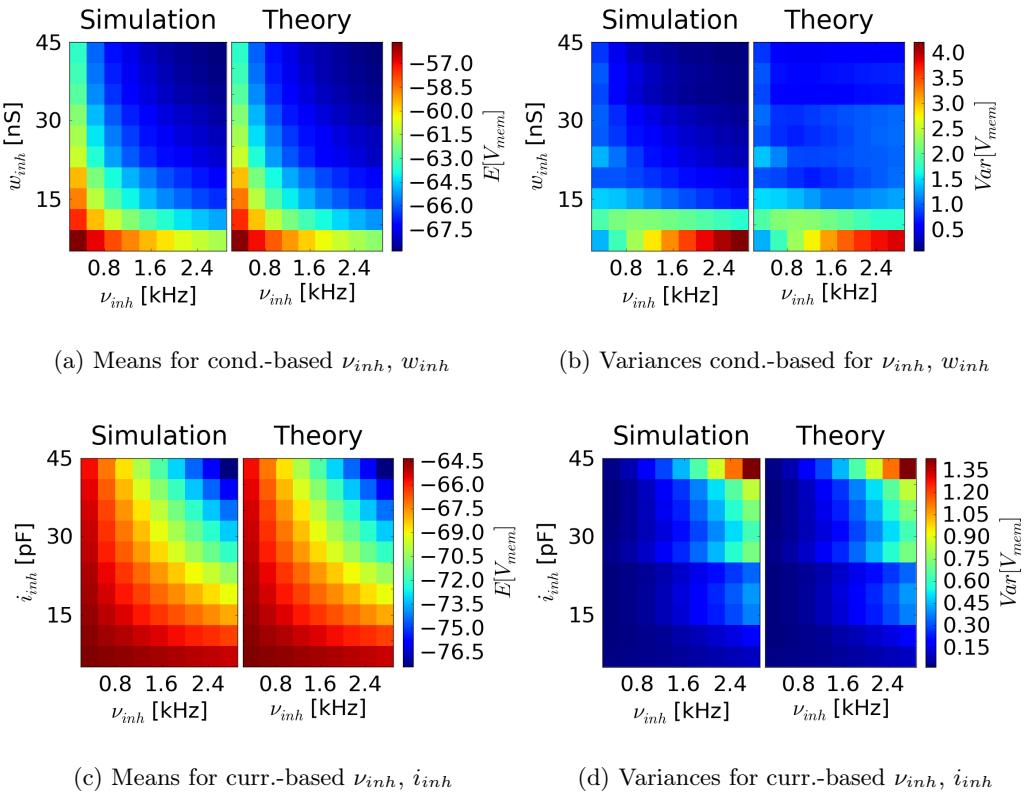

(a) Means for cond.-based ν_{inh}, w_{inh}

(b) Variances cond.-based for ν_{inh}, w_{inh}

(c) Means for curr.-based ν_{inh}, i_{inh}

(d) Variances for curr.-based ν_{inh}, i_{inh}

Figure 3.10: Color plots of statistical values with varying inhibitory input paramters and constant excitatory inputs, validating eq. (3.148) and (3.149).
Fig. (3.10a) and (3.10c) show an equal impact of synaptic rate and weight on the mean, which decreases symmetrically due to $\sim w_{inh} \cdot \nu_{inh}$, as predicted in (3.148). Figure (3.10b) shows the variances in the conductance-based model. The variance depends quadratically on w_{inh}, and linearly on ν_{inh}, as predicted in (3.149). For even higher inhibitory input, variance decreases as the mean comes closer to E_{inh}. There are no such saturation effects for the current-based model (3.10d), due to lack of reversal potentials. The asymmetry in influence of the variance also applies for the current-based model in with $Var[V_{mem}] \sim \nu_{inh} \cdot i_{inh}^2$.

Figures in (3.10) show this behaviour for both the simulated and theoretical statistical values for the current-based- as well as the conductance-based model for the inhibitory case. This strongly supports the analytical results that have been obtained in the past section, which exhibit the same dependencies on the synaptic inputs as the simulated membrane potentials.

Throughout all input ranges, the mean of the simulated LIF neuron is very precisely approximated by the theoretical mean. This can be seen in the color plots in fig. 3.11, where an equal increase of ν_{exc} and ν_{inh} yields perfect agreement in all hyperpolarized, as well as depolarized neurons.

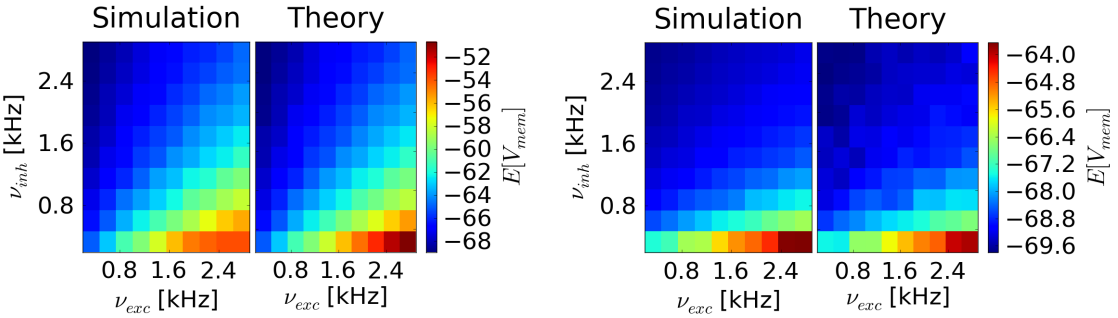

Figure 3.11: Illustration of means of theoretical and simulated traces. In fig. (3.11a), the synaptic weights were chosen to give equal contributions, with $w_{exc} = 15 \cdot 10^{-4}\mu$S, and $w_{inh} = \frac{E_{exc}}{E_{inh}} \cdot w_{exc} = 13 \cdot w_{exc} = 195 \cdot 10^{-4}\mu$S. For all parameter regions, the theoretical values approximate the real mean values very well.
Figure (3.11b) shows such a comparison for a relatively large inhibitory weight. With $w_{exc} = 5 \cdot 10^{-4}\mu$S, $w_{inh} = 65 \cdot 10^{-3}\mu$S $> 13 \cdot w_{exc}$, the means are very close to the resting- and inhibitory potential. Nevertheless, the theoretical mean values again show very good agreement in parameter regions where the neuron is hyperpolarized.

As opposed to this, the theoretical variances of the high conductance approximation, are expected to show systematic errors. This is a consequence of the problematic factor $E_{syn} - \overline{V_{eff}}$, which is included in the scaling of the conductance-based theoretical PSPs, and also in the variance. Any deviation from the average effective potential causes a difference to the simulated PSP.

The reason for this was discussed in more detail at the end of section 3.1.5. Resulting deviations between the theoretical and simulated traces arise when the membrane potential is located at the proximity of the inhibitory reversal potential E_{inh}, shown in figures 3.7b and 3.9.

This means that the systematic error of the variance in the conductance-based model is expected to become larger for dominant inhibitory input. To show this, inhibitory rate and weight were increased gradually in figures 3.12 and 3.13, respectively. The color plot shows the resulting relative error

$$Err = \left| \frac{\sigma^2_{sim} - \sigma^2_{th}}{\sigma^2_{sim}} \right| . \tag{3.150}$$

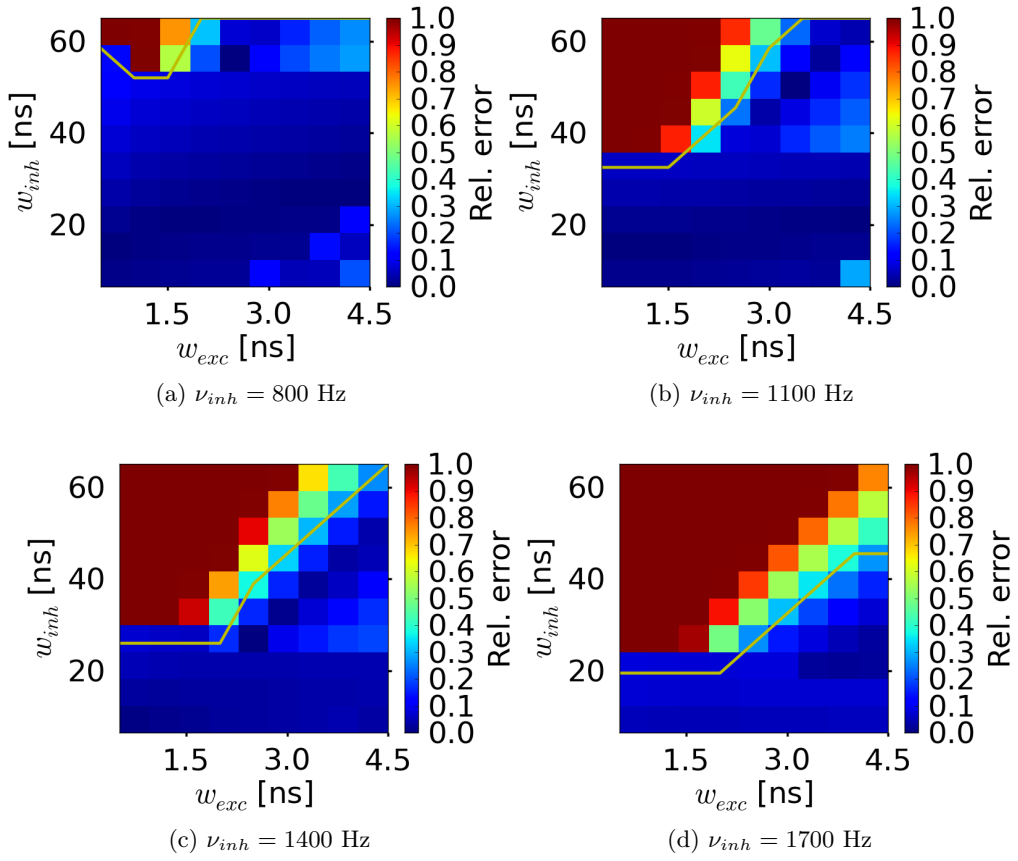

(a) $\nu_{inh} = 800$ Hz

(b) $\nu_{inh} = 1100$ Hz

(c) $\nu_{inh} = 1400$ Hz

(d) $\nu_{inh} = 1700$ Hz

Figure 3.12: These four colorplots show the relative errors (eq. 3.150) between the theoretical variances and the ones from the simulated membrane potential, in dependence on w_{inh} and w_{exc}. For each figure, the yellow curves enclose the area with $Err > 0.4$. In each plot, it can be seen that regions of high relative errors can be found for low w_{exc} and high w_{inh}. Additionally, the inhibitory synaptic rate is increased gradually from 3.12a to 3.12d. This results in a growth of areas of high relative error (brown colored area) for high w_{inh}.

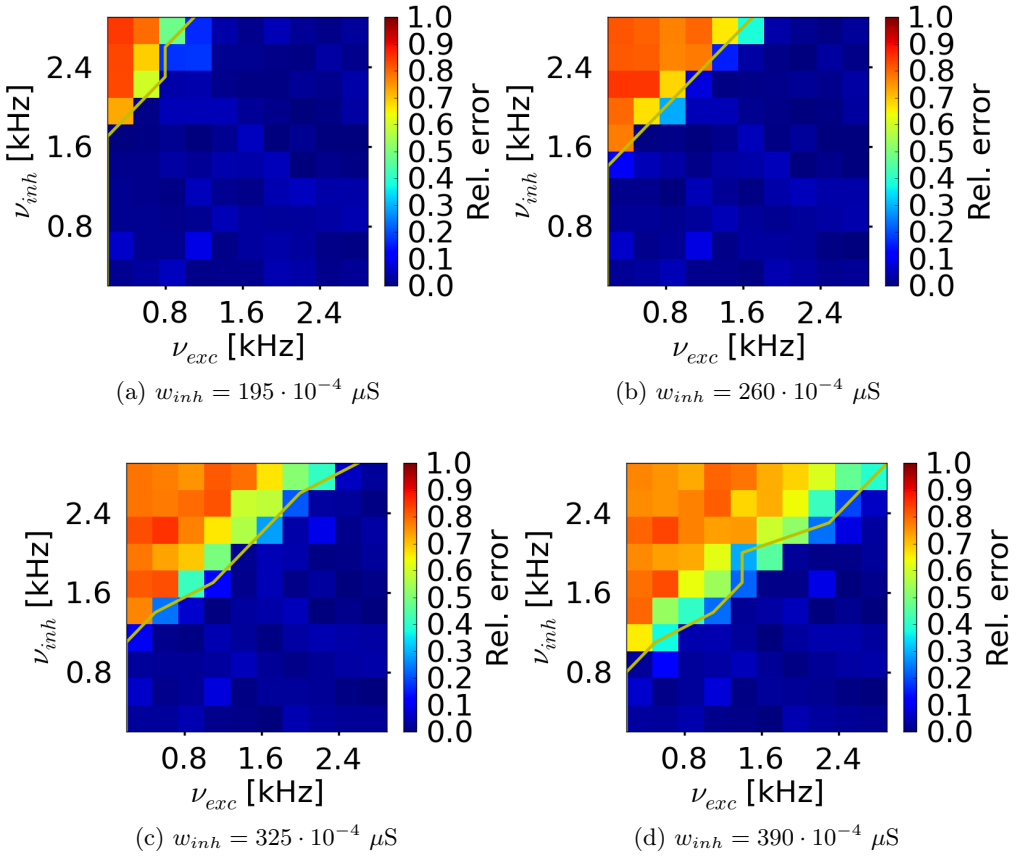

(a) $w_{inh} = 195 \cdot 10^{-4}$ μS

(b) $w_{inh} = 260 \cdot 10^{-4}$ μS

(c) $w_{inh} = 325 \cdot 10^{-4}$ μS

(d) $w_{inh} = 390 \cdot 10^{-4}$ μS

Figure 3.13: All colorplots show the relative errors (eq. 3.150) between the theoretical variances and the ones from the simulated membrane potential, analoguously to fig. 3.12. Here, the axes show the synaptic rates ν_{inh} and ν_{exc}. Again, the relative errors increase for high inhibition, for all four plots. The yellow curves enclose the area with $Err > 0.4$. From 3.13a to 3.13d, the inhibition is further increased by growing w_{inh}. As a result, the area of high errors grows for higher inhibitory weights from 3.13a to 3.13d.

Results for the conductance-based approximation:

- In general, the approximation for the conductance-based membrane potential yields a good estimation of mean values for all input parameter ranges, as can be seen in (3.11).
- The theoretical variances are more difficult to predict with the membrane potential composed of stereotypical PSPs. As inhibitory input is increased (via ν_{inh} or w_{inh}), the variances show deviations, as shown in figures 3.12 and 3.13.

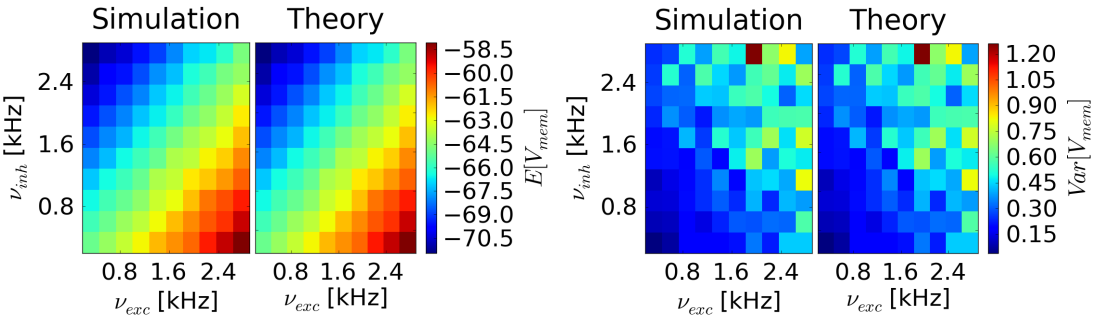

(a) Means of current-based simulation

(b) Variances of current-based simulation

Figure 3.14: Both figures show current-based statistical results with equal synaptic currents $i_{exc} = i_{inh} = 25 \cdot 10^{-3}$ nA, exhibiting perfect agreement between the theoretical mean values (3.14a) and variances (3.14b).

For parameter regions which result in depolarized neurons, the variances show good results. With the increase of inhibitory input, the membrane potential is driven towards E_{inh} with every inhibitory spike occurence.

Because of this proximity, the real scaling of the PSPs, $E_{inh} - V_{eff}(t)$ differs from the approximated scaling in the theoretical derivation $E_{inh} - \overline{V_{eff}}$.

Results for the current-based model:

- In the theoretical derivation of the current-based PSPs was no approxion used. The derivation is exact, and therefore the derived results yield ideal agreement (as seen in fig. 3.14) with the ones from simulation.

3.2 Distribution of the Membrane Potential

The modeling and prediction of the membrane potential has been successful so far for parameter regions that do not put it close to the inhibitory reversal potential and do not cause action potentials for high synaptic weights.

As the last step before finally committing to define and predict correlated behavior of neurons, it is essential to accurately describe the shape of the membrane potential distribution.

In this section, it will be shown that under certain circumstances, the membrane potential follows a Gaussian distribution. This will have crucial implications for the predictability of correlation measures as it will be possible to make use of several elegant properties of

this particular class of distributions.

In the derivation of the PSP time courses in section 3.1.5, a general PSP kernel was defined (eq. 3.125), covering both the HC-state and current-based LIF neuron models. In both cases, the superposition of PSP kernels is assumed to be linear, due to the fundamental principle of temporal and spatial summation of synaptic inputs, which was initially discussed on page 13 in the introductory chapter, and the approximations allowed by the considered input parameter ranges, discussed in section 3.1.7.

In this context, there is no difference between the current-based and conductance-based approximation, as both membrane potentials are sums of exponential kernels. This section will focus on the implications of the summation of kernels for the shape of the distribution of the membrane potentials.

3.2.1 Central Limit Theorem in the Current-based Model

Up to this point there was no information provided about the kind of distribution of the membrane potential amplitudes, simply because it was not necessary, even after deriving the variance and mean value of the potential. Certain factors determine the statistic nature of the membrane potential of a LIF model.

Mathematically, the generation of the PSPs is triggered by *point processes*. These are points of interest in the time space - i.e. input spike times (*Dayan and Abbott* [2001]). The PSPs are then generated by a kernel which is the PSP time course $V_{psp}(t)$ (as derived in (3.1.5)). The time constants of this kernel are the two time constants τ and synaptic time constant τ_{syn}.

If the input spike times follow poisson statistics (as proposed at the beginning of this chapter), it also applies to the PSPs. The filter process is then called a *shot noise*.

Moreover, if condition

$$\nu >> \frac{1}{\tau_{syn}} \tag{3.151}$$

holds, then the resulting membrane potential amplitude distribution can be approximated as a normal distribution due to the Central Limit Theorem (*Papoulis* [2002]).

The Central Limit Theorem states that the sum of independent random variables, converges towards a normal distribution with the increase of the sample size.

The classical *Central Limit Theorem* states:

Consider an N-sized random sample $\{X_1, \ldots, X_N\}$ of identically distributed, independent random variables, each with the mean μ and variance σ^2.
For large N, the sample mean of their sum, $S_N = \frac{X_1+\cdots+X_N}{N}$, is then a normal distribution $\mathcal{N}(\mu, \sigma^2)$ with the mean μ and the variance $\frac{1}{N} \cdot \sigma^2$.

In this case, a single random variable is the impact of an individual $PSP(t)$ on the membrane potential at time T.

$$PSP(t = T) = S_{syn}(t_{spk}) \cdot \left(e^{-\frac{(T-t_{spk})}{\tau}} - e^{-\frac{(T-t_{spk})}{\tau_{syn}}} \right) \tag{3.152}$$

with $\tau = \tau_{mem}$, τ_{eff} for current- or conductance-based model respectively. Dependent on where the PSP was triggered $t_{spk} \in [0, T]$, this impact will vary heavily. For many of these PSPs, with the sample size being approximately $N = T_{sim} \cdot \nu$ for very high simulation times T, the sum of all these impacts will converge to a normal distribution $\mathcal{N}(\mu, \sigma^2)$ for $t \to \infty$.

The implications for the conductance-based model will be addressed in the next section. If the total input rate is too small, then condition (3.151) is not fulfilled, because a fast relaxation of the membrane potental to the resting potential results in a surplus of probability in the regions closer to the resting potential. The membrane potential distribution becomes asymmetrical (see fig. 3.15).

The skewness of a membrane potential distribution $\rho(V_{mem})$ is a quantity which can be measured as the third statistic moment,

$$\rho_{V_{mem}} = E\left(\left| \frac{V_{mem} - E(V_{mem})}{Var(V_{mem})} \right|^3 \right) \ . \tag{3.153}$$

An upper boundary for the impact of the skewness of a distribution of a random variable on the convergence of the sum of such variables towards a Gaussian is provided by the *Berry-Esseen Theorem* (*Esseen* [1942])).

Unfortunately, the Berry-Esseen Theorem allows no particular assumptions for the shape of the individual distributions of the cumulated random variables and therefore provides upper bounds which are much larger than the trace errors resulting from low synaptic firing rates.

With no satisfactory theoretical tool available, estimates for the approximation quality have been obtained through numerical simulations. As a measure for the derivation of the

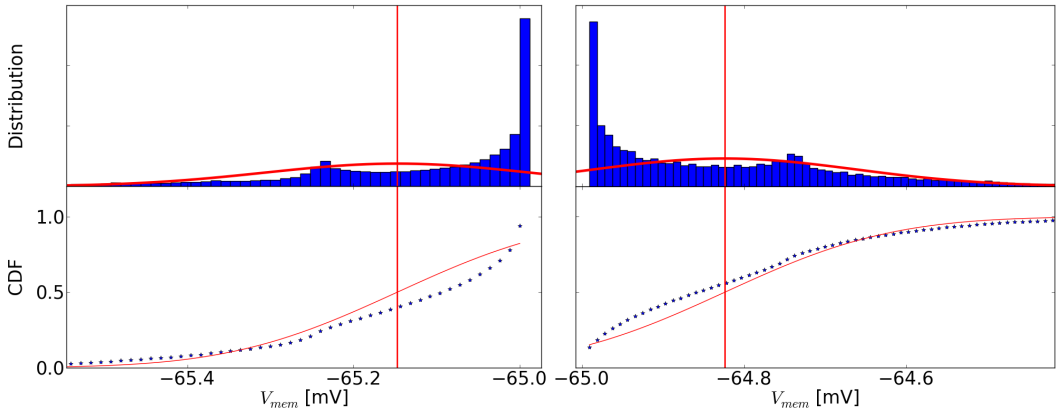

(a) V_{mem} for $\nu_{inh} = 20$ Hz (b) V_{mem} for $\nu_{exc} = 20$ Hz

Figure 3.15: The Current-based LIF neurons were stimulated by low input rates, and $i_{syn} = 0.08$ nA current weight and do not resemble normal distributions (red curves), but have the same mean values. In fig. (3.15a) and (3.15b), the distribtions are skewed to the region of lower potentials because the neuron is more often in a relaxating state than in an excited state immediately after a PSP generation. The small peaks in the center of the distribution show the maximum PSP height. The figures below the histograms show the cumulative density functions of the distributions (dotted lines), and the ones from theoretical Gaussians with the same mean and variance.

theoretical prediction from the experimental results, the L^2-norm was used to quantify the integrated difference of a sample of the theoretical membrane potential V_{sample} and a theoretical Gaussian sample V_{gauss}:

$$L^2(V_{sample}, V_{gauss}) = \int_{-\infty}^{\infty} [\Phi(V)_{sample}(x) - \Phi(V)_{gauss}(x)]^2 \, dx \tag{3.154}$$

Figure 3.16 shows a small discrepancy between a theoretical normal distribution and a sample from the membrane potential trace, offering strong support to the idea of approximating the mebrane potential as a Gaussian distribution.

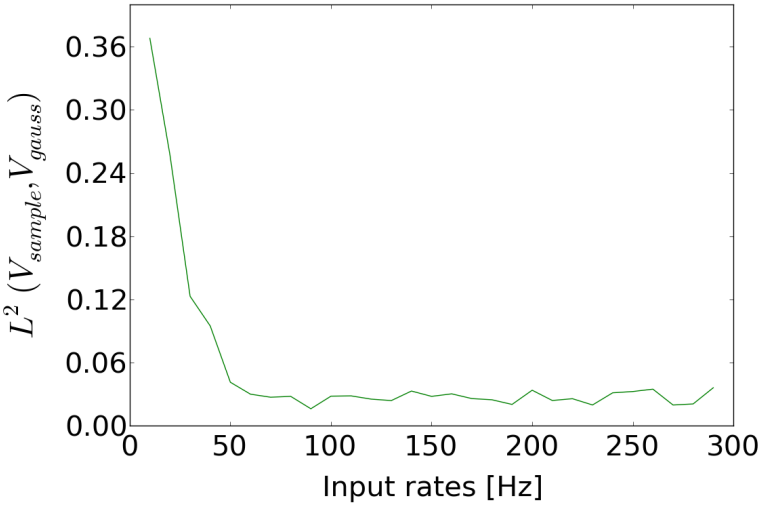

Figure 3.16: The L^2-norm of the difference between a normal distribution and a sample of the simulated membrane potential distribution with the same mean and variance. The synaptic excitatory rate was varied for a constant $\tau_{syn} = 5$ ms. The L^2-norm shows large deviations below input rates < 60 Hz. For higher rates, the norm remains more or less constant and small, assuring a good agreement with the normal distribution.

Conclusion:

If the interspike intervals are shorter than the relaxation constant, then the distribution will be skewed, as shown in fig. (3.15a), and not be similar to a Gaussian at all. If the input rate is high enough (> 60 Hz), then the Central Limit Theorem applies and ensures convergence towards a normal distribution of the membrane potential distribution.

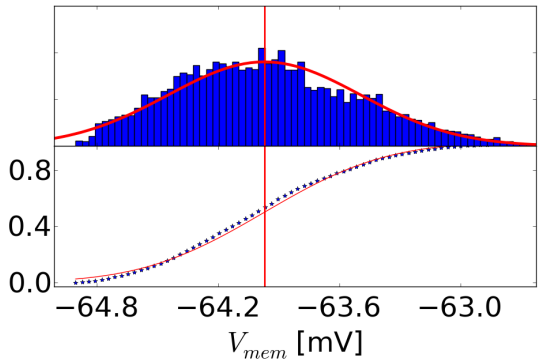

Figure 3.17: A current-based LIF neuron with an input rate of $\nu_{exc} = 100$ Hz

3.2.2 Membrane potential statistics in the conductance based LIF model

For the general case in the conductance based model, a normally distributed membrane potential is not guaranteed formally, because of a critical difference between the current-based and the conductance-based model: the dependence of the PSPs on the membrane potential at the time of input spike arrival.

The Central Limit Theorem, as depicted on p. 53, requires all PSPs to be distributed with a definite mean μ. Formally, this does not apply for a conductance-based model, as the shape of a PSP depends on the membrane potential at the arrival time of the synaptic input.

This means that the random variables, which constitute the impact of the PSPs on the membrane potential, are dependent on the state of the membrane potential. For example, if the membrane potential is close to the inhibitory reversal potential E_{inh}, the impacts of the occuring inhibitory PSPs are very small. They do not contribute equally to the ones close to the threshold. Therefore, a sum of random variables S_N, as described in the Central Limit Theorem on p. 53, is not defined, as every impact of a PSP X_i contributes differently.

However, for high input rates and small synaptic weights causing membrane potentials in $[-50\text{ mV}, -65\text{ mV}]$, there is an obvious similarity of the structure of the current based and the conductance based LIF model, due to following reasons:

- In the current based model, $\tau_{mem} = const.$ ensures identically shaped PSPs. Because of the possibility to approximate $g_{tot}(t) \approx \overline{g_{tot}(t)} = g_{tot}$ (as shown in 3.1.4), the time dependency of the time constant $\tau_{eff}(\cancel{t}) = \frac{C_{mem}}{g_{tot}}$ can be seen as eliminated in the conductance based model.
  This leads to approximately identically shaped PSPs not only in the current-based model, but also in the conductance-based model in a high conductance state, which has been derived in section 3.1.5.

- Although τ_{eff} is approximately constant for all PSPs, their size still would change depending on the distance of the membrane potential to the reversal potentials at the time of the occuring input spike.

  However, in the high conductance state, individual PSPs are relatively small. This results in the membrane potential staying very close to its mean. In this case, one can assume that the deviation of the conductance-based membrane potential from its mean value is small compared to $|E_{rev} - V_{eff}(t)|$. This, in turn, implies that the height of the PSPs remains unaffected by the exact value of $V(t)$ at the onset time of the PSP, as the PSP-shaping term stays approximately constant (equations (3.125), (3.126) on p. 42).

These two points taken into account, it can be concluded that the considerations in the prior section also apply for the conductance-based LIF neuron in the high conductance state. This means that the membrane potential of a conductance-based LIF-neuron can also be regarded as a normal distribution for input parameters (see fig. 3.18) similar to the ones discussed in the previous section (which is also supported by *Destexhe et al.* [2003]).

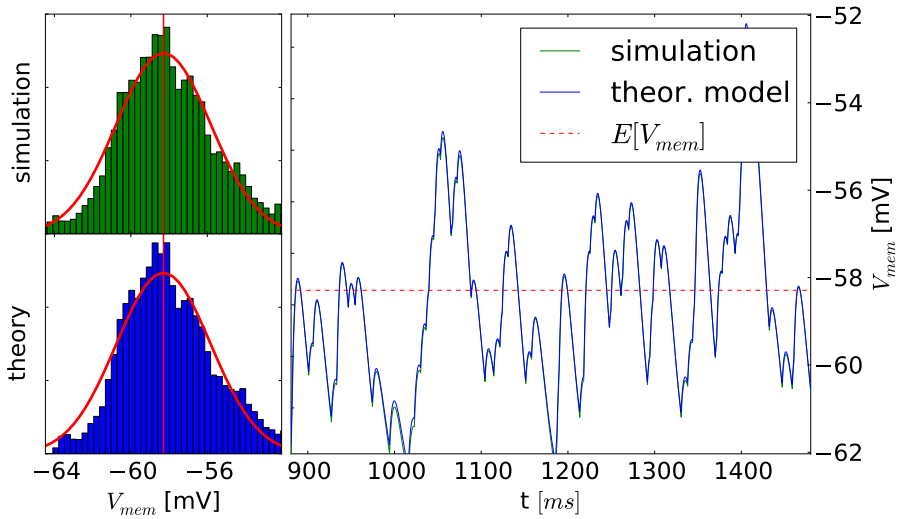

(a) V_{mem} for $\nu_{exc} = 120$ Hz, $w_{exc} = 10^{-2}\mu$S

Figure 3.18: The theoretical and simulated membrane potential trace of a conductance based LIF model with $\nu_{exc} = 120$ Hz, and $w_{exc} = 10^{-2}\mu$S, resulting in $E[V_{mem}] \approx -58$ mV (dashed line). These input rates are already high enough to justify a normal distribution of the membrane potential amplitudes.

In conclusion, the results of this chapter consist in deriving the solution of the leaky integrator differential equations for the current- and conductance-based model[4], which yield an exact (current-based) and approximated (conductance-based) PSPs evoked in the membrane potential by Poisson-distributed synaptic input spikes.

The overall very good quality of these theoretically derived membrane potential traces and also their statistical characteristics (mean μ and variance σ^2) have been examined in sections 3.1.1, 3.1.5 and 3.1.7. Finally, its was shown that the distribution of the membrane potential can be approximated as Gaussian even for medium synaptic rates ($\nu_{syn} > 60$ Hz) for $\tau_{syn} = 5$ ms.

[4]by applying the approximation for the high conductance state

The statistical properties of the normal distribution of the membrane potentials $\mathcal{N}(\mu, \sigma^2)$ will be highly useful in the next chapter, where correlated neuronal dynamics will be introduced upon the knowledge gained in this chapter.

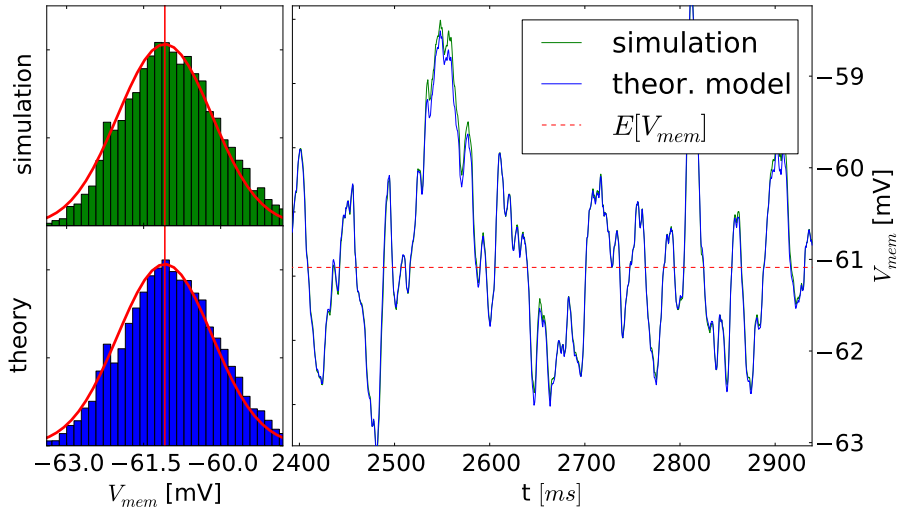

(a) V_{mem} for $\nu_{exc} = \nu_{inh} = 2500$ Hz, $w_{inh} = 5 \cdot 10^{-3}\mu$S, $w_{exc} = 10^{-3}\mu$S

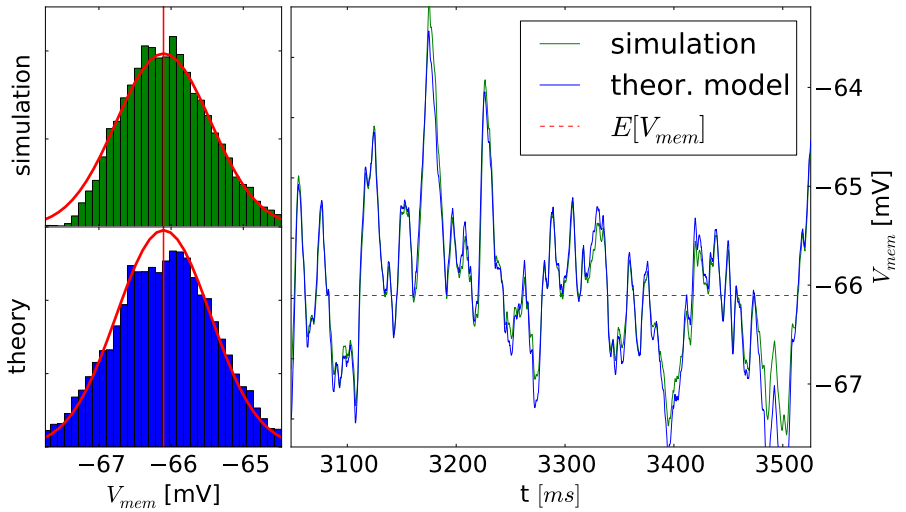

(b) V_{mem} for $\nu_{exc} = \nu_{inh} = 2500$ Hz, $w_{inh} = 18 \cdot 10^{-3}\mu$S, $w_{exc} = 10^{-3}\mu$S

Figure 3.19: In fig. (3.19a), distributions show very good agreement with the theoretical data, and the modeled high frequency PSPs show excellent correspondence to the simulated data.
In (3.19b), both distributions can still be approximated by a normal distribution, but the amplitude distribution of the simulated trace is slightly skewed to the right, because the membrane potential trace comes close to $E_{inh} = -70$ mV.

4 Correlation Measure for subthreshold Membrane Potental Fluctuations

Before one can have a concept of measuring any correlations between two neurons, it is obligatory to define their source and strength. The general concept of correlated neural dynamics between a LIF neuron pair will be ascribed to shared synaptic input, which will be introduced in the following.

The input parameters are the synaptic weights and input rates. The output carrying the impact of these shared input channels will be the membrane potentials of both LIF neurons.

Technically, this means that a part of the total number of Poisson-distrbuted input spikes will have the same arrival times for both neurons. This will be formalized in the following:

The *private* synapses of each neuron generate independent input. The *shared* synapses are connected to both neurons, stimulating them with the exact same spike times.

The spike times for each neuron consists of both parts:

$$\vec{t_1} = \vec{t_{1p}} + \vec{t_s} \tag{4.1}$$

$$\vec{t_2} = \vec{t_{2p}} + \vec{t_s} \tag{4.2}$$

Intuitively, one can assume that the membrane potentials of both neurons exhibit similar fluctuations when shared spiking occurs. Quantifying and predicting this similarity due to shared input on the membrane potentials will be the goal of this chapter, if also the input parameters for each synapse are varied. These parameters were the synaptic weights and rates w_{syn}, ν_{syn}.

4.1 Towards a Correlation Measure: the Joint Probability Distribution:

In the last chapter it was shown that the approximation of the distribution of a membrane potential as a normal distribution is valid for sufficiently high input rates, as shown in the previous chapter. It also was stated that the classification of the membrane potential amplitude distribution as a Gaussian is valid for high input rates and small synaptic weights and would simplify the theoretical treatment of correlations between

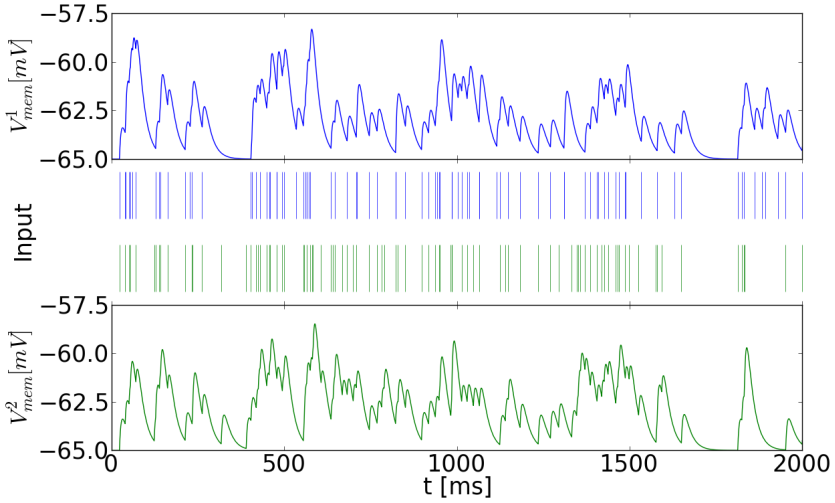

Figure 4.1: Two conductance-based LIF neurons, each neuron with a total amount of excitatory input channels of $Sy_{tot} = 7$. They consist of $Sy_{1p} = Sy_{2p} = 2$ "private" input channels for each neuron and $Sy_s = 5$ input channels "shared" by both neurons. As expected, the membrane potential time course is very similar, due to the high proportion of shared inputs.

neurons to a great extent.

The joint distribution of two membrane potentials $V_1(t)$, $V_2(t)$, each of them following a Gaussian marginal distribution, with respective means μ_1, μ_2 and variances σ_1^2, σ_2^2 can be formulated as a *bivariate normal distribution*[a] with the *correlation coefficient* ρ.

$$p(V_1, V_2) = \frac{1}{2\sigma_1\sigma_2\sqrt{1-\rho^2}} \cdot \exp\left(-z(V_1, V_2)\right) \tag{4.3}$$

$$z(V_1, V_2) = \frac{z_1^2(V_1)}{2 \cdot (1-\rho^2)} + \frac{z_1^2(V_2)}{2 \cdot (1-\rho^2)} - \frac{z_1(V_1) \cdot z_2(V_2)}{1-\rho^2} \tag{4.4}$$

$$z_1(V_1) := \frac{V_1 - \mu_1}{\sigma_1} \qquad z_2(V_2) := \frac{V_2 - \mu_2}{\sigma_2} \tag{4.5}$$

$$\text{and } \rho = \frac{Cov[V_1, V_2]}{\sigma_1 \cdot \sigma_2} \tag{4.6}$$

[a] More generally speaking, the joint membrane potential distribution of a set of neurons can be modeled as a multivariate Gaussian, but since pairwise correlations represent the subject of investigation here, only sets of two variables will be considered.

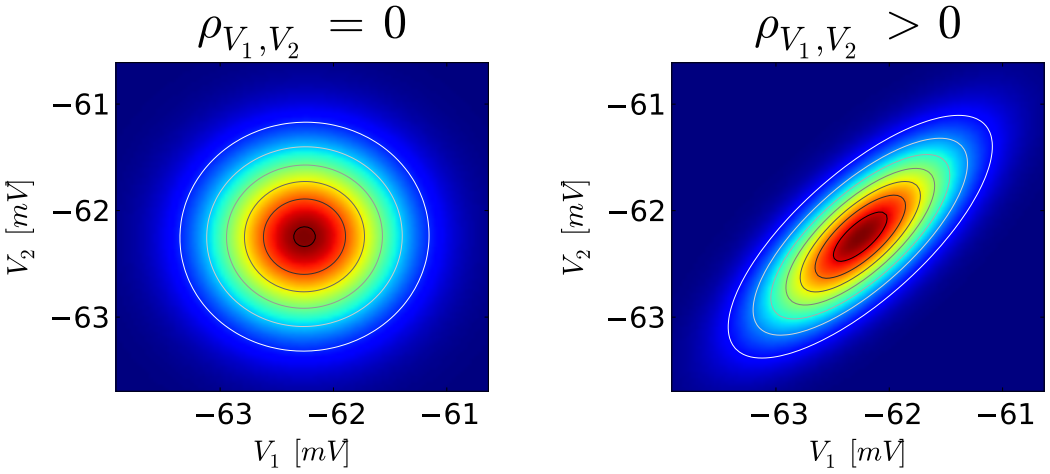

Figure 4.2: An example of bivariate normal distributions of neuron membrane potentials with identical means and variances. The only difference between the two distributions is the correlation coefficient, which describes uncorrelated (left) or correlated (right) membrane potentials V_1, V_2.

A nonzero correlation coefficient ρ is the result of overlapping inputs for both membrane potentials and should be a function of the input parameters. For completely independent potentials ($\rho \to 0$) the distribution would approach the product of two Gaussians:

$$p(V_1, V_2) = p(V_1) \cdot p(V_2)$$

The next section will be dedicated to deriving the exact dependence of the correlation coefficient not only on the configuration of shared and private input synapses, but also on the input parameters w_{syn}, ν_{syn}.

4.1.1 Predicting the Correlation Coefficient

Pearson's product-moment correlation coefficient, which appears naturally in the bivariate Gaussian distribution (eq. (4.3)), is defined as

$$\rho_{V_1,V_2} = \frac{Cov[V_1, V_2]}{\sigma_1 \cdot \sigma_2} \tag{4.7}$$

$$= \frac{E[(V_1 - E[V_1])(V_2 - E[V_2])]}{\sqrt{Var[V_1]} \cdot \sqrt{Var[V_2]}} \tag{4.8}$$

$$\tag{4.9}$$

From the Cauchy-Schwartz inequality it follows that, for any two stochastic variables x and y,

$$Cov[x, y] \leq \sqrt{Var[x] \cdot Var[y]} \ . \tag{4.10}$$

Therefore, $\rho_{xy} \in [-1, 1]$, with the extremal values 1 and -1 standing for linear dependence of x and y, i.e. perfect correlation and anticorrelation, respectively. For independent (and therefore uncorrelated[1]) variables, $\rho = 0$.
The important part in equation (4.7) is the covariance $Cov[V_1, V_2]$ in the numerator. Its value indicates the way both membrane potentials propagate in time in reference to each other. The variances of the PSPs in the denominator of this equation serve merely as normalization constants due to relation 4.10.

[1] The reverse does not hold!

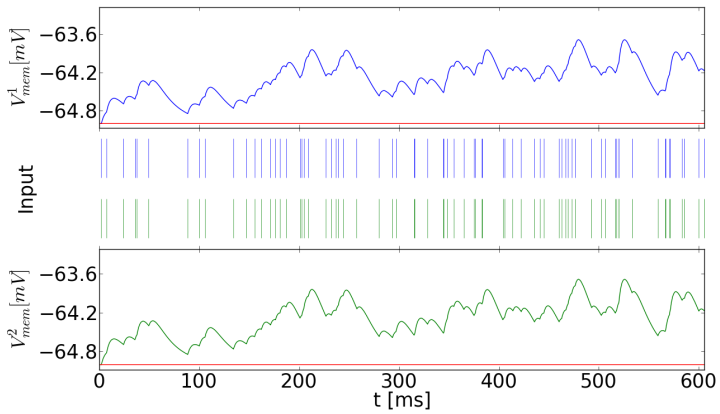

(a) $\rho_{V_1,V_2} = 1$

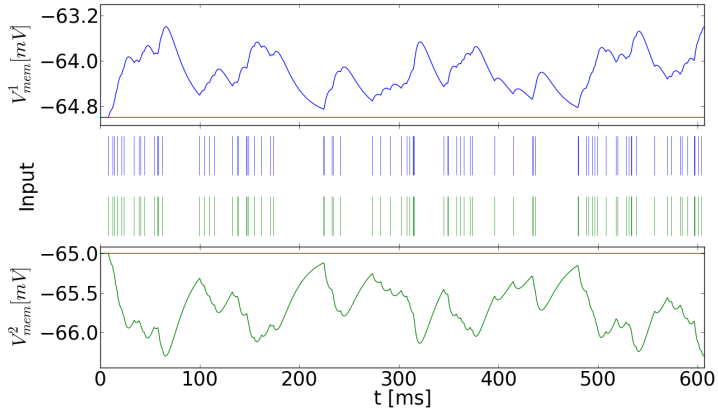

(b) $\rho_{V_1,V_2} = -1$

Figure 4.3: Two membrane potentials with identical input channels and weights illustrate the two bounds of ρ_{V_1,V_2}. The red line shows the resting potential. In Fig. 4.3b, both neurons receive the input as excitatory, and both membranes are depolarized simultaneously. This perfect synchrony results in $\rho_{V_1,V_2} = 1$. In Fig. 4.3b, the upper neuron receives excitatory post synaptic potentials, the lower neuron receives inhibitory post synaptic potentials at the same times, triggering identically shaped PSPs. This guarantees completely anti-synchronous behavior, yielding $\rho_{V_1,V_2} = -1$.

The amount and impact of common input spikes, which directly relates to the number, frequency and synaptic weights of shared and private input channels, determines the correlation coefficient of two neuron membrane potentials. Therefore, the correlation coefficient carries the dependencies

$$\rho_{V_1,V_2} = \rho_{V_1,V_2}\left(\vec{w},\, \vec{\nu},\, s,\, p_1,\, p_2\right) \tag{4.11}$$

$$\text{with } w = \begin{pmatrix} w_1 \\ \cdot \\ \cdot \\ \cdot \\ w_n \end{pmatrix} \text{ and } \nu = \begin{pmatrix} \nu_1 \\ \cdot \\ \cdot \\ \cdot \\ \nu_n \end{pmatrix} \tag{4.12}$$

denoting the weights and frequencies of the n input channels and s and $p_{1,2}$ denoting the subsets of shared and private channels, respectively.

The mean and variance in (4.8) of the corresponding random variables have already been derived in 3.1.5 and 3.1.6, making it possible to derive an analytical expression ρ_{V_1,V_2}.

Let V_{1i} be the sum of PSPs triggered by input spikes from a certain synapse i (temporal summation, p. 13) in the membrane potential of neuron 1. The total covariance of the membrane potentials of both neurons and all channels, is then

$$Cov[V_1, V_2] = Cov\left[\sum_i V_{1i}, \sum_j V_{2j}\right] \tag{4.13}$$

Now, one can separate the sums of all PSPs $\sum_i V_{1i}$, $\sum_j V_{2j}$ into the ones that have been triggered by shared channels and private, independent channels (spatial summation, p. 13).

$$\sum_i V_{1i} = \sum_{1s} V_{1s} + \sum_{1p} V_{1p} \tag{4.14}$$

$$\sum_j V_{2j} = \sum_{2s} V_{2s} + \sum_{2p} V_{2p}\ . \tag{4.15}$$

Note that although the spiking times are identical for all input from shared channels, the impact on the membrane potential through the PSPs can be different in both neurons due to different synaptic weights. This is the reason why V_{1s} and V_{2s} can differ.

The covariance now has the form

$$Cov\left[\left(\sum_{1s} V_{1s} + \sum_{1p} V_{1p}\right), \left(\sum_{2s} V_{2s} + \sum_{2p} V_{2p}\right)\right]\ . \tag{4.16}$$

This can be simplified by exploiting the bilinearity of the covariance,

$$Cov\left[\sum_i X_i, \sum_j Y_j\right] = \sum_i \sum_j Cov[X_i, Y_i] \ . \tag{4.17}$$

Applying this relation to (4.16) yields

$$Cov[V_1, V_2] = \sum_{i,j \in \{s,p\}} Cov\left[V_{1i}, V_{2j}\right] \tag{4.18}$$

The last equation couples the contributions from all possible pairs of input channels. This can be simplified drastically by omitting the covariances that are zero.

This happens for all covariance terms that have private channels as arguments because of their independence from all other channels, shared and private alike. The only contributions to the total covariance came from the products of the terms belonging to shared channels s. Therefore, the covariance can be written as

$$Cov[V_1, V_2] = \sum_s Cov\left[V_{1s}, V_{2s}\right] \tag{4.19}$$

To compute the total covariance, it is necessary to evaluate only the expression for the covariance of the contributions to the membrane potential from single, shared synapses.

This calculation is similar to the ones that were performed in the previous chapter, in section 3.1.6 to yield the variance of kernels triggered by Poisson spike sources.

The covariance can be written as

$$Cov[V_1, V_2] = E[V_1 \cdot V_2] - E[V_1] \cdot E[V_2] \ . \tag{4.20}$$

$E[V_i]$ has already been derived in section 3.1.3, eq. (3.77), whereas for $E[V_1 \cdot V_2]$ the same formalism can be applied as in eq. (3.78), but with this time with the kernel

$$\kappa^2(t) = S_{1s} \cdot S_{2s} \cdot \left(e^{-\frac{t}{\tau}} - e^{-\frac{t}{\tau_{syn}}}\right)^2 \tag{4.21}$$

cond:

$$S_s = \frac{w_s \cdot (E_s - \overline{V_{eff}}) \cdot \tau_g}{g_{tot} \cdot \tau_{eff}}$$

curr:

$$S_{syn} = \frac{i_s \cdot \tau_c}{g_L \cdot \tau_{mem}} \tag{4.22}$$

with τ, τ_g, etc. as defined on p. 42.
The total covariance then becomes

$$Cov[V_1, V_2] = \sum_s \nu_s \cdot S_{1s} \cdot S_{2s} \cdot \int_0^\infty \left(e^{-\frac{t}{\tau}} - e^{-\frac{t}{\tau_{syn}}} \right)^2 dt \tag{4.23}$$

This class of integrals has already been solved in the previous chapter in section 3.1.6. The result can be identified immediately:

$$Cov[V_1, V_2] = \sum_s \nu_s \cdot S_{1s} \cdot S_{2s} \cdot \left[\frac{\tau}{2} + \frac{\tau_{syn}}{2} - 2 \cdot \frac{\tau \cdot \tau_{syn}}{\tau + \tau_{syn}} \right] \tag{4.24}$$

The variances of the membrane potentials can also be computed as in section 3.1.6, eq. 3.137, including the private, as well as the shared contributions:

$$Var[V_1] = \left(\sum_s \nu_s \cdot S_{1s}^2 + \sum_{1p} \nu_{1p} \cdot S_{1p} \right) \cdot \left(\frac{\tau}{2} + \frac{\tau_{syn}}{2} - 2 \cdot \frac{\tau \cdot \tau_{syn}}{\tau + \tau_{syn}} \right) \tag{4.25}$$

$$Var[V_2] = \left(\sum_s \nu_s \cdot S_{2s}^2 + \sum_{2p} \nu_{2p} \cdot S_{2p} \right) \cdot \left(\frac{\tau}{2} + \frac{\tau_{syn}}{2} - 2 \cdot \frac{\tau \cdot \tau_{syn}}{\tau + \tau_{syn}} \right) \tag{4.26}$$

Plugging $Cov[V_1, V_2]$, $Var[V]$, into eq. (4.7) leads to the result of the correlation coefficient:

$$\rho_{V_1,V_2} = \frac{\sum_s \nu_s \cdot S_{1s} \cdot S_{2s}}{\sqrt{\left(\sum_s \nu_s \cdot S_{1s}^2 + \sum_{2p} \nu_{1p} \cdot S_{1p}^2 \right) \cdot \left(\sum_s \nu_s \cdot S_{2s}^2 + \sum_{2p} \nu_{2p} \cdot S_{2p}^2 \right)}} \tag{4.27}$$

This expression can still be simplified explicitly for each LIF neuron model.

For the conductance-based LIF model, equation (4.27) results in

$$\rho_{V_1,V_2} = \frac{\sum_s \nu_s \cdot w_{1s} \cdot w_{2s} \cdot (E_{1s} - \overline{V_{eff1}}) \cdot (E_{2s} - \overline{V_{eff2}})}{\sqrt{\prod_{i \in \{1,2\}} \left[\sum_s \nu_s \cdot w_{is}^2 (E_{is} - \overline{V_{eff_i}})^2 + \sum_{ip} \nu_{ip} \cdot w_{ip}^2 (E_{ip} - \overline{V_{eff_i}})^2 \right]}} \tag{4.28}$$

The result for the current-based case is then

$$\rho_{V_1,V_2} = \frac{\sum_s \nu_s \cdot i_{1s} \cdot i_{2s}}{\sqrt{\prod_{j\in\{1,2\}} \left[\sum_s \nu_s \cdot i_{js}^2 + \sum_{jp} \nu_{jp} \cdot i_{jp}^2 \right]}} \tag{4.29}$$

These results can be summarized at this point:

Correlation coefficient

The correlation coefficient ρ_{V_1,V_2} of a LIF neuron pair with s shared and p private synapses, equal synaptic currents (current-based) i_{syn} or (conductance-based) weights w_{syn} firing at input rates ν_{syn_s} and ν_{syn_p}, evoking synaptic PSPs S_{syn} [a] is predicted as:

conductance-based LIF model:

$$\rho_{V_1,V_2} = \frac{\sum_s \nu_s \cdot w_{1s} \cdot w_{2s} \cdot (E_{1s} - \overline{V_{eff1}}) \cdot (E_{2s} - \overline{V_{eff2}})}{\sqrt{\prod_{i\in\{1,2\}} \left[\sum_s \nu_s \cdot w_{is}^2 (E_{is} - \overline{V_{eff_i}})^2 + \sum_{ip} \nu_{ip} \cdot w_{ip}^2 (E_{ip} - \overline{V_{eff_i}})^2\right]}} \tag{4.30}$$

current-based LIF model:

$$\rho_{V_1,V_2} = \frac{\sum_s \nu_s \cdot i_{1s} \cdot i_{2s}}{\sqrt{\prod_{j\in\{1,2\}} \left[\sum_s \nu_s \cdot i_{js}^2 + \sum_{jp} \nu_{jp} \cdot i_{jp}^2\right]}} \tag{4.31}$$

- The input correlation is carried in the numerator, with the products of the weights/currents determining the correlation strenghts. Positive contributions to the correlation coefficient arise if products of excitatory-excitatory weights/currents exist. This increases the synchronous fluctuation of both membrane potentials. Antisynchronuous fluctuations, and therefore negative contributors in the correlation coefficient, arise for excitatory-inhibitory coupling. Lack of shared channels automatically results in a correlation coefficient of zero.
- If synchronuous and antisynchronuous fluctuations exist, the correlation coefficient can not directly measure the number of private channels. If, for example, the excitatory-excitatory coupling equals the excitatory-inhibitory coupling, the numerators in 4.30 and 4.31 become zero, yielding the same result as if there was no shared input whatsoever.

[a] The reversal potentials E_{syn} and average effective potential $\overline{V_{eff}}$ for the conductance-based model are as given on p. 42

From this point on, the correlation coefficient from eq. 4.30 and 4.31, respectively, will be the measure of correlations for subthreshold membrane potential fluctuations.

In the next section, it will be shown that the agreement is very good between the theoretical correlation coefficient, as derived above, and the correlation coefficient obtained directly from the simulated voltage traces.

4.2 The Correlation Coefficient: Prediction and Simulation

The quality of the predicted correlation coefficient can be tested by varying all possible input parameters, as well as the number of shared and private input channels.

In this section, simplifications will be made to test the quality of the theoretical correlation coefficient for regions of high excitation and high inhibition. The latter was identified as a problematic parameter space for the computation of the statistical values, as described in section 3.1.7.

For the analysis of the theoretical correlation coefficient, its values will be compared to the correlation coefficient resulting from the simulation if the ratio

$$\frac{\text{shared channels}}{\text{private channels}} \tag{4.32}$$

is changed. To simplify the comparison between the theoretical results and those calculated from the simulation, the following parameter space will be restricted as follows:

- Input rates from all channels will be equal, $\nu_s = \nu_{1p} = \nu_{2p}$. Therefore, the change of shared or private input will be regulated by changing the amount of shared or private channels.
- The synaptic weights/currents will be chosen equal for each channel, $w_{1s} = w_{2s} = w_{1p} = w_{2p}$, also only inhibitory-inhibitory and excitatory-excitatory coupling are activated. This restricts the theoretical correlation coefficient to $\rho \in [0, 1]$, but not the analysis for different parameter ranges, since it is possible to choose the total excitatory and inhibitory input rates.
- The total numbers of inhibitory and excitatory input channels will stay fixed at $N_{inh} = N_{exc} = N_{chan} = 100$. Therefore, an increase in shared channels implies a decrease of private channels. Additionally, both neurons will have the same total number of private channels, $P_1 = P_2 = P_{inh} = P_{exc} =: P$. As a consequence, the inhibitory input rates will always be equal to the excitatory rates.

Due to these simplifications of equations 4.30 and 4.31, the theoretical correlation coefficient becomes completely independent from the input rates and weights/currents, the only dependence being the numbers of total shared and private channels S and P.

$$\rho_{V_1,V_2} = \frac{S}{S+P} = \frac{S}{N_{chan}} \tag{4.33}$$

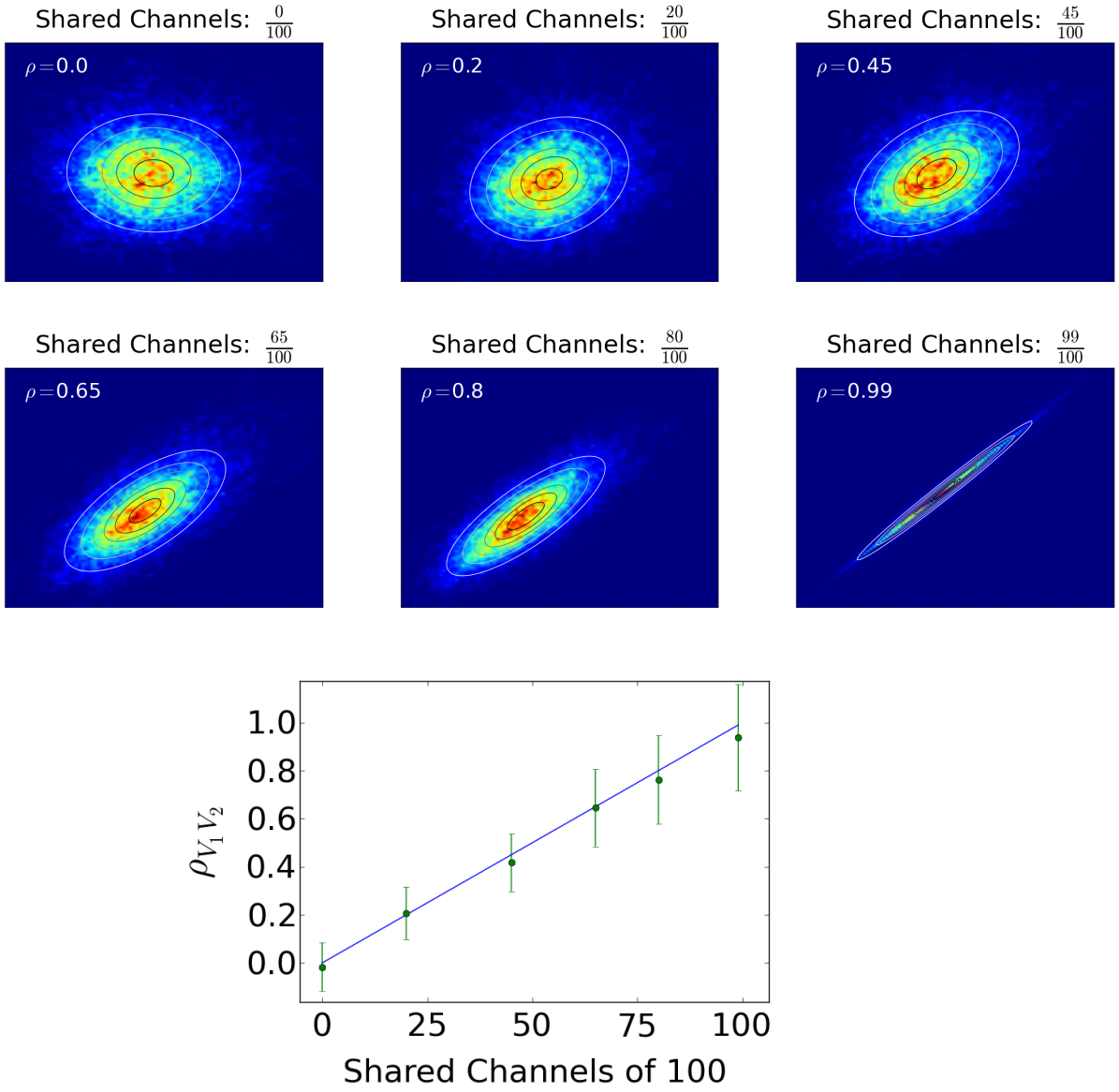

Figure 4.4: The figures show distributions of bivariate normal membrane potentials in a subthreshold regime. The contours on these color plots indicate the theoretical distribution, which show very good agreement with the simulation data. As the ratio $\frac{\text{shared channels}}{\text{private channels}}$ increases, the shape of the distribution, as well as the contours become more elliptical, due to the increase of the correlation coefficient. Fig. 4.4g shows the linear increase of the correlation coefficient with an increasing number of shared channels for all configurations. The theoretical correlation coefficient, as defined in eq. (4.33), is in compliance with the simulation results. All simulations were conducted with 50 biological seconds simulation time.

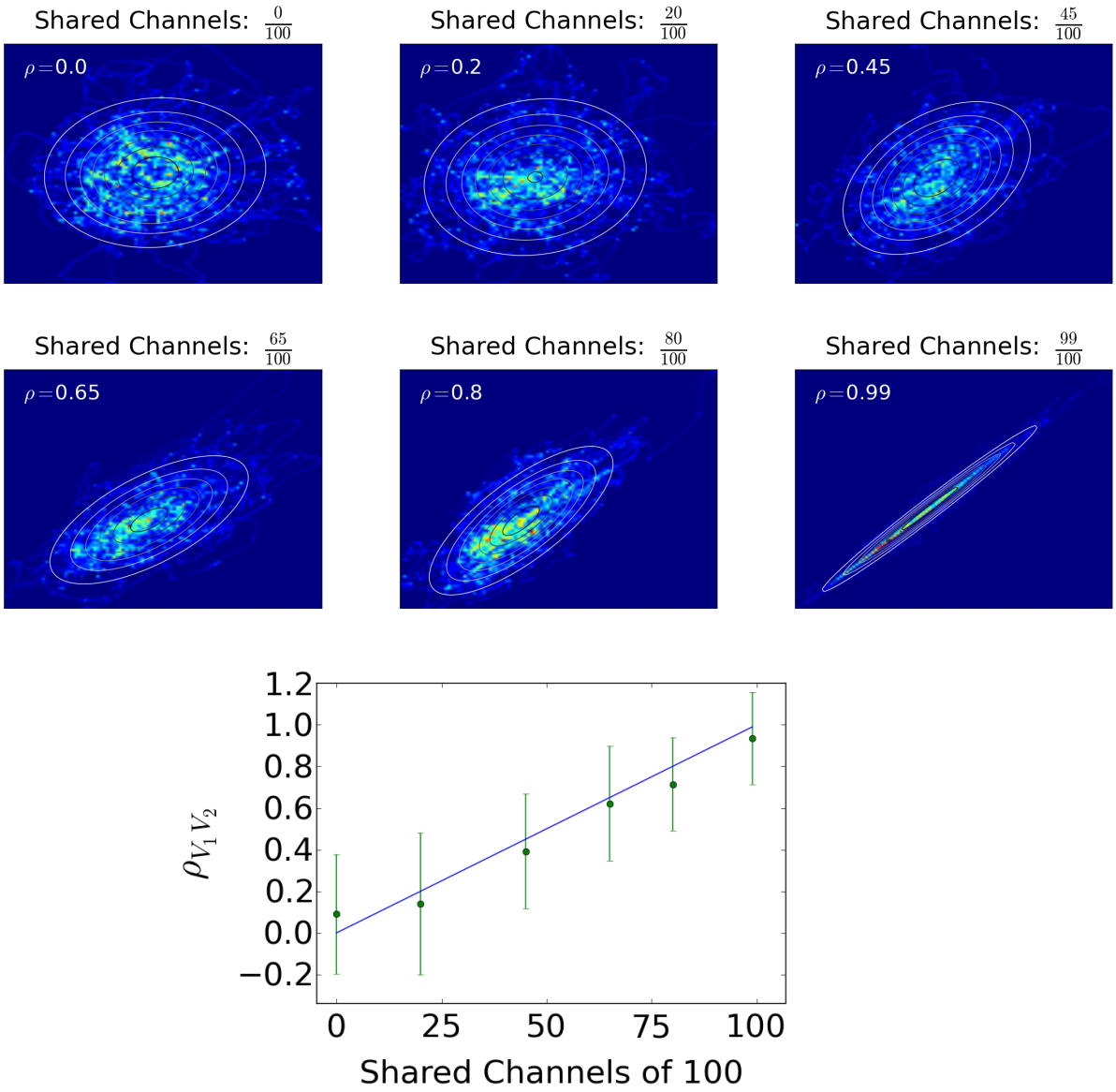

Figure 4.5: The figures show bivariate membrane potential distributions for an increasing ratio of $\frac{\text{shared channels}}{\text{private channels}}$, with the contours indicating the theoretical bivariate Gaussian. The simulation duration is 5 biological seconds, only a tenth of the simulations in fig. 4.4. To that effect, the sample distributions exhibit significant distortions. The correlation coefficients are shown in 4.5g and yield a good approximation to the theoretical values, albeit with larger standard deviations than in 4.4g.

Im this form, ρ_{V_1,V_2} will stay constant for a particular ratio $\frac{S}{P}$, allowing to test whether this applies to all parameter ranges of this measure, or is affected by the effects of the proximity of E_{inh} in the conductance-based LIF model.

For the current-based LIF model the agreement between the theoretical correlation coefficient and the one from the simulated case is expected to be perfect in the limit of $T_{sim} \to \infty$, due to the exact derivation of its statistical values in the previous chapter.

Figures 4.4 and 4.2 below show joint distributions of conductance-based LIF membrane potential traces. The overlayed contours belong to the indicated bivariate normal distribution with the theoretical statistical values.

The plots in fig. 4.4 show simulations with a duration of 50 biological seconds, whereas the figures are a result from simulations of 5 biological seconds.
The simulation time required for these plots has to be increased considerably as compared to the one-dimensional analysis that has been conducted in the last chapter, because of the much larger relevant configuration space of the bivariate normal distribution.

Figure 4.4 shows bivariate distributions of the two conductance-based LIF membrane potentials with an increasing number of shared channels, as discussed above. The theoretical distribution is indicated by the contours and overlaps excellently with the illustrated density of the data points. The increase of the correlation coefficient can also be seen in the changing shape of the bivariate distribution, as the initially spherical shape becomes more elliptic with an increase of overlapping input channels.

To analyze the change of the correlation coefficient more extensively, simulations over a wide range of input parameters have been performed, with an expected correlation coefficient as given in 4.33.

The chosen parameter ranges are identical with the ones from the previous chapter, as defined in section 3.1.7.

Conclusively, it can be stated that the prediction of the correlation coefficient for increasing shared channels shows very good results, as the figures in 4.2 indicate. The correlated subthreshold fluctuations of a LIF neuron pair can therefore be quantified by the correlation coefficient. This also can be done for a wide range of parameters, as fig. 4.6 indicate. The appearing deviations between the simulation correlation coefficient and the one derived theoretically, are merely statistical errors. Their influence will be discussed in the following.

4.2.1 Estimating the Statistical Errors of the Correlation Coefficient

A particularly important point concerns the duration of the simulations. The quality of the approximation towards the theoretical correlation coefficient is influenced by the

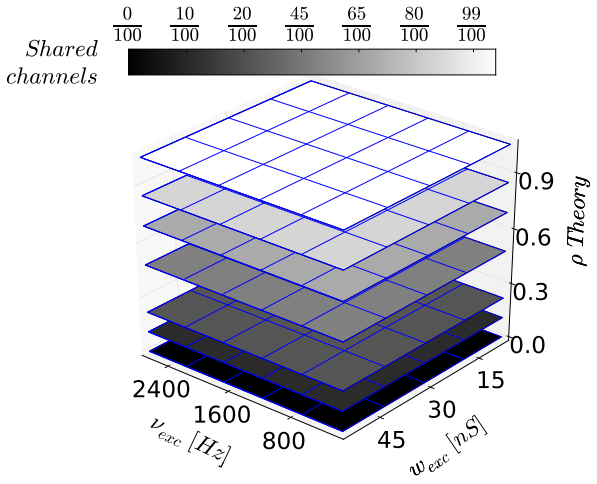

(a) Conductance-based theoretical prediction of ρ

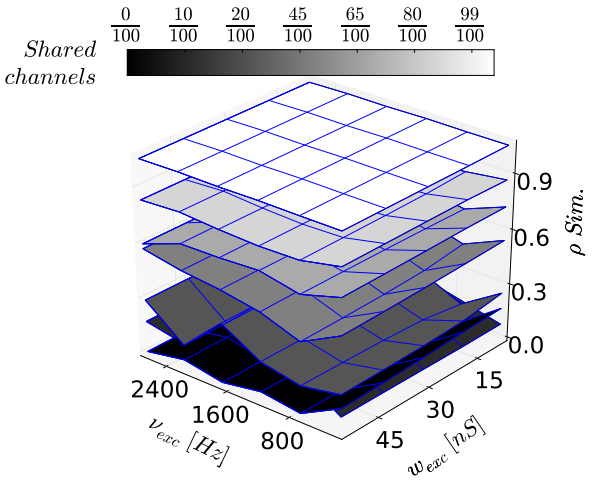

(b) Conductance-based simulation results of ρ

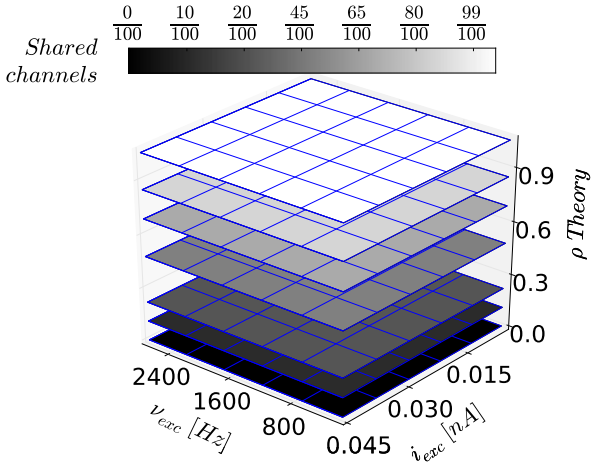

(c) Current-based theoretical prediction of ρ

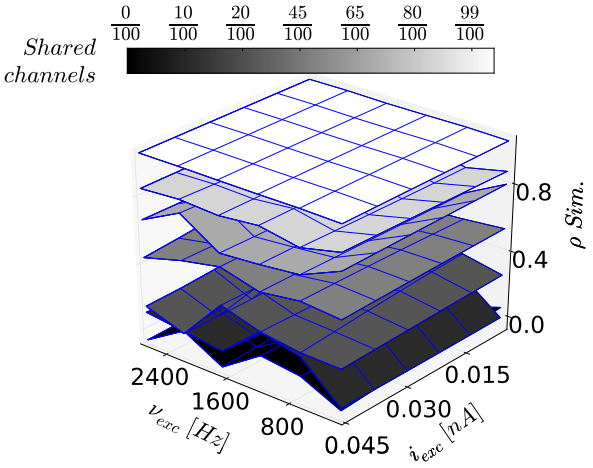

(d) Current-based simulation results of ρ

Figure 4.6: Figures 4.6a and 4.6b show the correlation coefficients of the simulation results for different parameters in the conductance-based model and its prediction. The theoretical hypersurfaces are not dependent on synaptic weights and input rates (see eq. 4.33). It can be observed that the fluctuations of the correlation coefficient increase in the hypersurfaces for smaller number of shared channels. This is also true for the current-based simulation, as shown in fig. 4.6d, where the same trend for a decreasing number of shared channels can be observed. (See text for further details)

simulation time. The results from 4.2, for example, are obtained for the exact same configurations of shared and private channels with the same input parameters as in fig.

4.4, but with a simulation time of 5 biological seconds. Consequently, the distribution of the gathered data from this simulation represents a highly distorted version of the expected bivariate Gaussian.

The difference in quality between fig. 4.4 and 4.2 can be ascribed to the simulation time T_{sim}. The joint distribution of the membrane potentials converges slower (in terms of required samples, which is equal to $T_{sim}/\Delta t$) to the bivariate distribution than a one-dimensional distribution. Intuitively, this is due to the data points being required to cover an interval, in the univariate use, and and an area, in the bivariate use.
For a fixed T_{sim}, the lower the number of shared channels is, the stronger the deviations from the target bivariate Gaussian become. This phenomenon can be explained by the argument of the exponential in equation 4.4, which can be interpreted as the equation of an elliptic geometrical shape in the two-dimensional Euclidean space. The following calculations will show that an increasing correlation coefficient decreases the area of a given confidence interval, leading to less distortion in the sample distribution for a given number of data points.

Considering a fixed bivariate normal distribution $p(V_1, V_2)$, as given in 4.3,

$$p(V_1, V_2) \cdot n = e^{-z(V_1,V_2)} \tag{4.34}$$

$$\text{with } n = 2 \cdot \pi\sigma_1\sigma_2\sqrt{1-\rho^2}\ , \tag{4.35}$$

the natural logarithm can be applied on both sides to yield

$$ln\left(\frac{1}{p(V_1, V_2) \cdot n}\right) = z(V_1, V_2) \tag{4.36}$$

$$\overset{4.4}{=} \frac{z_1^2(V_1)}{2 \cdot (1-\rho^2)} + \frac{z_1^2(V_2)}{2 \cdot (1-\rho^2)} - \frac{z_1(V_1) \cdot z_2(V_2)}{1-\rho^2}\ . \tag{4.37}$$

So for some value $\tilde{p} \ll 1$ (such that samples with a smaller probability almost never occur), it holds that

$$R = \left(\frac{z_1^2(V_1)}{2 \cdot (1-\rho^2)} + \frac{z_1^2(V_2)}{2 \cdot (1-\rho^2)} - \frac{z_1(V_1) \cdot z_2(V_2)}{1-\rho^2}\right)\ , \tag{4.38}$$

with

$$R =: A \cdot z_1^2(V_1) + B \cdot z_2^2(V_2) + C \cdot z_1(V_1) \cdot z_2(V_2) \tag{4.39}$$

This is the canonical equation for an ellipse with R defining its size (constant!), and ρ the shape. If $\rho > 0$, the main axis of the ellipse lies along the line $z_1(V_1) = z_2(V_2)$. For $\rho < 0$, the main axis lies along $z_1(V_1) = -z_2(V_2)$.

Because a multivariate Gaussian is a quasiconcave function, the set of arguments for which $p(\vec{x}) \geq \tilde{p}$, $\forall \tilde{p} \in \mathbb{R}$ is convex. Since the boundary of the set $\{(V_1, V_2)|p(V_1, V_2) \geq \tilde{p}$ is the ellipse from eq. 4.39, the complete set contains all the interval points of the ellipse and therefore has a cardinality equal to $Ar \cdot D_a$, with Ar being the surface of the ellipse and D_n the configuration space density.

$$\Rightarrow N := card\left(\{(V_1, V_2)|p(V_1, V_2) \geq \tilde{p}\}\right) = \frac{2 \cdot \pi \cdot R \cdot D_n}{\sqrt{4 \cdot A \cdot B - B^2}} \ . \tag{4.40}$$

Inserting the substitutes for A, B, C in this equation results in

$$N = 2 \cdot \pi \cdot \sigma_1 \cdot \sigma_2 \cdot z(V_1, V_2) \cdot \sqrt{1 - \rho^2} \cdot R \cdot D_n \tag{4.41}$$

It now becomes clear that because the area in configuration space to be sampled from decreases with increasing $|\rho|$, for a fixed T_{sim}, the distribution of the sampled set approximates the target distribution better as the number of shared channels increases.

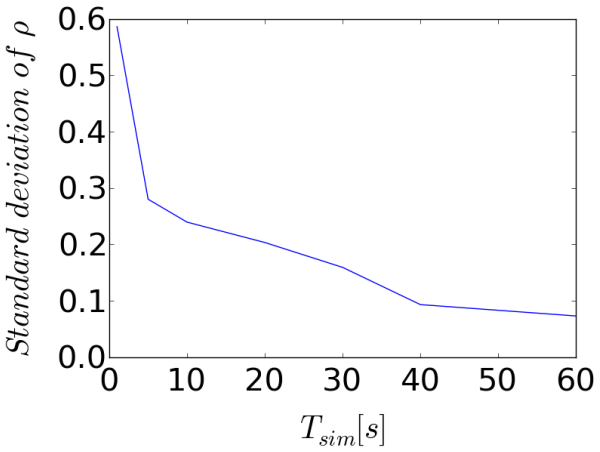

(a) Influence of the increase in simulation time T_{sim} on σ_ρ

Figure 4.7: The figure shows the plotted standard variation of the correlation coefficient for increasing simulation times T_{sim} (and therefore, the sample size)), for $S = 0$. The deviations show a significant decrease.

5 Investigating Correlations in the Spiking Activity of Neurons

In the previous chapter, synaptic input correlations were introduced and an analytic expression for their effect on the correlation coefficient of subthreshold membrane potential traces, was derived.

In this chapter, input correlations will again originate from the shared input channels, but neuronal dynamics will not be restricted to subthreshold fluctuations, like in the previous chapter. Instead, output spiking will be subject of analysis for a correlated neuron pair.

Under various circumstances, being able to predict correlated spiking can be very useful. In many cases, correlated input heavily distorts network dynamics, such as in attractor configurations (*Lundqvist et al.* [2006]) or in networks exhibiting asynchronous irregular behaviors (*Kremkow et al.* [2010]). Especially in the context of neuromorphic hardware, where neurons might be forced to share inputs due to bandwidth limitations, correlation prediction becomes an indispensable tool for minimizing this usually undesired effect.

The simplest approach to describing the spiking behavior of a neuron is to define a binary variable encoding the "state" of a neuron.

In this thesis, *ON-states* will be states which coincide with spiking activity of a postsynaptic neuron. An ON-state is initialized by an output spike and temporally restricted by a fixed time bin t_{ON}. This means that the membrane potential must at least reach the spiking threshold $E_{thresh} = -50$ mV to activate such a state. In case of renewed spiking within an ON-state, the state is instantly refreshed for another period t_{ON}. When multiple events of this kind occur, the output spike sequence is often referred to as *burst spikes*. Spikes occuring in an interspike interval longer than t_{ON}, will be called *single spikes*.
Reasonable values of the newly introduced parameter t_{ON} are yet to be found. They are assumed to be somehow related to the input parameters

$$\{\nu_{exc}, \nu_{inh}, w_{exc}, w_{inh}\} \ . \tag{5.1}$$

In the past chapter, the correlation coefficient has proven to be a reliable measure to predict neuronal membrane fluctuations in dependence of these input parameters. Now,

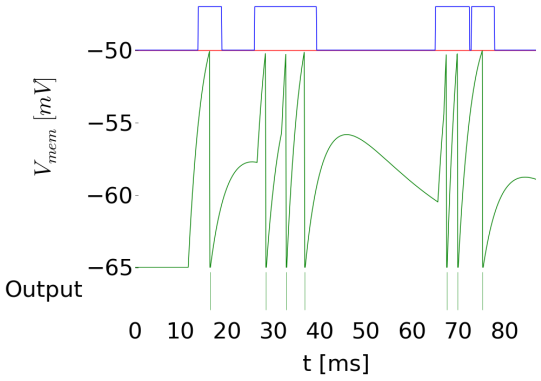

Figure 5.1: ON-states caused by a strong input.

instead of applying it to voltage traces, it can be applied to the newly defined state variable

$$s(t) = \begin{cases} 1 & \text{if } \exists\ t_{spike} \in (t - t_{ON}, t] \\ 0 & \text{else} \end{cases} \tag{5.2}$$

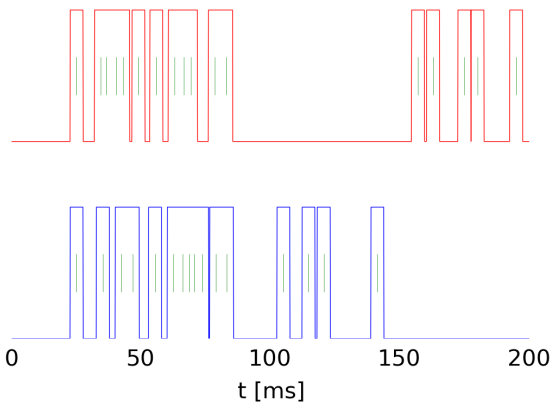

Figure 5.2: ON/OFF-states of a neuron pair with shared inputs. The green lines represent the output spikes of the two neurons.

As the interest lies in considering a neuron pair with each neuron being in a state as expressed in eq. (5.2), the configuration space of two neurons consists of 4 possible states:

$$[s_1, s_2] \in \{[1,1], [0,0], [1,0], [0,1]\} =: \Omega \tag{5.3}$$

For the state variables s_1 and s_2 of the two neurons in question, the correlation coefficient can be written as

$$\rho_{s_1,s_2} = \frac{Cov[s_1, s_2]}{\sqrt{Var[s_1] \cdot Var[s_2]}} = \frac{E[s_1, s_2] - E[s_1] \cdot E[s_2]}{\sqrt{[E[s_1^2] - E^2[s_1]] \cdot [E[s_2^2] - E^2[s_2]]}} \tag{5.4}$$

$$= \frac{\sum\limits_{(s_1,s_2)\in\Omega} p(s_1, s_2) \cdot s_1 \cdot s_2 - \sum\limits_{s_1\in\{0,1\}} p(s_1)s_1 \sum\limits_{s_2\in\{0,1\}} p(s_2)s_2}{\sqrt{\prod\limits_{n\in\{1,2\}} \left[\sum\limits_{s_n\in\{0,1\}} p(s_n)s_n^2 - \left(\sum\limits_{s_n\in\{0,1\}} p(s_n)s_n\right)^2\right]}} \tag{5.5}$$

In every sum, all terms containing either $s_1 = 0$ of $s_2 = 0$ disappear, leaving only

$$\rho_{s_1 s_2} = \frac{p_{11} - p_1^1 \cdot p_1^2}{\sqrt{\left(p_1^1 - (p_1^2)^2\right)\left(p_1^2 - (p_1^2)^2\right)}} \tag{5.6}$$

$$\text{with } p_{ij} = p(s_1 = i, s_2 = j) \tag{5.7}$$

$$\text{and } p_i^j = p(s_j = i) \tag{5.8}$$

These used notations will be formally introduced in the next section, but are required here to illustrate the instability of ρ at low spike rates.

For either very strong ($p_{11} \to 1, p_i^j \to 1$) or very weak ($p_{11} \to 0, p_i^j \to 0$) input, both numerator and denominator in the fraction from eq. (5.6) approach zero, making only the slightest error in their calculation or measurement have an arbitrarily large impact on the value of ρ. Therefore, for an exhaustive description of state correlations under a broad spectrum of input regimes, a more stable measure is required.

Essentially, this means that the measure should encode the difference between the true joint probability distribution $p(s_1, s_2)$ and the (hypothetical) situation where the states are independent: $p^1(s_1, s_2) = p(s_1) \cdot p(s_2)$.

5.1 A New Correlation Measure: Symmetric Uncertainty[1]

As implied in the last section, there are at least two conditions which have to be fulfilled by the new measure. It must be capable of detecting (anti-)synchrony and has to operate

[1] This measure has already been proposed in 2009 by M. Petrovici and J. Bill, albeit for a very particular case of input regimes

on the state function $s(t)$ described in (5.3).

The probability $p(s_i = 1)$ of finding neuron i in an ON-state in a simulation duration T_{sim}, and only one occuring spike would yield a probability of

$$p(s^i = 1) = \frac{t_{ON}}{T_{sim}} \tag{5.9}$$

A particular measure which takes this into account, is the *Kullback-Leibler divergence* (see *Dayan and Abbott* [2001]). Given a random variable X with the distributions $p(X)$, and $q(X)$, the Kullback-Leibler divergence is defined as

$$D(p(X)||q(X)) = \sum_x q(x) \cdot \log\left(\frac{q(x)}{p(x)}\right) \ . \tag{5.10}$$

$$D(p(S_1, S_2)|p(S_1) \cdot p(S_2)) = \sum_{s_1 \in \{0,1\}} \sum_{s_2 \in \{0,1\}} p(s_1, s_2) \cdot \log\left(\frac{p(s_1, s_2)}{p(s_1) \cdot p(s_2)}\right) \tag{5.11}$$

This equation is intimately connected to the concept of entropy. In the context of Information theory, this quantity can be described as a measure of uncertainty of random variable A, with $a \in \{a_1, a_2, \dots\}$ being the observables of this variable.

$$H(A) = -\sum_a p(a) \cdot \log p(a) \ , \tag{5.12}$$

For the configuration space chosen above, there are two extreme cases which can be used to illustrate this quantity. The first is the case where the probability of finding neuron N^1 in the ON-state is very low,

$$p(s_1 = 1) \approx 0 \Rightarrow -p(s_1 = 1) \cdot \log p(s_1 = 1) \xrightarrow{\text{rule of L'Hôspital}} 0 \tag{5.13}$$

This means that if a state occurs too rarely, it will not contribute much to the entropy. In the other case

$$p(s_1 = 1) \approx 1 \Rightarrow \log p(s_1 = 1) = 0 \tag{5.14}$$

the outcome is not "uncertain" at all, as it always shows that the neuron is in its ON-state.

The maximum entropy for binarily coded information is given if $p(s_1 = 1) = p(s_1 = 0) = \frac{1}{2}$, where both states appear often enough to contribute but there is still a high uncertainty to find the neuron in a certain state.

These considerations will be important in understanding the new measure of synchrony, after modifying equation (5.11) by using the *Bayes' theorem*

$$p(A|B) = \frac{p(B|A)}{p(A) \cdot p(B)} \ . \tag{5.15}$$

This yields

$$\begin{aligned} D(p(S_1, S_2)||p(S_1) \cdot p(S_2)) &= \sum_{s_1, s_2 \in \Omega} p(s_1, s_2) \cdot \log \left(\frac{p(s_1|s_2)}{p(s_1)} \right) && (5.16) \\ &= \sum_{s_1, s_2 \in \Omega} p(s_1, s_2) \cdot p(s_2) \cdot p(s_1, s_2) \cdot \log p(s_1|s_2) && (5.17) \\ &\quad - \sum_{s_1, s_2 \in \Omega} p(s_2) \cdot p(s_1|s_2) \log p(s_1) && (5.18) \\ &= \underbrace{\sum_{s_2 \in \{0,1\}} p(s_2) \sum_{s_1 \in \{0,1\}} p(s_1|s_2) \cdot \log p(s_1|s_2)}_{-H(S_1|S_2)} && (5.19) \\ &\quad \underbrace{- \sum_{s_1 \in \{0,1\}} p(s_1) \cdot \log p(s_1)}_{H(S_1)} \end{aligned}$$

The RHS term is simply the entropy of the neuron state S_1. The LHS term is a negative conditional entropy $H(S_1|S_2)$, which will be explained now.

$$-H(S_1|s_2) = \sum_{s_1 \in \{0,1\}} p(s_1|s_2) \cdot \log p(s_1|s_2) \tag{5.20}$$

determines the negative entropy if S_2 remains in a certain state while summing over the contributions of all states of S_1. This negative entropy is a result of the total uncertainty of S_1 after observing a predetermined state s_2. Summing over all possible states of S_2 yields the total conditional entropy

$$\begin{aligned} H(S_1|S_2) &= \sum_{s_2} p(s_2) \cdot H(S_1|s_2) && (5.21) \\ &= - \sum_{s_2} p(s_2) \sum_{s_1} p(s_1|s_2) \cdot \log p(s_1|s_2) \ . && (5.22) \end{aligned}$$

The conditional entropy $H(S_1|S_2)$ shows what remains of the entropy of S_1 after S_2 is observed. This is also called *noise entropy*, because what remains of S_1 that is not due to S_2 is presumably due to noise. Subtracting this from $H(S_1)$ one remains with everything in S_1 that is due to S_2, and vice-versa.

$$D(p(S_1, S_2)||p(S_1) \cdot p(S_2)) = H(S_1) - H(S_1|S_2) =: I(S_1, S_2) \tag{5.23}$$

This quantity is known as the *Mutual Information* $I(S_1, S_2)$, and satisfies all conditions of a metric, which will not be shown here[2].

For example, if observing S_2 has no influence on the entropy of S_1, then $H(S_1|S_2) = H(S_1) \Rightarrow I(S_1, S_2) = 0$
Obtaining the mutual information is a crucial step towards a measure that can detect (anti)synchronous firing states, as it considers (anti)synchronous states by also evaluating probability states where one neuron spikes and the other is tranquil: $p(s_1 = 0, s_2 = 1)$, $p(s_1 = 1, s_2 = 0)$

A remaining concern of this measure is its overall dependence on the spike rates of the individual neurons, which obviously change when input parameters ν_{syn}, w_{syn} are altered. To have a normalized measure of the dependency of the ON/OFF-states of the neuron pair, different methods can be considered. One possibility, which does not affect symmetry, lies in the division by the sum of the individual entropies, because

$$I(N^1, N^2) \leq H(N^1), H(N^2) \ , \tag{5.24}$$

This finally yields the *Symmetric Uncertainty*.

$$SU(S_1, S_2) = \frac{2 \cdot I(S_1, S_2)}{H(S_1) + H(S_2)} \tag{5.25}$$

$$SU(S_1, S_2) \in [0, 1] \tag{5.26}$$

This denomination stems from *Witten and Frank* [2005] and can be somewhat misleading, since one would expect "uncertainty" to decrease when two random variables become more correlated. However, the opposite is the case, given that the SU conserves the dependencies of the mutual information, being merely a normalization thereof.

[2] For further information, see (*Kraskov et al.* [2003])

Mutual Information

Given the random variables S_i as the states of a neuron defined by $s_i(t)$ (see eq. 5.2) and the probability of finding the neuron in such a state $p(s_i)$, the difference between the entropy of one state $H(S_1)$ and the conditional entropy $H(S_1|S_2)$ is called the mutual information $I(S_1, S_2)$:

$$I(S_1, S_2) = H(S_1) - H(S_1|S_2) \tag{5.27}$$

It also can be interpreted as the $Kullback - Leibler$ distance between the joint distribution $p(s_1, s_2)$ and the product of the two marginal distributions $p(s_1) \cdot p(s_2)$

$$MI = \sum_{s_1 \in \{0,1\}} \sum_{s_2 \in \{0,1\}} p(s_1, s_2) \cdot \log \left(\frac{p(s_1, s_2)}{p(s_1) \cdot p(s_2)} \right) \tag{5.28}$$

The MI has all the properties of a metric.

Symmetric Uncertainty

To be able to quantify the statistical dependency of the distributions $p(s_1)$, $p(s_2)$ over a wide range of input parameters, this can be normalized by the entropies $H(S_i)$ to yield the Symmetric Uncertainty $SU(S_1, S_2)$, which represents the desired new measure of synchrony:

$$SU(S_1, S_2) = \frac{2 \cdot I(S_1, S_2)}{H(S_1) + H(S_2)} \tag{5.29}$$

$$SU(S_1, S_2) \in [0, 1] \tag{5.30}$$

An example of the Symmetric Uncertainty measure on a neuron pair are given in figure 5.4
To be able to predict input correlations by using the SU, it is necessary to somehow estimate the duration of the ON-states.

A possible approach can be made by using the theoretical membrane potential statistics that have been derived in chapter 3, yielding very good approximations to the real membrane potential of the neurons.

For spiking neurons, the statistical values of the theoretical membrane potentials are an equally good approximation of the *free membrane potential*, which is the exact membrane potential for subthreshold regimes, but not restricted by a spiking threshold and

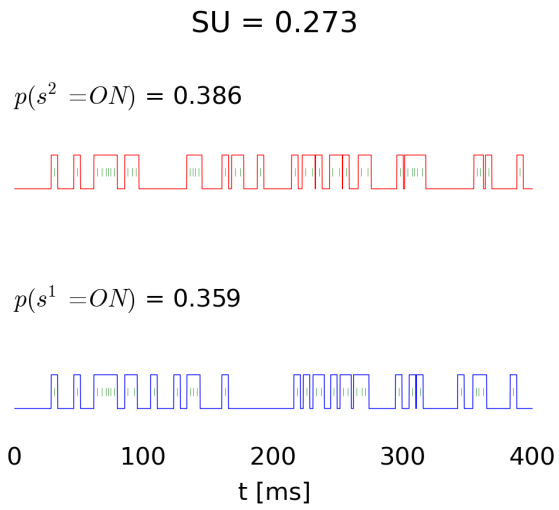

Figure 5.3: ON-states of a neuron pair with 5 shared inputs, and 2 private ones for each neuron.

therefore does not generate output spikes (which would distort the statistical values). In other words, the free membrane potential behaves like the membrane potential for an infinite spiking threshold $V_{thresh} = \infty$.

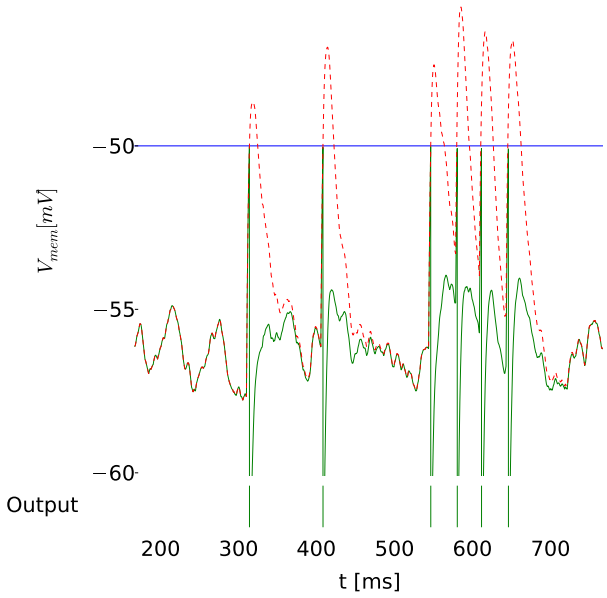

Figure 5.4: Example of the free membrane potential (dashed curve), which behaves like the real membrane potential (solid curve) in the subthreshold regime.

The theoretically derived membrane potential with stereotypical PSPs will henceforth be named the *Load function* $L(t)$, if its role is to approximate the free membrane potential of spiking neurons.

Additionally, it was found out that the amplitude of the Load-function can be approximated by a Gaussian, if the input rates are high enough (section 3.2). This simplifies the theoretical computations of such statistical ON/OFF-states, because the probability density of normal distributions can be treated analytically.

This allows to analytically calculate predictions for ON/OFF-states of neurons without extensive numerical computations:

If the Load function $L(t)$ is normally distributed with the mean μ_L and variance σ_L^2, the probability of a neuron being in an ON-state is

$$p(s_i = 1) = \int_{V_{thr}}^{\infty} \mathcal{N}(\mu_L, \sigma_L^2)\, dx \ , \tag{5.31}$$

with $\mathcal{N}(\mu_L, \sigma_L^2)$ being the probability density of a Gaussian.

The corresponding OFF-state is evaluated in the same fashion,

$$p(s_i = 0) = \int_{-\infty}^{V_{thr}} \mathcal{N}(\mu_L, \sigma_L^2)\, dx \tag{5.32}$$

The same applies to the joint probabilities of spiking states of neurons. To do this, the bivariate gaussian distribution $\mathcal{N}(\mu_{L1}, \sigma_{L1}^2, \mu_{L2}, \sigma_{L2}^2)$ is used, which has been discussed in chapter 4:

If the Load functions $L_1(t)$, $L_2(t)$ of a LIF neuron pair with the means μ_{L_1}, μ_{L_2} and variances $\sigma^2_{L_1}$, $\sigma^2_{L_2}$ are normally distributed, the probability of both neurons being in an ON-state is

$$p^{11} := p(s_1 = 1, s_2 = 1) = \int_{V_{thr}}^{\infty} \int_{V_{thr}}^{\infty} \mathcal{N}(\mu_{L_1}, \sigma^2_{L_1}, \mu_{L_2}, \sigma^2_{L_2})\, d^2x \ . \tag{5.33}$$

The other three states measuring the overlaps of ON/OFF-states of a neuron pair can be expressed analogously:

$$p^{10} := p(s_1 = 1, s_2 = 0) = \int_{V_{thr}}^{\infty} \int_{-\infty}^{V_{thr}} \mathcal{N}(\mu_{L_1}, \sigma^2_{L_1}, \mu_{L_2}, \sigma^2_{L_2})\, d^2x \tag{5.34}$$

$$p^{01} := p(s_1 = 0, s_2 = 1) = \int_{-\infty}^{V_{thr}} \int_{V_{thr}}^{\infty} \mathcal{N}(\mu_{L_1}, \sigma^2_{L_1}, \mu_{L_2}, \sigma^2_{L_2})\, d^2x \tag{5.35}$$

$$p^{00} := p(s_1 = 0, s_2 = 0) = \int_{-\infty}^{V_{thr}} \int_{-\infty}^{V_{thr}} \mathcal{N}(\mu_{L_1}, \sigma^2_{L_1}, \mu_{L_2}, \sigma^2_{L_2})\, d^2x \tag{5.36}$$

$$p^{11} + p^{00} + p^{10} + p^{01} = 1 \tag{5.37}$$

The Symmetric Uncertainty will then be evaluated by plugging these probabilities to equation (5.29)

The crucial idea behind this definition of the probability of ON-states is the ability to predict them theoretically, utilizing the knowledge which has been obtained in the preceding chapters about the theoretical membrane potential (which in this case is the Load-function).

This would imply that it is possible to predict the Symmetric Uncertainty without time-consuming simulations. The next step is now to analyze where such a prediction of correlation is possible and to determine its limitations. To be able to do this, one has to compare the Symmetric Uncertainty resulting from the theoretical ON/OFF-states to ON/OFF-states of a spiking neuron pair of a simulation.

The role of the introduced parameter t_{ON} is a critical component to this, as it will be used to compare the theoretical SU with the one retrieved from the simulation.

Theor. ON-state		Sim. ON-state
Load above threshold	$\longleftrightarrow$	Neuron in spiking state with minimum length t_{ON}
$\hookrightarrow SU_L$		$SU_{t_{ON}} \hookleftarrow$

5.2 ON-States of Simulated Spiking Neuron Pairs

Before the analysis of the theoretical prediction of such ON-states can begin, the still undefined minimal ON-state t_{ON} needs to be defined, as it is vital to know the impact of different t_{ON} on the prediction.

Not only the length of t_{ON}, but also the centering of the ON-state relative to the occurence of the action potential has to be addressed. The rise of the membrane potential due to an excitatory PSP compared to its fall resulting from the relaxation is short compared to the time the Load function is above threshold. In fact, the higher the conductance of the membrane, the faster the membrane reacts to any synaptic input.

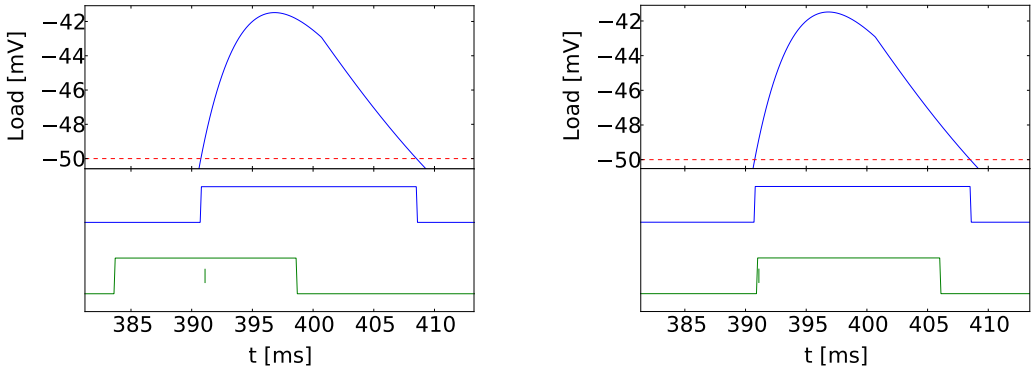

(a) ON-state centering the output spike

(b) ON-state begins 0.1 ms after output spike

Figure 5.5: Input spike with high synaptic weight $w = 0.04$ μS, triggering a single output spike. The blue ON-state defined by the crossing of the threshold at -50 mV starts almost immediately before the generation of the action potential. Left figure shows the green ON-state centered around the output spike, which results in a bad overlap. In the right picture, the ON-state in the simulation is activated 0.1 ms after the output is generated - this yields a better overlap and thereby approximation of the ON-states.

In case of burst spiking without inhibition, the extraordinary height ($w_{exc} > 10^{-2}$ μS) of the synaptic weights makes it possible to trigger even more than one output spike before the free membrane potential relaxes below the spiking threshold at -50 mV. The rise

of the membrane potential towards the spiking threshold is very fast ($\approx$ 1 ms), which means that the ON-state triggered by the output realistically begins when the Load function is at the threshold, as shown in fig. 5.5. Therefore, it is a valid approximation to start the ON-state at the time of the output spike occurence.

5.2.1 Fixing the ON-State Length for Simulated Neuron Pairs

Determining the length of t_{ON} is not as simple. First of all, it is necessary to check if the structures of the joint probabilities p_{10} p_{11}, p_{00}, p_{10} show dependencies on this parameter. In order to find this out, simulations for a conductance-based LIF neuron pair were performed, iterating over reasonable values of t_{ON}, and varying input rates and weights ν_{exc}, w_{exc}, the stimulation being equal for both neurons.

Parameter space:

$$t_{ON} \in \{10 \text{ ms}, 15 \text{ ms}, 20 \text{ ms}, 25 \text{ ms}\}$$
$$w_{exc} \in [15 \cdot 10^{-3}\mu\text{S}, 50 \cdot 10^{-3}\mu\text{S}\ ]$$
$$\nu_{exc} \in [100 \text{ Hz}, 300 \text{ Hz}]$$

These input parameter regions include neuron states where frequent burst spiking occurs (high w_{exc}, low ν_{exc}), and also regions where membrane potentials fluctuate in the proximity of the threshold, triggering output spikes in lower frequency (low w_{exc}, high ν_{exc}).

The results of these iterations for the probabilities p_{11} and p_{00} can be seen in fig. 5.6, and the ones for p_{10} in fig. 5.8:

- While the values of the p_{11}- and p_{00}-hypersurfaces in the parameter space depend on t_{ON}, their monotonicity properties are the same. The differences between the planes for different t_{ON} are merely monotonic transformations. These are of course expected, because the larger t_{ON} becomes, the larger p_{11} becomes, and inversely p_{00}. However, it is apparent that there are no fundamental differences of p_{11}-hypersurfaces with differing t_{ON}.

  Indeed, the color plots of the theoretical structures of such color plots in 5.7 show a very similar pattern and impact of ν_{exc} and w_{exc} on the probabilities.

- The p_{10}-hypersurfaces[3], in fig. 5.8 differ for increasing t_{ON}. Again, the impact of ν_{exc} and w_{exc} on the p_{10}-hypersurface is symmetrical, which can be seen as a

[3]The probability hypersurfaces of p_{01} are not shown, because for sufficiently long time periods, $p_{10} \approx p_{01}$ for equal excitatory stimulation in both neurons.

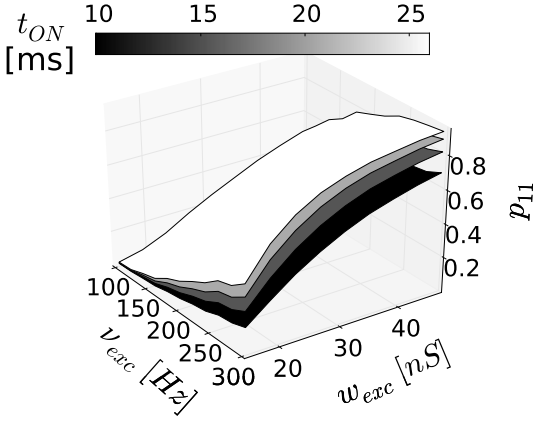

(a) p_{11} for $t_{ON} \in \{10, 15, 20, 25\}$

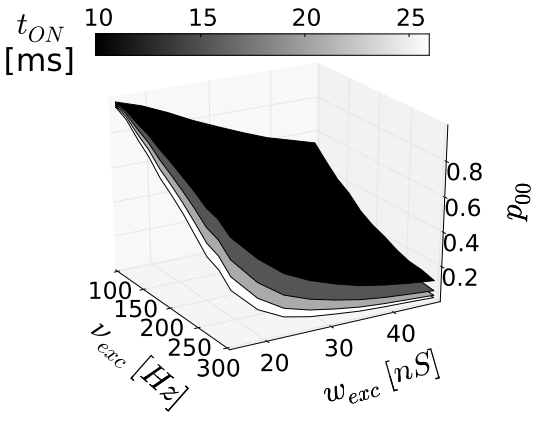

(b) p_{00} for $t_{ON} \in \{10, 15, 20, 25\}$

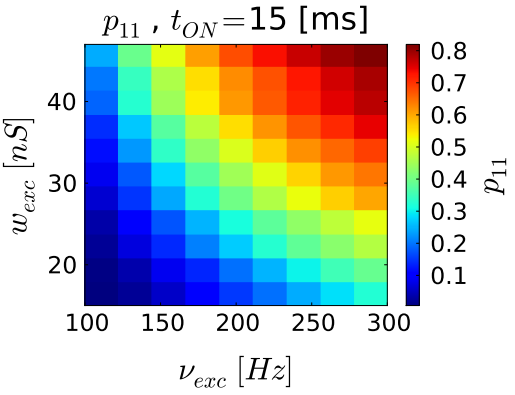

(c) Color plot for $t_{ON} = 15$ ms

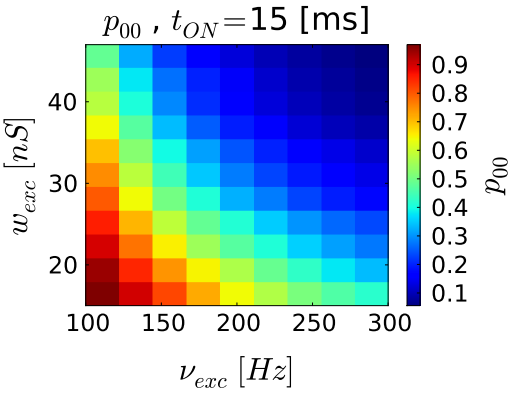

(d) Color plot for $t_{ON} = 15$ ms

Figure 5.6: Figures 5.6a and 5.6b show hypersurfaces of probabilities p^{11} and p^{00} for different t_{ON} in the parameter space of w_{exc} and ν_{exc}. It can be seen that the general behavior on all four hypersurfaces is the same. Surfaces of higher t_{ON} values are shifted up systematically for p^{11}, and down systematically for p^{00}. This is expected intuitively. Figures 5.6c and 5.6d show the symmetrical structure of one such hypersurfaces, $t_{ON} = 15$ ms. It can be seen that both w_{exc} and ν_{exc} affect the state probabilities.

consequence of the symmetry in the p_{11}- and p_{00}-hypersurfaces with the sum of all probabilities being 1. Overall, even here, the comparison with the theoretical p_{10}-hypersurface shows good agreement.

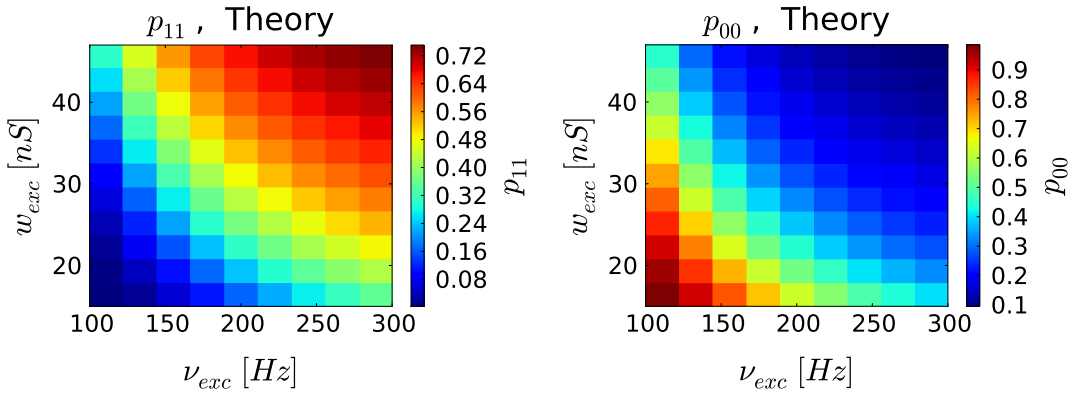

(a) Color plot for theoretical p^{11}

(b) Color plot for theoretical p^{00}

Figure 5.7: Figures 5.6a and 5.6b show the theoretical hypersurfaces of probabilities p_{11} and p_{00} in the same w_{exc} and ν_{exc} parameter space as the probabilities of the simulated ON-states in fig. 5.6. The hypersurfaces show the same properties as the ones in fig. 5.6.

At this point, the results indicate that there are different possible parameters t_{ON} that can be used to analyze the prediction capabilities of the SU measure for correlated inputs with different configurations of shared inputs.

Before making an extensive parameter sweep for both the current-based and conductance-based[4] LIF neuron pairs, it is necessary to determine a t_{ON} parameter which suits most of the relevant regions of all probabilities.

The most important condition which must be fulfilled, is

$$p_1^{sim} = p_1^{th} \ . \tag{5.38}$$

This condition demands that for the input parameter space, the total probability of a neuron being in a spiking state must be close for the theoretical and the ON-states from the simulation, triggered by output spiking.

The probabilities from the simulations of the parameter sweep for the conductance-based LIF model will be compared to the theoretical values by computing the relative error

$$Err = \frac{p_1^{sim} - p_1^{th}}{p_1^{th}} \ . \tag{5.39}$$

[4] in the high conductance approximation, as derived in section 3.1.5

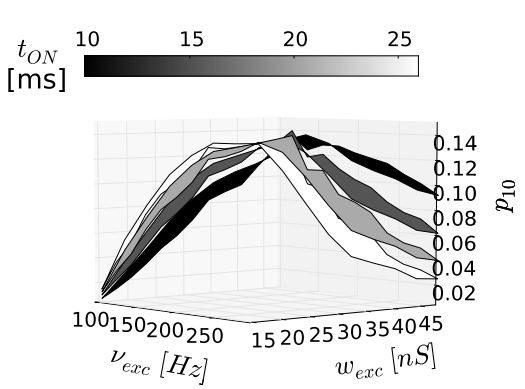

(a) p_{10} for $t_{ON} \in \{10, 15, 20, 25\}$

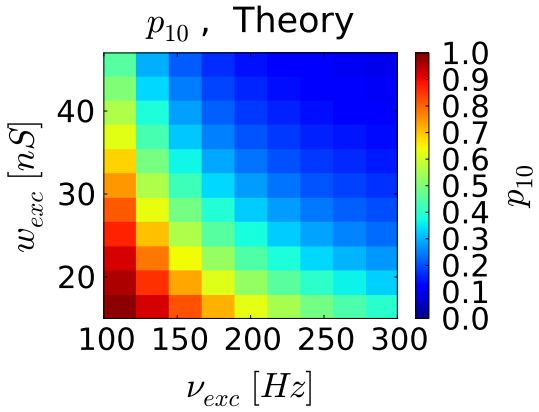

(b) Color plot for theoretical p_{10}

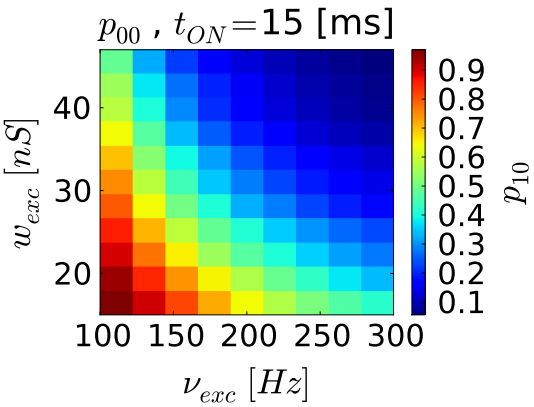

(c) Color plot for $t_{ON} = 15$ ms

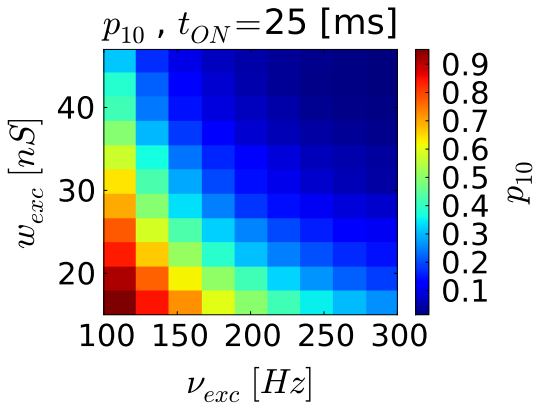

(d) Color plot for $t_{ON} = 25$ ms

Figure 5.8: Figure 5.8a shows the hypersurfaces for different parameters of t_{ON}. It is noteable that the transformation of the hypersurfaces is not monotonic, in contrast to the probabilities in 5.6a and 5.6b. Figures 5.8c and 5.8d show the color plots of the probabilities for $t_{ON} = 15$ ms and $t_{ON} = 25$ ms, respectively. Overall, for both t_{ON} values, the color plots have the same structure as the theoretical one from 5.8b. Remarkably, the influences of increasing w_{exc} and ν_{exc} are practically the same.

As figure 5.9 shows, the parameter value $t_{ON} = 15$ ms induces the lowest relative error and therefore will be the value of choice. In the next section, it will be used to generate the ON-states in simulation, and making it possible to compare the Symmetric Uncertainty with the Symmetric Uncertainty utilizing theoretical ON-states.

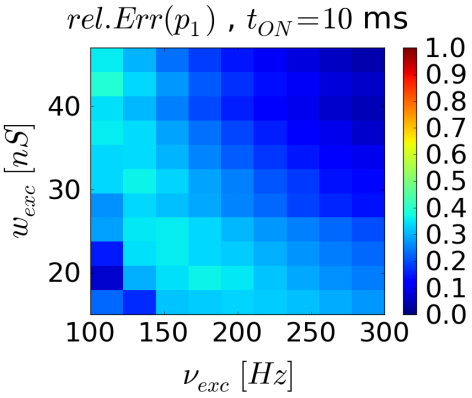

(a) Err for $t_{ON} = 10$ ms

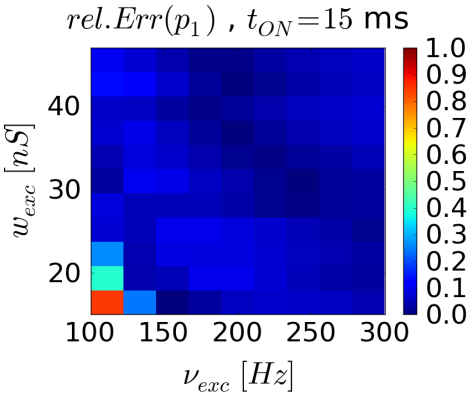

(b) Err for $t_{ON} = 15$ ms

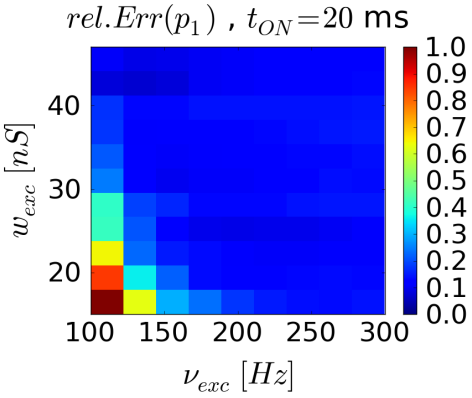

(c) relative error for $t_{ON} = 20$ ms

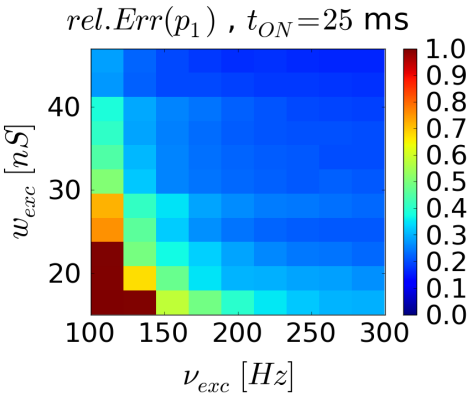

(d) relative error for $t_{ON} = 25$ ms

Figure 5.9: The figures show the relative errors based on eq. (5.39) for simulations with constant w_{inh} and ν_{inh}. The best overall agreement for all parameter regions can be found in fig. 5.9b, although it has a very high relative error for very low excitation. This heavily decreased excitation leads to a lack of output spikes, which is visible in all four color plots.

5.3 Predicting Correlated Input Configurations

Finally, the quality of the prediction of the Symmetric Uncertainty measure will be tested. The goal of this section is to evaluate three quantities regarding the Symmetric Uncertainty measure:

- SU_{th} / $SU_{\mathcal{N}}$: the predicted SU measure, which is the result of integrating the assumed bivariate normal distribution of the Load-function, as described on p. 86
- SU_{load}: the SU measure which will be evaluated from the numeric simulation of

the Load-function:

$$L(t) > V_{thresh} \Rightarrow ON - state$$

- SU_{sim}: the SU measure as a result from the ON/OFF-states of output spiking of the LIF neuron pair with a minimal ON-state of $t_{ON} = 15$ ms, as mentioned in the previous section.

This simulation setup will be performed for the following synaptic configuration of shared and private channels:

- Overall, there will be 100 available channels $ch = 100$
- The total synaptic input rates will be ν_{exc}, ν_{inh}, distributed equally over all channels for each LIF neuron:
  $\nu_{syn}^{chan} = \frac{\nu_{syn}}{ch}$
- The occuring input spikes will be weighted with synaptic weights w_{syn} for the conductance-based LIF neuron.
- The shared channels will be increased, also increasing the shared shared synaptic rates, therefore increasing the correlation of spiking phases of the neuron pair.

The total input parameters of this extensive simulations, are

Parameter spaces

$$t_{ON} = 15 \text{ ms}$$

Synaptic input rates

$$\nu_{exc}, \nu_{inh} \in [10 \text{ Hz}, 250 \text{ Hz}]$$

High-conductance-based synaptic weights:

$$w_{exc},\ w_{inh} \in [20 \text{ nS}, 45 \text{ nS}]$$

These parameter spaces require some explanation. The inhibitory rates are also taken into account this time, to make assumptions about the impact of inhibition of the spiking states.

The ranges for inhibitory and excitatory weights are different:
For the conductance-based model, equal weights lead to dominant excitation, as the excitatory PSPs have higher amplitudes in this case. To prevent constant ON-states, the range of inhibitory weights has to be set higher than the one for excitation.
These paramter ranges lead to a variety of spiking behaviors of both neurons, which can be classified roughly into two characteristic behaviors:

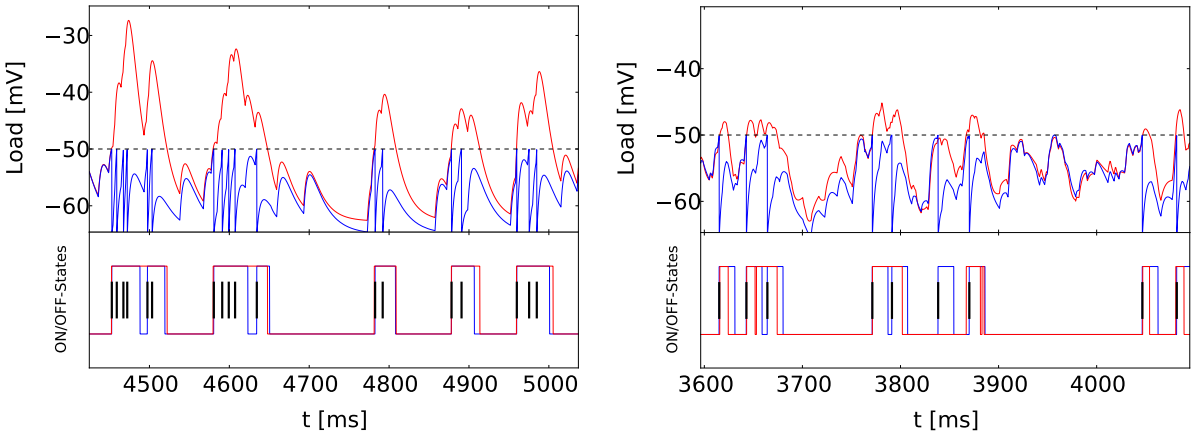

(a) Low synaptic rates, high weights

(b) High synaptic rates, low weights

Figure 5.10: Both figures show different classes of ON-states of a conductance-based LIF neuron. In 5.10a, the excitatory rate, at $\nu_{exc} = 50$ Hz is low, but triggers large PSPs due to a high synaptic weight $w_{exc} = 45$ nS. The Load-function is well above threshold due to multiple output spikes, initiating long ON-states. A fundamentally different behavior is shown in fig. 5.10b, where comparably high synaptic rates $\nu_{exc} = 210$ Hz, $\nu_{inh} = 170$ Hz trigger irregular ON-states due to small-amplitude fluctuations of the membrane potential.

- Long ON-states due to output spike bursts, caused by a low excitatory rate ν_{exc}, but very high excitatory weights/currents. The resulting output spiking patterns can be seen in fig. 5.10a.
- Varying ON-state lengths resulting from membrane potential fluctuations induced by high-frequent PSP generation. This behavior is shown in fig. 5.10b.

Before comparing the results of different shared input rates, the basic properties of the predicted Symmetric Uncertainty SU_{th} will be explained. As stated before, it assumes a normally distributed Load-function and is computed by means of the predicted ON/OFF-states p_1, p_0, p_{11}, p_{00}, p_{10}, p_{01}, as described on p. 86.

The impact of increasing shared rates is an increase in the SU_{th}, which is expected, as this is equivalent to an increase in correlated input.

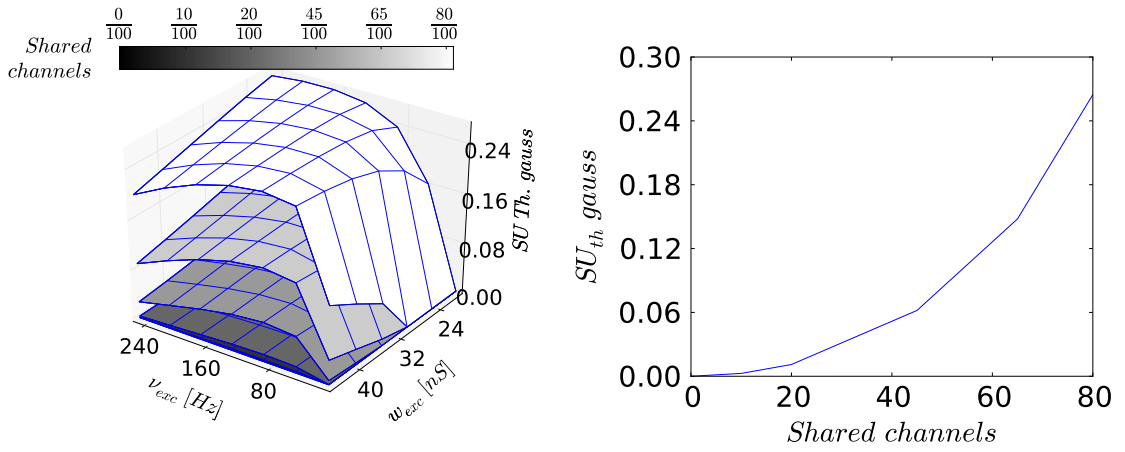

(a) SU_{th} for $w_{inh} = 0.035$ μS, $\nu_{inh} = 50$ Hz

(b) SU_{th} for different shared channels, $w_{inh} = 0.035$ μS, $\nu_{inh} = 50$ Hz, $\nu_{exc} = 90$ Hz, $w_{exc} = 0.03$ μS

Figure 5.11: Figure 5.11a shows differently colored SU values for increasing shared input rates. As the number of shared channels increases, the SU_{th} hypersurfaces change, albeit keeping the general shape. It shows that an increase in ν_{exc} has more impact on the SU than w_{exc}. This of course also applies to the current-based SU, which is not shown here. Fig. 5.11b illustrates the evolution of the SU in the (SU, no. of shared channels) hypersurface, showing the rising increase of SU_{th}, dependent on the shared input rates. The similar shape for all hypersurfaces justifies analysing only one of them to show the impact of variation of input parameters.

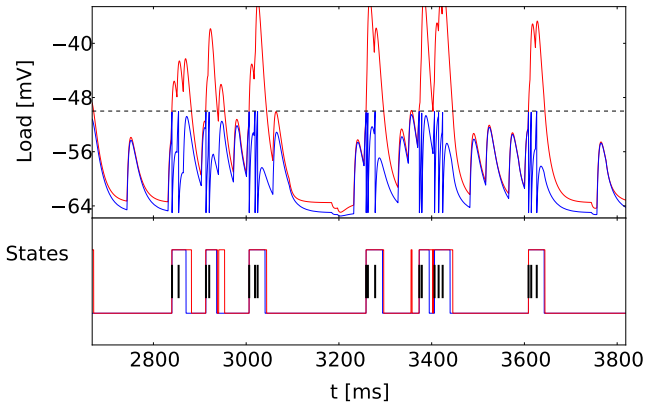

(a) Load-function trace and states for $L(t) > V_{tresh}$ and output spikings

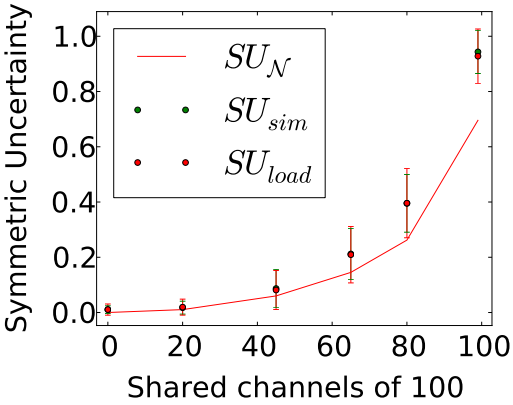

(b) SU for variation in shared channels

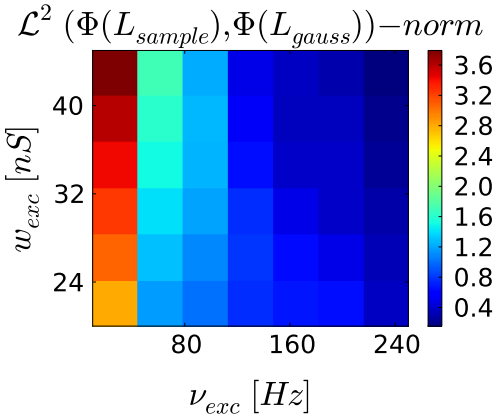

(c) $\mathcal{L}^2 - norm$ of difference of $\Phi(L)$ to Gaussian

Figure 5.12: Figure 5.12a shows a Load-function trace (red curve) and membrane potential (blue curve) for high excitatory weights $w_{exc} = 0.05$ μS) and low synaptic rates ($\nu_{exc} = 20$ Hz, $\nu_{inh} = 10$ Hz. The agreement between the states of the ON-states generated by output spiking (blue states) correspond very well to the ON-states triggered by $L(t) > V_{thresh}$ (red states). The same parameters were used to compare SU_{sim} and SU_{load} to $SU_{\mathcal{N}}$ in fig. 5.12b for rising number of shared channels, out of 100 total channels. It is clear that the agreement between SU_{sim} and SU_{load} is very good, as indicated by the ON-states in fig. 5.12a, but $SU_{\mathcal{N}}$ is systematically lower, which becomes clear for increasing shared channel numbers. The reason for this can be seen in fig. 5.12c, where the L^2-norm of the difference of the Load-amplitude distribution and a theoretical Gaussian is plotted, as given in eq. (5.40). The L^2-norm increases drastically for high w_{exc} and low ν_{exc}, implying that the assumption of a normal distributed Load-function can not be held with low input rates. This is also shown in chapter 3, section 3.2.

SU for low ν_{exc}, high w_{exc}

This input parameter region, as illustrated in 5.10a, leads to generation of output spikes due to high excitatory weights large PSPs.

In fig. 5.12, the Symmetric Uncertainty is evaluated for such regions in the conductance-based LIF model. The three different SU results are shown, with visible deviations of SU_{sim}, SU_{load} to SU_{th}.

The cause of this deviation can be explained - in this case - by the difference between the cumulative density function (cdf) of the Load-amplitude-distribution, and a theoretical cdf of a Gaussian[5]:

$$L^2(L_{sample}, L_{gauss}) = \int_{-\infty}^{\infty} \left[\Phi(L)_{sample}(x) - \Phi(L)_{gauss}(x)\right]^2 \, dx \tag{5.40}$$

For low input rates, as is the case in fig. 5.12, the Load-function can not be approximated by a normal distribution. This problem has been discussed for the subthreshold membrane potential in chapter 3.

Figures 5.12 indicates that the region of low synaptic input rates can not be estimated by $SU_{\mathcal{N}}$, whereas the values of SU_{sim} and SU_{load} show a good agreement.

For higher input rates, the normal distribution of the Load-function amplitude distribution is well approximated by a Gaussian, as has been shown in chapter 3, section 3.2. This leads directly to the second parameter region in which the Symmetric Uncertainty will be analyzed:

SU *for high* ν_{exc}, *low* w_{exc}

In these regions, SU_{sim} and $SU_{\mathcal{N}}$ will be compared, neglecting SU_{load}, which converges to the theoretical Symmetric Uncertainty.

To avoid constantly spiking neurons due to high excitation, the inhibitory input rates will also be chosen high. Both these high input rates guarantee a normally distributed Load-function, as already discussed. A typical simulation trace can be seen in fig. 5.13a.

The comparison of the Symmetric Uncertainty in such regions can be seen in fig. 5.17, where critical deviations between the theoretical and simulation values can be identified with the relative error.

[5] This concept has been already discussed on p. 54

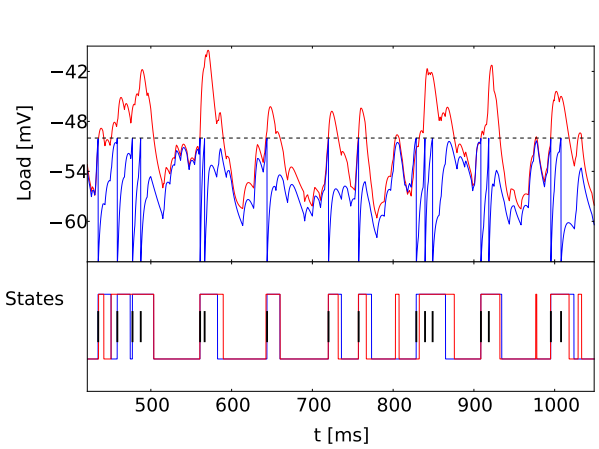

(a) Load-function (red), membrane potential and states for $L(t) > V_{tresh}$ and output spiking

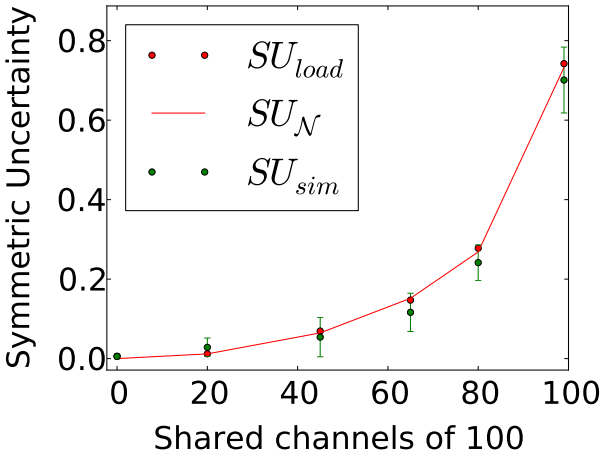

(b) SU-channel plot

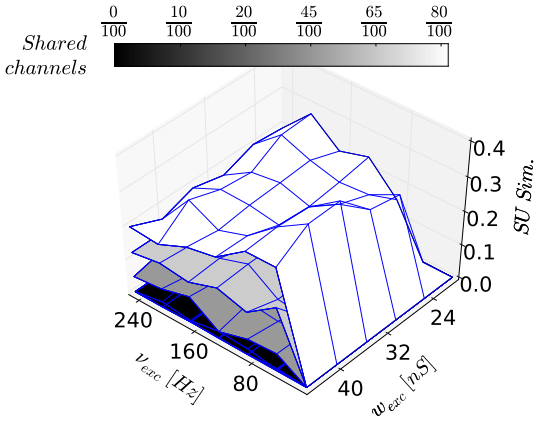

(c) SU_{sim} for high inhibitory input

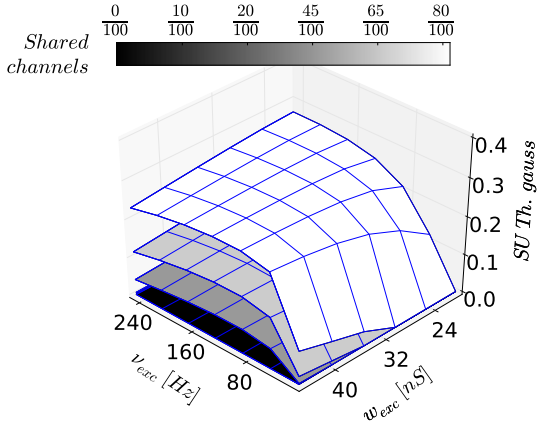

(d) SU_{th} for high inhibitory input

Figure 5.13: A typical simulated Load-function and membrane potential trace for high ν_{exc} and low w_{exc} can be seen in 5.13a. Due to the high input rates, the membrane potential (and therefore the Load-function) fluctuates. This leads to big differences in the lengths of ON-states if $L(t) > V_{thresh}$ (blue states). Because the output spike-triggered ON-states (red states) show minimum lengths of $t_{ON} = 15$ ms, deviations between both states occur. This, in turn, leads to deviations of the Symmetric Uncertainties.
For the whole parameter region, SU_{sim} and $SU_{th} = SU_{\mathcal{N}}$ are shown in 5.13c and 5.13d. A relatively high inhibitory input rate of $\nu_{inh} = 170$ Hz and low weight $w_{inh} = 0.02$ μS ensures that the amplitude distribution of the Load-function can be approximated as a Gaussian, as opposed to the Load-functions from 5.12. Yet, the hypersurfaces of SU_{sim} from 5.13c show visible deviations from the SU_{th} values in 5.13d. Although only the hypersurface of 80 of 100 shared channels can be seen completely on the plots, this applies to all configurations of shared channels, as can be seen in fig. 5.15, where the relative error is shown.

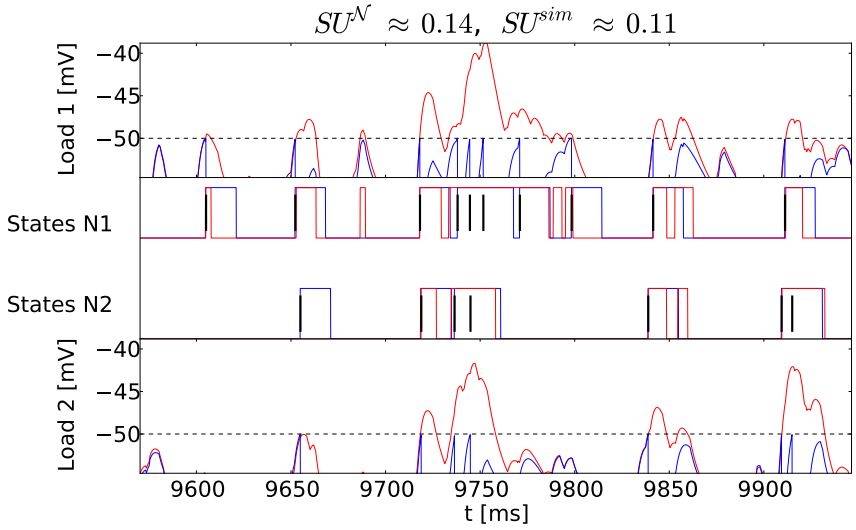

(a) Simulated states with high ν_{exc} and ν_{inh}

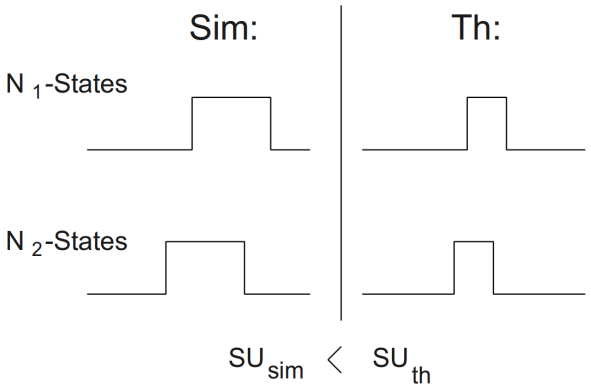

(b) SU_{th} and SU_{sim} for increase of shared channels

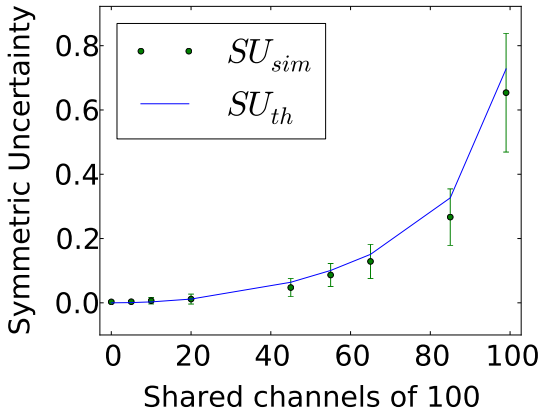

(c) $SU_{sim} < SU_{th}$

Figure 5.14: The simulation with $\nu_{exc} = 170$ Hz, $\nu_{inh} = 170$ Hz shows suboptimal overlap between the output spike-triggered ON-states (red) and the states activated by the Load-function (blue). In simulations with high input rates, the derived states are often longer than the ones derived in theory. This is illustrated in fig. 5.14b. This results in $p^{10}_{sim} > p^{10}_{th}$. This results in systematically lower SU_{sim}, which can be computed easily. Note that increasing the ON-state length t_{ON} would distort the other probabilities p^{11}_{sim}, p^{00}_{sim}.

The actual probabilities contributing to the Symmetric Uncertainty show the same behavior for varying input parameters, for one specific configuration of shared channels. This has also been shown in the previous section, in 5.7 and 5.8.

Two very important can be drawn from the analysis of figures 5.12, 5.13, 5.17:

- In fig. 5.12, the systematic errors in low-frequency ranges between SU_{th} and SU_{sim} can be attributed to the fact that the distribution of the Load-amplitudes can not be approximated as Gaussian. For these synaptic rate parameters, the Symmetric Uncertainty can not be reliably predicted.
- For higher input rates, therefore justifying a normal distribution of the Load-function, fig. 5.13 shows highly fluctuating SU_{sim}. This is a sign of statistical deviations, which is solidified by the direct comparison of both Symmetric Uncertainties in fig. 5.17.
- Indications in fig. 5.17 suggest that, even for high simulation times, systematic errors occur for high input rates, although the Load-function can be approximated by a normal distribution.

These points suggest that SU_{sim} is heavily susceptible to statistical errors of the probabilities, but also systematic errors. Both classes of errors will be explained in the next section.

5.4 Deviations of the Symmetric Uncertainty Measure

The previous section has exposed particular problems in the evaluation of the Symmetric Uncertainty:

- SU_{sim} is susceptible to statistical fluctuation of the probabilities.
- For long simulation times, with a minimum of statistical errors, systematic errors of SU_{sim} also can be seen.

Systematic Deviations:

As pointed out in fig. 5.13, the major difference between the ON-states triggered by output spikes and the Load-function being above V_{thresh}, is that in simulation, a minimum ON-state is triggered when output spiking occurs.

The higher the input rates, the more fluctuation shows the Load-function. In general, this leads to less overlap of the ON-states activated by the Load-function with the ON-states triggered by output spikes, as can be seen in fig. 5.14.
The cause of this problem is the fixed length of t_{ON}, which makes it impossible to overlap the variable lengths of the ON-states triggered by the Load-function with only

one fixed length. This problem exists for all fixed time lengths and explains the limits of the Symmetric Uncertainty to detect correlated spiking states.

However, it is difficult to implement ON-states that are not fixed states and overlap with the Load-function if stimulated with high input rates, as output spike timings vary heavily and do not always coincide with the ON-states given by the Load-function. Even minor discrepancy can lead to a major contribution to the systematic error of the Symmetric Uncertainty.

Statistical Deviations:

In addition to the discussed errors above, statistical errors of the probabilities are part of the uncertainty propagation of SU_{sim}. To evaluate an estimation of the total statistical error of the Symmetric Uncertainty, it is helpful to alter the notation slightly:

$$SU = \sum_{i,j\in\{0,1\}} p^{i,j} \cdot \log\left(\frac{p^{i,j}}{p_1^i \cdot p_2^j}\right) \qquad =: SU^{11} + SU^{00} + SU^{11} + SU^{10} \tag{5.41}$$

$$= \sum_{i,j\in\{1,0\}} SU^{i,j} \tag{5.42}$$

The true source of statistical errors are the probabilities which contribute to SU_{sim}. The probabilities p_1^1, p_2^1, p^{11}, p^{10}, p^{01} can be regarded as independent, because the rest of the probabilities can be derived with the knowledge of the mentioned:

- Single OFF-states of neurons 1, 2: p_1^0, p_2^0
- OFF-state of both neurons p^{00}:

$$p^{10} + p^{01} + p^{11} + p^{00} = 1$$

These relations can be used to derive the total result of the propagation of statistical uncertainty:

$$\Delta SU_{sim} = \sqrt{\sum_{i\in\{1,2\}} \left(\frac{\partial SU_{sim}}{\partial p_i^1} \cdot \Delta p_i^1\right)^2 + \sum_{j\in\{11,10,01\}} \left(\frac{\partial SU_{sim}}{\partial p^j} \cdot \Delta p^j\right)^2} \tag{5.43}$$

Using the notation from eq. 5.42, the partial derivatives for all above probabilities are

$$\left.\frac{\partial SU^{ij}}{\partial p_k^1}\right|_{i,j\in\{1,0\},\ k\in\{1,2\}} = A \cdot D(ij) \log\left(\frac{p^{ij}}{p_k^1}\right) \ , \tag{5.44}$$

$$\text{with } A = \log_2(e) \tag{5.45}$$

and

$$D(ij) = \begin{cases} -1 & \text{if } i = j = 0 \\ 1 & \text{else} \end{cases} \tag{5.46}$$

and also

$$\frac{\partial SU^{ij}}{\partial p^{km}} = D(km) \cdot A \cdot \left[\log\left(\frac{p^{km}}{p_1^1 \cdot p_2^1} \right) + D(km) \right] \tag{5.47}$$

$$\tag{5.48}$$

Due to the proportionality given in the above equations, the terms $\frac{\partial SU^{11}}{\partial p^{11}}$, $\frac{\partial SU^{10}}{\partial p^{10}}$, $\frac{\partial SU^{01}}{\partial p^{01}}$ and $\frac{\partial SU^{00}}{\partial p^{ij}}$ grow approximately logarithmically. Because $p^{00} = p^{11} - p^{10} - p^{01}$, the probabilities of one neuron spiking and the other not, are included in almost every term, contributing significantly to the error propagation.

The total statistical error of the Symmetric Uncertainty, including all of the above terms, can become very large. As an example, a typical uncertainty of $\Delta p_k \approx 10\%$ for the probabilities of SU_{sim} (as has been shown in the previous section, in particular[6] in fig. 5.13), $\Delta SU_{sim} \approx 0.08$, which is about 35% of the theoretical value $SU_{\mathcal{N}} = 0.23$.

Lowering the input rates is the only way to decrease this error. Unfortunately, such an increase would lead to a Load function amplitude distribution which is not a Gaussian, as already seen in fig. 5.12.

[6] with $w_{exc} = 0.03$ μS, $w_{inh} = 0.02$ μS, $\nu_{exc} = \nu_{inh} = 170$ Hz, for 80 shared channels

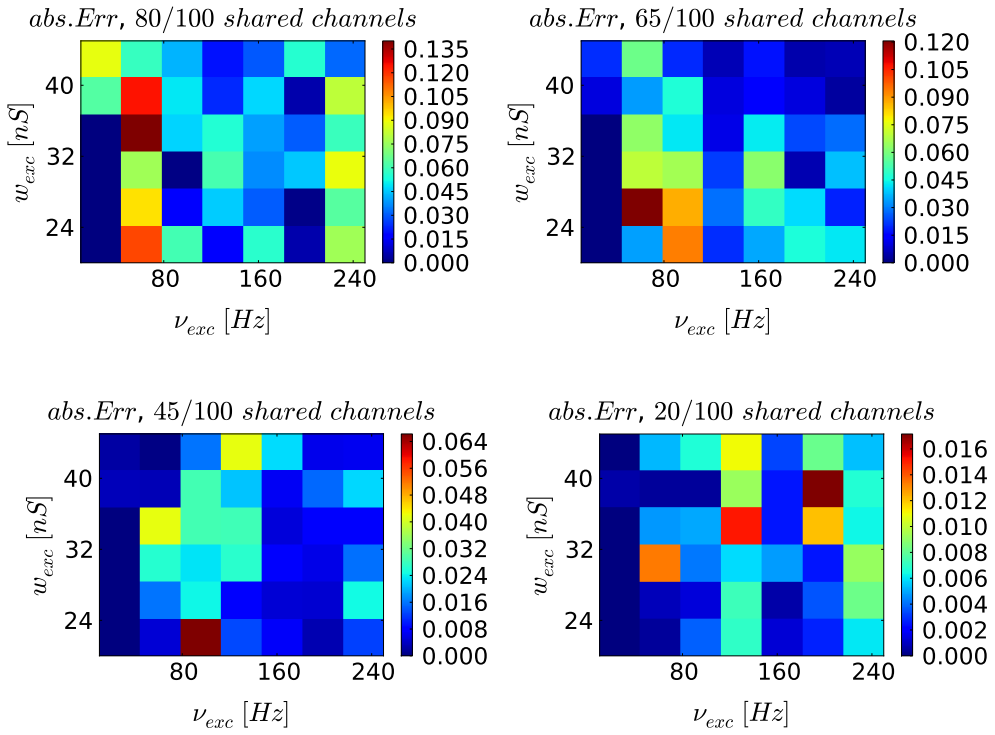

Figure 5.15: All color plots have been taken from the simulation results of fig. 5.13, with the absolute error between SU_{th} and SU_{sim}. The figures show that increasing shared inputs decrease the deviation between both SU_{th} and SU_{sim}. In all four plots, there are regions with relatively high deviations, but most values (blue) show deviations below 15%, which is a satisfactory result.

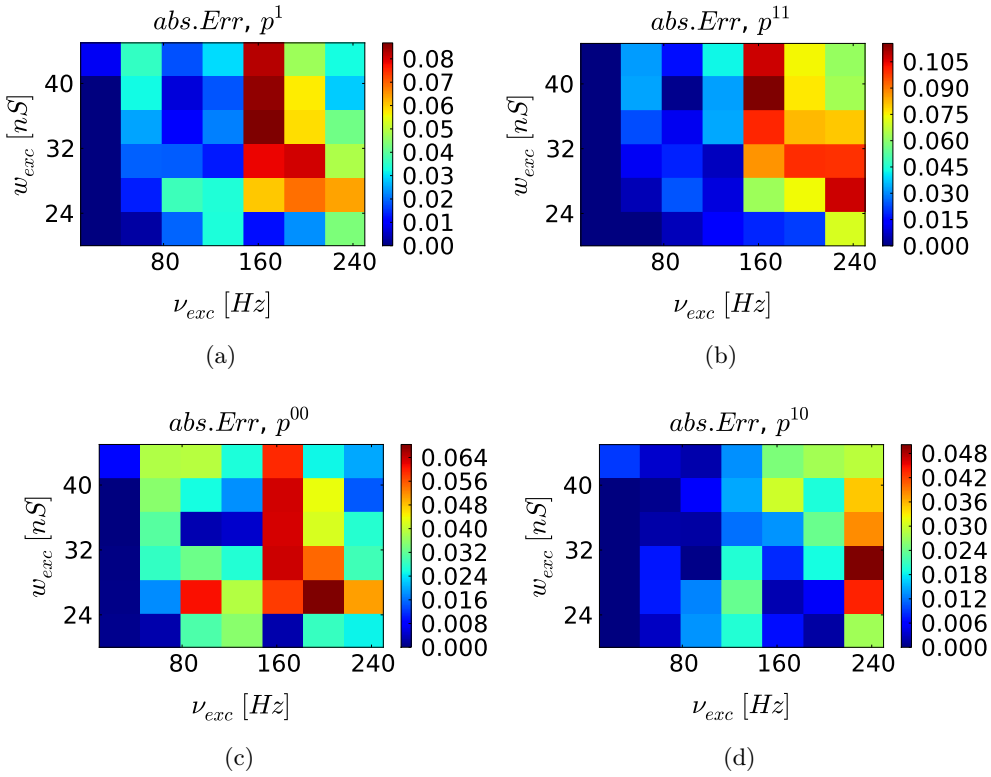

Figure 5.16: The color plots, based on simulations with high synaptic input, show the absolute errors between the probabilities resulting from the simulations and the ones derived theoretically for 65/100 shared channels. All error margins are very low for all four probabilities. Even the maximum absolute error for p^{11} in fig. 5.16b is slightly under 11%. The prediction of these states shows very good results.

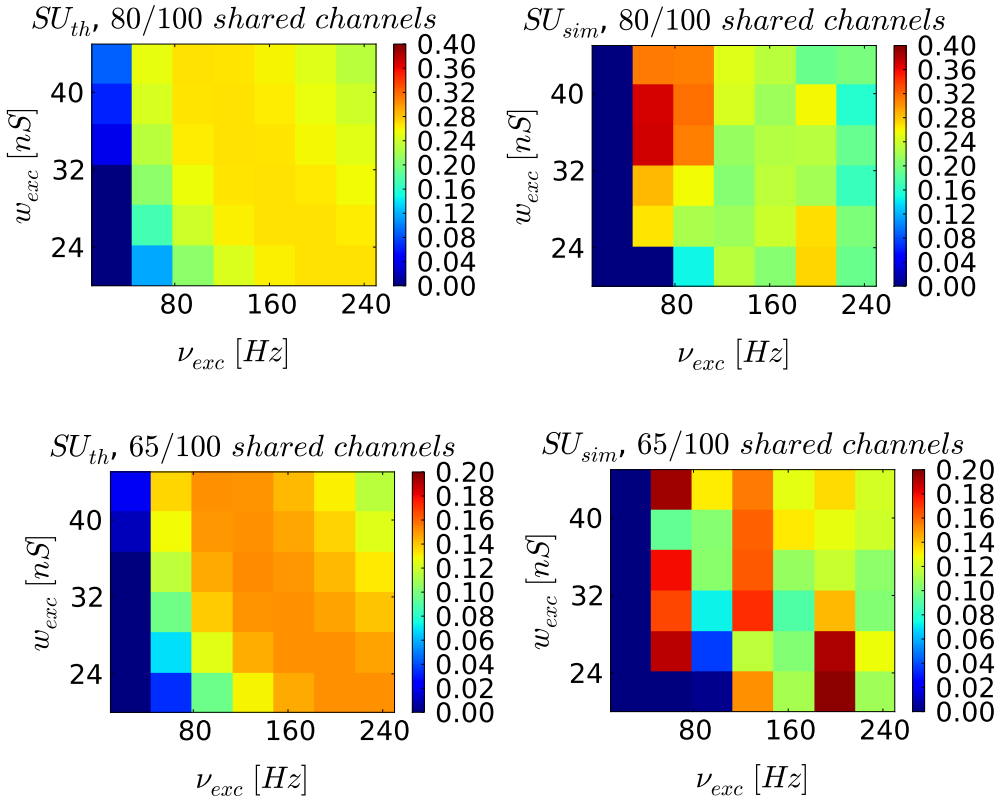

Figure 5.17: The color plots show a general comparison between SU_{th} and SU_{sim}, taken from the simulations from 5.13, where a constant high excitation is also applied. The upper color plots 5.17a and 5.17b show a comparison of a configuration with 80 shared channels. Considering the large stochastic errors (which are estimated in section 5.4), both SU measures show a similar trend. For low w_{exc} and ν_{exc}, $SU_{th} = SU_{sim} = 0$, which is a consequence of very long OFF-states due to a lack of output spikes. For higher ν_{exc}, the SU_{th} grows slowly, increasing symmetrically with rising w_{exc} and ν_{exc}. The simulated results show systematically lower SU_{sim}, with patches of very high SU_{sim}. A similar trend can be seen on the lower color plots, for SU_{th} in 5.17c and SU_{sim} in 5.17d, for a configuration of 65 shared channels. There, one can see random high values and systematic deviations with $SU_{th} > SU_{sim}$.

6 Conclusion & Outlook

In this chapter, the results from the previous chapters will be briefly summarized, and will motivate further research based on the obtained results in this thesis.

LIF neuron dynamics

Before attempting to define any measure of correlations, thorough analysis and understanding of neuron membrane dynamics is required. Chapter 2 starts with electrophysiological properties of neurons and eventually the differential equations for the current- and conductance-based Leaky Integrate and Fire neuron.

In chapter 3, the Leaky Integrator differential equation was used to predict the neural dynamics of a current- and conductance-based LIF neuron. This equation, for the case of presynaptic input, could be solved analytically for the current-based LIF neuron in section 3.1.1, yielding a closed-form expression for the PSPs. An equivalent for the conductance-based LIF neuron was found for the high conductance state.

When the requirements for this approximation are not met, the prediction exhibits deviations from the simulated membrane potential trace. An important factor which affects the quality of this theoretical prediction is the proximity of the membrane potential to the inhibitory reversal potential.

In a subsequent step, the mean and variance of the membrane potential distributions have been derived. Based on the solution of the PSP membrane potential, the calculation of these quantities was conducted in section 3.1.6 for both LIF neuron models. The obtained results are summarized on p. 45.

The systematic deviations of the mean and variance of the conductance-based membrane potentials to the ones from the simulated membrane potentials were investigated in section 3.1.7 for an extensive range of synaptic input parameters. Overall, the results for the prediction of both the mean and variance of the conductance-based membrane potential were very good, although the expected systematic deviations in the regime of high inhibition were confirmed. For the current-based LIF neuron, the agreement was perfect, as its differential equation was solved analytically.

To extend the valuable knowledge about the statistics of the membrane potential, especially for the hardware-relevant conductance-based LIF neuron, the nature of the

membrane potential amplitude distribution was analyzed in section 3.2.

By means of the Central Limit Theorem in section 3.2.1, it was argued that the membrane potential distribution can be approximated by a Gaussian for sufficiently high synaptic Poisson-input rates. This argument was underpinned through extensive software simulations.
The essential achievements of these chapters are

- the theoretical derivation of the mean and variance for the current- and conductance-based membrane potential, and
- the confirmation that membrane potential distribution can be approximated as a Gaussian for the studied input regimes.

Quantifying correlated membrane potential fluctuations

In chapter 4, the concept of correlated input was introduced. Based on the results from the previous chapter, the membrane potential distribution of a LIF neuron will be approximated by a Gaussian. Therefore, in section 4.1, the membrane potential distributions of a pair of LIF neurons has been described as a bivariate Gaussian.

This bivariate Gaussian is completely described by the two means and variances of the neuron pair (as derived in the previous chapter), and the correlation coefficient. This correlation coefficient, naturally embedded in the bivariate Gaussian, has been chosen as the measure of correlated membrane potential fluctuations resulting from shared input channels. In section 4.1.1, this quantity is derived as a function of synaptic input parameters and the number of shared channels by using the statistical framework from chapter 3.

The results for the current- and conductance-based LIF neuron, summarized on p. 69, were used to predict the correlation coefficient in section 4.2.

The prediction yielded very good results, albeit with existing statistical measurement errors due to limited simulation times, which increase for a decreasing number of shared input channels. The cause and magnitude of these errors can be estimated theoretically, as shown in section 4.2.1.

Quantifying correlated neural spiking dynamics

In chapter 5, the correlation will be approached in the context of spiking neuron pairs, therefore differing from the one in the past chapter, which investigated only subthreshold dynamics.

In this context, two states were assigned to a neuron. A spiking state (ON-state), and a non-spiking state (OFF-state). This implies four possible states for any pair of neurons.

The theoretical prediction of such states can be achieved by utilizing the previously derived statistical values (chapter 3) through joint probabilites, as already utilized in chapter 4.

Based on these predictions, a possible method to quantify correlations resulting from shared channels input is the so-called Symmetric Uncertainty (SU), which was derived in section 5.1.
It was found that, the theoretically derived probabilities show a very similar dependency of input parameters as the results from the simulations.

In section 5.3, both the theoretical Symmetric Uncertainty and the one based on ON-states from action potentials, were compared for different configurations of shared input channels.

The quality of prediction depends heavily on the input rates. Low input rates prohibit the use of a bivariate Gaussian as an approximation, while for high synaptic input rates, notable statistical, as well as systematical errors exist. Their causes are discussed in section 5.4, leading to the conclusion that the quality of the prediction of the Symmetric Uncertainty is limited by the high susceptibility of statistical errors and, more importantly, the requirement of fixed ON-state lengths.

6.1 Outlook

In its present state, this work already has several direct applications. Together with the overlap minimization algorithm mentioned in the introduction, it offers the necessary tools to optimize the input-to-network mapping in the FACETS/BrainScaleS hardware, for the single chip as well as for the waferscale system. Furthermore, the closed-form expressions for the PSP shapes and the membrane potential distributions are already being used for the calibration of synapse drivers on the Spikey chip and can be used analogously for the HICANN module.

As an extension to the present work, it would be interesting to consider applying the same framework to sets of more than just two neurons in order to quantify and predict higher-order correlations. Naturally, the correlation coefficient will not suffice in this situation, raising the requirement for a more sophisticated correlation measure.

On a final note, this framework might also be useful in neuroanatomical studies, where simultaneous measurements of multiple neurons are notoriously difficult to perform. It is conceivable that by analyzing statistics of neuron pairs - not necessarily recorded at the same time - one can use a reversed version of the developed theory to infer the number of common sources of a neuron pair from their correlated behavior. It might thereby be possible to formulate hypotheses about the connectivity of deeper brain structures without invasive measurement.

Appendix

Bibliography

Brette, R., and W. Gerstner, Adaptive exponential integrate-and-fire model as an effective description of neuronal activity, *J. Neurophysiol.*, *94*, 3637 – 3642, doi:NA, 2005.

Bruederle, Neuroscientific Modeling with a Mixed-Signal VLSI Hardware System, Ph.D. thesis, Kirchhoff-Institut für Physik, 2009.

Brüderle, D., et al., A comprehensive workflow for general-purpose neural modeling with highly configurable neuromorphic hardware systems, *Biological Cybernetics*, *104*, 263–296, 10.1007/s00422-011-0435-9, 2011.

Dayan, P., and L. F. Abbott, *Theoretical Neuroscience: Computational and Mathematical Modeling of Neural Systems*, The MIT press, Cambride, Massachusetts, 2001.

Destexhe, A., M. Rudolph, and D. Pare, The high-conductance state of neocortical neurons in vivo, *Nature Reviews Neuroscience*, *4*, 739–751, 2003.

Djurfeld, Lundqvist, Johansson, Rehn, Ekeberg, and Lansner, Brain-scale simulation of the neocortex on the IBM Blue Gene/L supercomputer, *IBM Journal of Research and Development*, *52*, 2008.

Emri, Antal, Toth, Cope, and Crunelli, Backpropagation of the Delta oscillation and the retinal excitatory postsynaptic potential in a multi-compartment model of thalamocortical neurons, *Neuroscience*, *98*(1), 111–127.

Esseen, C.-G., On the Liapunoff limit of error in the theory of probability, *Arkiv för matematik, astronomi och fysik*, (28), 1942.

Gerstner, W., and W. Kistler, *Spiking Neuron Models: Single Neurons, Populations, Plasticity*, Cambridge University Press, 2002.

Hartman, P., *Ordinary Differential Equations*, 2nd ed., Society for Industrial & Applied Math, 2002.

Hodgkin, The ionic basis of electrical activity in nerve and muscle, *Biological Reviews*, *26*, 339–409, 1951.

Hodgkin, A. L., and A. F. Huxley, A quantitative description of membrane current and its application to conduction and excitation in nerve., *J Physiol*, *117*(4), 500–544, 1952.

Klinke, *Physiologie*, 5th ed., Silbernagl, 2005.

Kraskov, Stogbauer, Andrzejak, and Grassberger, Hierarchical Clustering Based on Mutual Information, 2003.

Kremkow, J., L. U. Perrinet, G. S. Masson, and A. Aertsen, Functional consequences of correlated excitatory and inhibitory conductances in cortical networks., *Journal of computational neuroscience*, *28*(3), 579–594, doi:10.1007/s10827-010-0240-9, 2010.

Lundqvist, M., M. Rehn, M. Djurfeldt, and A. Lansner, Attractor dynamics in a modular network model, *Network: Computation in Neural Systems*, *17*(3), 253–276, 2006.

Markram, H., A. Gupta, A. Uziel, Y. Wang, and M. Tsodyks, Information processing with frequency-dependent synaptic connections., *Neurobiol Learn Mem*, *70*(1-2), 101–112, 1998.

Papoulis, A., *Probability, Random Variables and Stochastic Processes*, 4 ed., McGraw-Hill Europe, 2002.

Rieke, F., D. Warland, R. de Ruyter van Steveninck, and W. Bialek, *Spikes - Exploring the neural code.*, MIT Press, Cambridge, MA., 1997.

Rudolph, M., and A. Destexhe, Analytical integrate-and-fire neuron models with conductance-based dynamics for event-driven simulation strategies, *Neural Comput.*, *18*(9), 2146–2210, 2006.

Schemmel, J., D. Brüderle, K. Meier, and B. Ostendorf, Modeling synaptic plasticity within networks of highly accelerated I&F neurons, in *Proceedings of the 2007 IEEE International Symposium on Circuits and Systems (ISCAS'07)*, IEEE Press, 2007.

Schemmel, J., D. Brüderle, A. Grübl, M. Hock, K. Meier, and S. Millner, A wafer-scale neuromorphic hardware system for large-scale neural modeling, *Proceedings of the 2010 IEEE International Symposium on Circuits and Systems (ISCAS"10)*, pp. 1947–1950, 2010.

Shelley, M., D. McLaughlin, R. Shapley, and J. Wielaard, States of high conductance in a large-scale model of the visual cortex, *J. Comp. Neurosci.*, *13*, 93–109, 2002.

Song, S., and L. F. Abbott, Cortical development and remapping through spike timing-dependent plasticity, *Neuron*, *32*(2), 339–350, 2001.

Thompson, R. F., *The Brain*, W. H. Freeman and Company, New York and Oxford, 1985.

Vogginger, B., Testing the operation workflow of a neuromorphic hardware system with a functionally accurate model, Diploma thesis, University of Heidelberg, 2010.

Witten, and Frank, *Data Mining: Practical Machine Learning Tools and Techniques*, vol. 3, Morgan Kaufmann, 2005.

Statement of Originality (Erklärung):

I certify that this thesis, and the research to which it refers, are the product of my own work. Any ideas or quotations from the work of other people, published or otherwise, are fully acknowledged in accordance with the standard referencing practices of the discipline.

Ich versichere, daß ich diese Arbeit selbständig verfaßt und keine anderen als die angegebenen Quellen und Hilfsmittel benutzt habe.

Heidelberg, January 10, 2012

.....
(signature)